SEMICRYSTALLINE POLYMERS IN MATERIAL EXTRUSION ADDITIVE MANUFACTURING

A Dissertation
Presented to
The Academic Faculty

by

Emily R. Fitzharris

In Partial Fulfillment
of the Requirements for the Degree
Doctor of Philosophy in the
School of Materials Science and Engineering

Georgia Institute of Technology
May, 2019

SEMICRYSTALLINE POLYMERS IN MATERIAL EXTRUSION ADDITIVE MANUFACTURING

Approved by:

Dr. Meisha L. Shofner, Advisor
School of Materials Science and Engineering
Georgia Institute of Technology

Dr. Donggang Yao
School of Materials Science and Engineering
Georgia Institute of Technology

Dr. David W. Rosen, Advisor
The George W. Woodruff School of Mechanical Engineering
Georgia Institute of Technology

Dr. H. Jerry Qi
The George W. Woodruff School of Mechanical Engineering
Georgia Institute of Technology

Dr. Seung Soon Jang
School of Materials Science and Engineering
Georgia Institute of Technology

Date Approved: November 30, 2018

To my family and Lauren:

For your unwavering support and encouragement

ACKNOWLEDGEMENTS

I would like to express my sincere thanks to my research advisors, Dr. Shofner and Dr. Rosen, for their support and guidance throughout my doctoral research. They have both played an integral role in my development as a researcher and I owe my growth and success to the time they invested in me. The way they taught me to think scientifically and critically will undoubtedly be a skill I use throughout my life as a member of the scientific community. I would also like to thank my committee members – Dr. Jang, Dr. Yao, and Dr. Qi for the guidance and insight that gave me direction and shaped the course of this research.

I would also like to thank the Kimberly-Clark Corporation for funding my graduate research. Working with Geof Carlow and Peter Allen throughout my time as a graduate student was a unique opportunity that taught me how to communicate technically with a wide range of audiences. Those opportunities taught me so much and gave me a well-rounded research experience.

I would like to thank my research group members, Dr. Prateek Verma, Matthew Orr, Narumi Watanabe, and Cam Irvin. Your help, support, input and friendship was a crucial part of my experience as a graduate student. I would especially like to thank Ian Watt, my undergraduate student, for all of his hard work and dedication to his research. The work he helped me with was invaluable and I appreciate all of the long hours he put in to complete every task I threw his way.

I would also like to thank HYREL International for their help and support with the material extrusion additive manufacturing system in this work. Their prompt reply to emails and phone calls made the novel applications of material extrusion in this work possible. I would also like to thank Dr. Yao for the use of his capillary rheometer.

Finally, I would like to thank my family and friends. I am extremely grateful to my parents for their unwavering assurance and support. Lastly, I would like to thank Lauren D'Amico for always believing in me, listening to so many presentation runs, and offering endless support and encouragement.

TABLE OF CONTENTS

LIST OF TABLES

LIST OF FIGURES

LIST OF SYMBOLS

$\boldsymbol{\alpha(T)}$	Coefficient of thermal expansion
$\boldsymbol{a}$	Acceleration
β	Cooling rate
$\boldsymbol{C}$	Elasticity stiffness matrix
C_{ijk}	Component *ijk* of the elasticity stiffness matrix
δ_{ij}	Kronecker-delta
$\dot{\gamma}$	Shear rate
G	Shear modulus
ΔH_m	Enthalpy of melting
ΔH_m^o	Theoretical enthalpy of melting of a 100% crystalline material
Δc_p	Specific heat capacity
$\Delta c_{p,a}$	Specific heat capacity of the glass transition of a completely amorphous polymer
ΔT	Temperature gradient
$\delta \mathbf{x}$	Nodal displacement
$\boldsymbol{D}$	Rate-of-deformation tensor
$\boldsymbol{D}$	Directors that define direction of nodal displacement
$\frac{DT}{Dt}$	Material derivative of temperature
$\boldsymbol{\varepsilon}$	Total strain
$\boldsymbol{\varepsilon_M}$	Mechanical strain
$\boldsymbol{\varepsilon_{tm}}$	Thermal strain
E	Young's modulus
E_s	Young's modulus of polymer matrix in a composite

F	F-ratio
$\boldsymbol{f}$	Volume force
f_n	Normal force per unit length
f_τ	Tangential force
h	Convection coefficient
h	Geometrical degree of freedom for amplitude of normal displacement
$H(T)$	Arrhenius function
η	Viscosity
K	Power-law constant
k	Thermal conductivity
λ	Lamé constant
ν	Poisson's ratio
μ	Lamé constant
n	Power-law constant
n	Number of experiments used in the Taguchi method
n	Number of heating and cooling cycles performed with FSC
$\boldsymbol{n}$	Unit normal vector
φ	Filler volume fraction in a polymer composite
p	Pressure
P_e	Percent contribution of the experimental error to the design output
P_i	Percent contribution of the i^{th} control parameter to the design output
$Parameter_i$	Material property value of material i
Q	Volumetric flow rate
$\boldsymbol{q}$	Heat flux
ρ	Density

R	Gaussian curvature
R_i	Principle radius of curvature measured in i^{th} orthogonal directions
r	Heat generated per unit volume by external forces
$\boldsymbol{\sigma}$	Cauchy stress tensor
σ	Surface tension coefficient used in free surface calculation
$\boldsymbol{\sigma : D}$	Viscous dissipation
σ_{VM}	Von Misses stress
SS_e	Sum of squares for the experimental error
SS_i	Sum of squares of the i^{th} control parameter
SS_T	Total sum of squares
τ	Unit vector tangent to free surface
$\boldsymbol{T}$	Extra-stress tensor
T_0	Reference temperature
T_a	Annealing temperature
$T_{ambient}$	Environment temperature
T_{BP}	Build platform temperature
$T_{c,\,cold}$	Cold crystallization peak temperature
T_g	Glass transition temperature
T_{sint}	Critical sintering temperature
v	Velocity
v_n	Normal velocity
v_s	Tangential velocity
Var_e	Variance of experimental error
Var_i	Variance of the i^{th} control parameter
$Warpage_i$	Warpage value obtained from process simulation model

$\boldsymbol{x}$	Node position
ψ_i^h	Shape function associated with geometrical degree of freedom
$\hat{y}$	Response target value in the Taguchi method
y_i	Response for the i^{th} experiment in the Taguchi method

LIST OF ABBREVIATIONS

ABS	Acrylonitrile-*co*-butadiene-*co*-styrene
AFM	Atomic force microscopy
AIN	Aluminum nitride
AM	Additive manufacturing
ANOVA	Analysis of variance
ASA	Acrylonitrile styrene acrylate
BC	Boundary conditions
CAD	Computer aided design
CTE	Coefficient of thermal expansion
DOE	Design of experiments
DOF	Degrees of freedom
DSC	Differential scanning calorimetry
DW	Direct writing
FDM	Fused deposition modeling
FEM	Finite element method
FFE	Full factorial experiment
FSC	Fast scanning calorimetry
HIPS	High impact polystyrene
MEMS	Micro-electro-mechanical systems
MEX	Material extrusion additive manufacturing
NAMII	National manufacturing innovation institute
PA	Polyamide

PB	Polybutene
PBN	Polybutylene naphthalate
PBT	Polybutylene terephthalate
PC	Polycarbonate
PCL	Poly(ε-caprolactone)
PEEK	Polyether ether ketone
PEKK	Polyether ketone ketone
PEI	Polyether imide
PE	Polyethylene
PET	Polyethylene terephthalate
PETG	Polyethylene terephthalate glycol copolymer
PLA	Polylactic acid
PMMA	Polymethyl methacrylate
POM	Polyoxymethylene
PP	Polypropylene
PPO	Polyphenylene oxide
PPS	Polyphenylene sulfide
PPSF	Polyphenylene sulfone
PPSU	Polyphenylene sulfone
PS	Polystyrene
PSU	Polysulphone
PTFE	Polytetrafluoroethylene
PVA	Polyvinyl alcohol
PVDF	Polyvinylidene fluoride
RAF	Rigid amorphous fraction

S/N	Signal-to-noise
SAXS	Small angle X-ray scattering
SLA	Stereolithography apparatus
SLS	Selective laser sintering
SS	Sum of squares
TEM	Transmission electron microscope
TPC	Thermoplastic copolyester elastomer
TPU	Thermoplastic polyurethane
UDF	User defined function
WAXS	Wide angle X-ray scattering

SUMMARY

Material extrusion (MEX) additive manufacturing is one of the most widely used additive manufacturing techniques in which a polymer filament is liquefied and extruded through a nozzle to fabricate a three-dimensional part in a layer-by-layer deposition technique. While MEX offers many advantages over traditional manufacturing methods, the shift of MEX from a prototyping method to a manufacturing technique is limited by the inferior mechanical properties of the produced parts compared to bulk parts and the limited number of MEX feedstock materials. The objective of this research was to provide insights into the molecular behavior specific to semicrystalline MEX materials that influence the resulting MEX part behavior. Polyphenylene sulfide (PPS) was used as a case study material in this research. Process simulation models were developed that predicted the temperature evolution of MEX parts during fabrication and determined correlations between material properties and deformation characteristics of MEX parts. Fast scanning calorimetry showed that the cooling rates experienced during MEX hindered the crystallization of PPS. In addition, a process optimization of material dependent thermal history parameters reduced the disparities between bulk and MEX parts. The combination of process simulation models, thermal and mechanical characterization, and process optimization techniques studied in this research developed a methodology for successfully printing high quality MEX parts using semicrystalline materials.

CHAPTER 1. INTRODUCTION

Material extrusion additive manufacturing (MEX) is an additive manufacturing (AM) process that deposits liquefied thermoplastic polymer filament layer-by-layer to fabricate three-dimensional parts. The unique capabilities of MEX compared to traditional manufacturing methods have motivated increased research in shifting MEX from a prototyping technology to a manufacturing method. However, there are challenges to using MEX parts in end use applications. Parts fabricated with MEX have reduced and anisotropic mechanical properties due to the numerous interfaces inherent to the additive build technique. In addition, MEX has been limited to a few feedstock materials, which are primarily amorphous polymers. Continued growth of the MEX market is dependent on continued improvement in the performance of parts produced with MEX and the development of new feedstock materials, specifically semicrystalline polymers. The objective of this research was to provide insights into the molecular behavior specific to semicrystalline MEX materials that influence the resulting MEX part behavior. Polyphenylene sulfide (PPS) was used as a case study material in this research.

The use of semicrystalline polymers with MEX presents challenges due to the shrinkage that occurs in semicrystalline materials as polymer chains draw together and order during cooling and crystallization. In MEX, this shrinkage can result in difficulty during fabrication and parts with low quality when MEX parts warp during fabrication and become detached from the build platform. Process simulation models of MEX were developed in ANSYS® Polyflow and ANSYS® Mechanical to predict the temperature evolution of MEX parts and to determine the correlations between material properties and

warpage and deformation characteristics. The correlations between material properties and MEX part characteristics established using the process simulation models could facilitate new material development strategies in order to expand the materials available for MEX.

The crystallization behavior in semicrystalline polymers is heavily dependent on the thermal history of the material. The effects of the temperature evolution and cooling rates simulated in the process simulation models on the crystallization behavior of PPS were investigated using differential scanning calorimetry (DSC) and fast scanning calorimetry (FSC). FSC showed that the cooling rates experienced during the MEX process hindered the crystallization behavior in PPS. The fast heating and cooling rates available to FSC were also used to mimic the rates experienced during MEX fabrication and the evolution of crystallinity during part fabrication was investigated. FSC could be used to determine the cooling rates that prevent crystallization in other semicrystalline polymers. These critical cooling rates could then be compared to simulated MEX cooling rates from the developed process simulation models. The combination of process simulation models and thermal characterization techniques could provide a screening method for predicting the deformation characteristics of new semicrystalline MEX materials. There are also various MEX process parameters that affect the thermal exposure of MEX parts during fabrication. By understanding how the thermal exposure affects crystallization and therefore the deformation characteristics of MEX parts, the process parameters can be selected to limit the crystallization that occurs during MEX part fabrication.

While limiting the crystallization that occurs during fabrication can help prevent warpage in MEX parts, low levels of crystallinity in semicrystalline polymers are typically associated with lower mechanical properties. A process optimization study was performed

using the Taguchi method to optimize thermal exposure variables in the MEX process to improve the mechanical properties of fabricated MEX parts. Post-processing heat-treatments were investigated in order to increase the crystallinity of fabricated parts and to increase the bonding between the interfaces inherent to the additive build technique. The effect of print temperature on the thermally driven bonding process was also investigated. Results of the process optimization showed that the use of post-processing heat-treatments at temperatures above the glass transition temperature of PPS increased the interlayer bonding strength of PPS MEX parts. Post-processing heat-treatments increased the percent crystallinity of the fabricated parts and increased inter-road and inter-layer bonding by allowing additional time for polymer chains to diffuse across bonded interfaces. Higher print temperatures also resulted in increased bonding between roads and layers because additional thermal energy was available. Control of the thermal history of MEX parts reduced the disparities between bulk and MEX mechanical properties. The improvement of MEX part properties could allow fabricated parts to be used in more end use applications.

In summary, the implications of semicrystalline polymer behavior on the MEX fabrication process and the resulting part quality were examined in this dissertation. In CHAPTER 2, the history of AM and MEX technologies and the materials and machines used in those fields are described along with the motivation for this research. CHAPTER 3 introduces and describes the process simulation models developed for PPS to establish relationships between material properties and MEX part warpage characteristics. The process simulation models also predicted the temperature exposure of MEX part fabrication, and the effect of the simulated cooling rates on PPS crystallization is described

in CHAPTER 4 through the use of DSC and FSC. CHAPTER 5 describes the process optimization performed to improve the mechanical properties on MEX parts by controlling the thermal history of the MEX process. Finally, CHAPTER 6 offers a comprehensive summary and final conclusions of this research.[†]

[†] Parts of this dissertation have been taken/adapted from author's publications – [21] and [49]

CHAPTER 2. BACKGROUND

2.1 Additive manufacturing

Additive manufacturing (AM) is a class of manufacturing techniques in which 3D parts are constructed in an additive, layer-by-layer fashion. The first commercial use of AM was in 1987 with Stereolithography apparatus (SLA) developed by 3D systems in which thin layers of light-sensitive liquid polymer are solidified to form a three-dimensional part [1, 2]. Since that time, AM technology has developed extensively and includes several different processes such as filament based material extrusion (MEX), direct writing (DW), Polyjet, and selective laser sintering (SLS). Originally referred to as rapid prototyping due to its use for developing visual aids or presentation models, AM was renamed to reflect its evolution from a prototyping technology to a manufacturing method capable of producing functional end-use parts [1, 3]. In 2010, the overall AM products and services industry had reached $1.325 billion and is projected to grow to over $5 billion by 2020 [2]. Investments in AM research and development have increased rapidly from both industry and government agencies as shown by the establishment of the ASTM Committee F42 on Additive Manufacturing Technologies in 2010 and the National Additive Manufacturing Innovation Institute (NAMII) in 2012, now known as America Makes [4, 5].

The major ways AM processes differ are in the materials they use, how the layers are fabricated, and how the layers are subsequently bonded together [1]. However, all AM processes follow the same general process for additively fabricating three-dimensional parts. In AM, a model initially generated using a 3D Computer Aided Design (CAD)

system is directly fabricated. The generated CAD model of the desired part is first converted into an STL file and then "sliced" into thin horizontal layers in the XY plane using AM software. The AM software also generates a tool path for the AM machine that specifies how the individual layers will be fabricated. With the tool path, the AM machine can fabricate the 3D part in an additive fashion [1, 6, 7].

AM technologies have several unique capabilities when compared to conventional manufacturing processes. Because AM technologies fabricate objects layer-by-layer, they are able to fabricate virtually any geometry. This differs from traditional subtractive (cutting, milling, grinding, etc.) and formative (pressing, casting, forming, etc.) processes that are limited by design constraints inherent to their fabrication methods. The design flexibility of AM allows for the fabrication of parts that have been topologically optimized to reduce material cost and decrease the part mass. The design flexibility of AM also results in no additional cost besides the AM machine cost when fabricating complex geometries with AM. This is because there is no need for additional tooling, increased operator expertise, or fabrication time. However, when examining a traditional manufacturing method such as injection molding, there is a direct link between part complexity and cost due to the cost of the mold [8]. Injection molding and some other conventional manufacturing methods are very time and cost efficient for mass production, in spite of their high initial tooling costs. While AM is much slower than injection molding for fabricating parts, AM technologies are better suited for low part quantities [6].

AM technologies were originally used for prototyping because their unique advantages allowed for reduced time between design and production, improvement in redesign time, and reduced cost of redesign [1, 3, 6, 9]. The recent improvements to AM

technology processes combined with the reduction in costs of the technology have increased its use as a manufacturing method in three key industries: automotive manufacturers, aerospace companies, and medical industries [3, 6]. Automotive manufacturers have leveraged the ability of AM to bring new products to market quickly in order to reduce time and development costs in new vehicles. AM is also the preferred manufacturing method for the production of parts for low-volume, high-end automobiles because it is more cost-effective compared to traditional manufacturing methods more suited for high volume production [3, 9]. Aerospace companies are primarily interested in AM technologies because of their ability to fabricate complex and high performance geometries. The ability of AM to integrate mechanical functionality, eliminate assembly, and create internal functionality, such as cooling channels or internal honeycomb structures, are used to create lightweight structures with high geometrical and functional complexity [3, 9]. Medical industries utilize AM technologies to tailor devices to suit the needs of individual patients. This is facilitated by the ease in which 3D medical imaging data can be converted into files compatible with AM technologies [1, 3, 6].

While there are many unique capabilities of AM technologies, they still experience different barriers and challenges. When compared to injection molding, the cost of large batch fabrication of standardized parts is significantly higher for AM due to the slower cycle time associated with AM technologies. However, in the industries that currently use AM technologies for end use parts, the slow cycle time is outweighed by the benefits of reduced material waste, consolidated parts, or the demand for customized geometries [6]. In addition, there is a trade-off between layer resolution and build time of parts fabricated with AM. While increasing the layer resolution provides a better surface finish, the

increased number of layers causes the build time to increase. Because of this, there is a relationship between the layer resolution and the overall scale of the part to be fabricated with AM technologies [6]. In addition, while the cost of AM machines has decreased, the high cost of some AM systems still limits their use in industrial applications [1, 3, 6].

AM technologies also suffer from a limited material selection while traditional manufacturing methods have a wide variety of materials that are compatible with their fabrication methods. Due to the limited number of AM materials available, the applications of AM are hindered while traditional manufacturing methods are able to accommodate a variety of materials suited for many different applications. In addition, because of the layer-by-layer fabrication method used in AM, produced parts suffer from anisotropic properties due to interlayer bonding deficiencies. The tensile strength of acrylonitrile-*co*-butadiene-*co*-styrene (ABS) parts produced with MEX has been shown to be dependent on the testing direction. The tensile strength of MEX parts tested parallel to the layers was up to four times as large as the tensile strength of parts tested perpendicular to the layer direction [10]. Similarly, the layer-by-layer fabrication method also results in parts that are not as strong as injection-molded parts of the same material. MEX parts tested along the layer direction still resulted in tensile strengths that were between 65 and 72 percent of the tensile strength of injection molded ABS parts [10]. There is also a lack of understanding of the basic physics that occur during AM processes due to the complexity of multiple interacting physical phenomena [11].

2.2 Filament based material extrusion additive manufacturing

MEX is an AM process used to fabricate three-dimensional parts through the deposition of liquefied thermoplastic polymer filament. MEX is one of the most widely used AM technologies due to its increased availability because of its relatively low cost compared to other AM technologies [1, 6, 7, 9]. MEX follows the same general procedure outlined for AM in order to generate a three dimensional part [1]. In order to fabricate the layers, counter-rotating rollers grip and pull a polymer filament in order to convey it into a heated chamber. As the filament moves through the heated chamber, it gradually softens. The liquefied polymer filament is then pushed out of the nozzle tip and deposited in a road on the XY plane. The liquefied material bonds with adjacent roads before solidifying. Once all the roads in a given layer are deposited, the build platform indexes downward to prepare for the next layer to be deposited on top of the subsequent layer. This process is repeated until the entire part is fabricated. The deposition nozzle tip in MEX is typically around 0.4 mm in diameter and the typical layer height is around 0.2 mm [6].

MEX has many settings and variables present in the process known as process parameters. MEX process parameters can be grouped into two categories: deposition strategy and thermal management variables. Deposition strategy variables dictate how the part is additively realized and include settings such as deposition orientation, print speed, layer height, infill density, and many others. The orientation of roads and layers dictated by deposition strategy variables have been shown to affect the mechanical properties of the resulting parts [10, 12-14] Thermal management variables, such as print temperature, build platform temperature, and build chamber temperature, dictate the thermal conditions imposed upon the part. The bonding process between roads and layers in MEX is a

thermally driven process based on wetting between adjacent filaments and the diffusion at the interface shown in Figure 2.1 [15-19]. Only partial bonding occurs between roads and layers due to the rapid cooling of MEX roads. The selection of print temperature has been shown to be influential on the neck growth process between deposited roads while the build platform and environment temperature have been shown to increase time above glass transition temperature, leading to increased diffusion between roads and layers [17]. Due to the influence of MEX process parameters on layer and road orientation and on the thermally driven bonding process, the success of the MEX process and the resulting part quality depend on the proper selection of MEX process parameters [20].

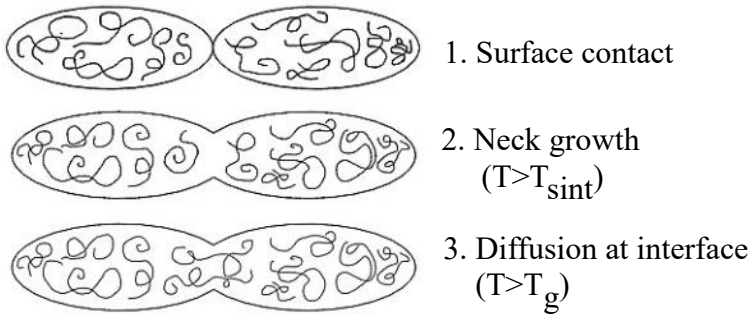

Figure 2.1: The bonding process in MEX begins with surface contact between the newly deposited road and adjacent interfaces (1). A neck is then formed between the interfaces through wetting, but only partial bonding occurs as the material quickly cools below its critical sintering temperature, T_{sint} (2). Diffusion then occurs across the interface until the material cools below its glass transition temperature (3). This diffusion process has been shown to be dependent on temperature and scale with time to the fourth power [21].

2.3 Materials used in filament based material extrusion

Amorphous polymers are typically used in MEX due to their gradual softening above glass transition temperature and relatively low shrinkage during cooling [7, 9, 22]. The most commonly used materials with MEX are ABS and polylactic acid (PLA). ABS is a rigid and amorphous engineering thermoplastic with many useful properties such as low cost, durability and toughness [12, 23, 24]. These properties make ABS particularly suited for producing prototypes or end-use parts in some applications. PLA is a popular material due to its biocompatibility and biodegradability. It is also an attractive material because it is derived from natural renewable sources [25, 26]. With the increase in popularity of MEX, the variety of commercially available MEX filament has increased dramatically. ABS filament can be purchased in a variety of colors and is also available in a translucent grade [27-30]. PLA filament is also available in several colors and has been used as the matrix material for different composite filaments. Composite PLA filaments have been developed with ceramic, clay, wood, and metal fillers in order to print objects with unique surface finish and aesthetic qualities while still maintaining the ease of printing of PLA [27-30].

The shift from MEX as a prototyping technology to a manufacturing technology has necessitated the broadening of material choices for the process [1, 6, 31]. In addition to the increase in available ABS and PLA filaments, there has also been an increase in different thermoplastics used for MEX filaments. The commercially available amorphous MEX filaments are summarized in Table 2.1 [27-30, 32-34]. There is a range of available MEX filaments including commodity, engineering and high-performance thermoplastics. In addition to ABS, other commodity thermoplastics that are commercially available as

MEX filaments include polyvinyl alcohol (PVA), polyethylene terephthalate glycol copolymer (PETG), acrylonitrile styrene acrylate (ASA), high impact polystyrene (HIPS), thermoplastic polyurethane (TPU), and thermoplastic copolyester elastomer (TPC) [27-30, 34]. PVA has been primarily used as an MEX support filament. Because PVA is water soluble, support structures printed using MEX can be easily dissolved away during post processing of the part [28, 29]. PETG is another commodity thermoplastic MEX filament that offers good coloring characteristics and has translucent grades that offer 89% light transmission. It offers the ease of printing of PLA with the strength and durability of ABS. It is also FDA approved for use in food containers and for tools used in food consumption [27-29]. ASA prints similarly to ABS, but is especially well suited for parts that would be outdoors due to its increased weatherability and UV resistance [27-30]. Another commodity thermoplastic, HIPS, offers increased flexibility and higher impact resistance compared to ABS, but still prints at similar temperatures [27-29]. TPU and TPC are also available as MEX filaments and offer increased flexibility [28, 29, 34]. These materials are used when fabricating objects that need to flex to fit their application such as stoppers, bumpers or belts. TPU and TPC require the use of specially designed extrusion print heads to prevent the filament from stretching or buckling as they pass through the pinch roller feeding system [28, 29, 34]. Commodity thermoplastic MEX filaments are typically used to fabricate non-functional porotypes, figurines, or other parts with non-structural applications [30].

MEX could be extended to part production instead of just producing prototypes by using precursor polymers with the structural, thermal, or functional properties desired in the final part. Engineering thermoplastics available as MEX filaments offer improved

material properties compared to commodity materials. Available engineering thermoplastic MEX filaments include a polyamide (PA) copolymer, polymethyl methacrylate (PMMA), and polycarbonate (PC) [28-30, 32]. While these materials offer improved properties, they are more difficult to process using MEX and require print heads with higher extrusion temperature capabilities. PA copolymer offers improved thermal, mechanical, fatigue, and chemical resistance characteristics compared to ABS. It is strong but still maintains some flexibility, making it more shatter resistant. However, PA absorbs moisture easily, and needs to be dried sufficiently before printing to ensure MEX part quality [28, 29, 32]. PMMA is also available as an MEX filament and is used for applications that require high stiffness, impact resistance and transparency [29]. Another engineering thermoplastic, PC, is available as an MEX filament and offers increased impact and heat resistance. It has also been blended with ABS and ASA to leverage the improved properties of PC but maintain the ease of printing associated with ABS and ASA [28-30, 32]. These engineering thermoplastics are used with MEX to produce strong parts that can withstand testing. By combining the improved material properties of engineering thermoplastics with the rapid tooling ability of MEX, these materials have been used for functional prototyping, conceptual modeling, manufacturing tools and even production parts [30].

Some high-performance thermoplastics are also available as MEX filaments and offer material properties suitable for the most rigorous thermal, structural, and chemical applications. Available amorphous high-performance MEX filaments include polysulphone (PSU), polyphenylene sulphone (PPSU or PPSF), and a polyether imide (PEI) known by its tradename, ULTEM. Polymers in the sulphone family, such as PSU

and PPSU, are known for their high heat-deflection temperatures, outstanding dimensional accuracy, and high chemical resistance [30, 33]. They have been used with MEX to produce parts with demanding applications such as low-volume injection molds, under-hood automotive scenarios, and heat, chemical, plasma and radiation sterilization [30]. Another material that is commonly used with MEX for engineering applications is ULTEM [30, 33, 35-37]. ULTEM is an amorphous, high performance thermoplastic with a high strength-to-weight ratio and excellent thermal and mechanical properties. Two grades of ULTEM are commercially available as MEX filaments: ULTEM 9085 and ULTEM 1010 [30, 33].While these materials offer exceptional properties and performance, they are much more difficult to process using MEX and require the use of very high printing temperatures.

Table 2.1: Commercially available amorphous MEX filaments [27-30, 32-34]

	Material	T_g [°C]	Print temperature [°C]	Key characteristics
Commodity	PVA	37	190-220	Water soluble, used for support structures
	PETG	80	230-260	Good coloring, 89% light transmission in transparent grades, FDA approved
	ASA	100	235-255	UV-resistant weatherable
	HIPS	104	235-245	Increased flexibility, higher impact resistance
	ABS	108	230-240	Versatile, durable, ductile
	TPU	120	210-240	Flexible
	TPC	Not given	230-255	Flexible, UV resistant
Engineering	PA copolymer	105	250-270	Improved thermal, mechanical, fatigue and chemical resistance compared to ABS
	PMMA	85-110	245-255	Transparent, high impact resistance and stiffness
	PC-ABS	125	270-290	Increased mechanical properties and higher heat resistance with printability of ABS
	PC-ASA	125	270-290	UV-stability with increased mechanical and thermal properties
	PC	161	280-310	High impact and high heat resistance
High performance	PSU	185	350-380	Excellent thermal and chemical resistance, hydrolytic resistance, resistant to gamma radiation, sterilization capable, flame resistant
	ULTEM 9085	186	350-380	Flame resistance, chemical resistance, excellent dimensional stability, hydrolytic stability, exceptional strength and modulus
	ULTEM 1010	217	370-390	Flame resistance, chemical resistance, excellent dimensional stability, hydrolytic stability, exceptional strength and modulus, stable dielectric constant
	PPSU/PPSF	220	360-390	Excellent thermal and chemical resistance, hydrolytic resistance, outstanding impact resistance, resistant to gamma radiation, sterilization capable, flame retardant

While amorphous polymers have traditionally been used with MEX, semicrystalline polymers could serve as possible new materials for use in MEX because of the advantages they offer over amorphous materials such as their deformability, toughness, and increased service temperatures [38, 39]. However, the extension of semicrystalline polymers to use in MEX is not straightforward due to the sharp viscosity changes exhibited after melting and the shrinkage that occurs as the MEX part cools and crystallizes. More dense crystalline regions are formed in semicrystalline materials as the polymer chains draw together and order during cooling, which results in increased shrinkage when compared to amorphous polymers. This shrinkage can result in difficulty during fabrication and parts with low quality when MEX parts warp during fabrication and become detached from the build platform.

The commercially available semicrystalline MEX filaments are given in Table 2.2 and include a range of materials including commodity, engineering and high performance thermoplastics. In addition to PLA, another commodity semicrystalline thermoplastic available as an MEX filament is polypropylene (PP) [28, 29]. While PLA is one of the most popular MEX materials due to its ease of printing, PP has been shown to be difficult to print with due to its large amount of warpage and poor layer adhesion [29, 40]. However, PP does offer advantages such as its chemical inertness and flexibility.

Semicrystalline engineering thermoplastics available as MEX filaments include polyoxymethylene (POM), and two PA, PA 12 and PA 6 [29, 30]. POM is commonly used in gears, bearings, and zippers due to its low coefficient of friction combined with its high dimensional accuracy. Both of these properties make POM well suited for use with MEX [29]. While the majority of available MEX PA filaments are amorphous, Stratasys

produces semicrystalline PA 12 and PA 6 filaments [30]. These materials offer high impact and fatigue resistance and offer one of the best combinations of strength and toughness of the available Stratasys MEX materials [30].

Currently, very few suppliers offer semicrystalline high performance thermoplastics as MEX filaments. The available semicrystalline high performance thermoplastics include polyvinylidene fluoride (PVDF), polyether ketone ketone (PEKK), polyether ether ketone (PEEK), and polyphenylene sulfide (PPS) [33]. PVDF offers exceptional thermal and chemical resistance properties making it well suited for industrial grade printing. PEKK and PEEK also offer exceptional thermal and mechanical properties but require extremely high processing temperatures. PEKK offers lower printing temperatures than PEEK while still exhibiting excellent properties including low smoke generation and service temperatures above 260 °C. While PEEK is more difficult to process, it is one of the highest performance thermoplastics available [33]. PPS is known for its excellent chemical and temperature resistance, as it has no known solvents at room temperature [41-44]. It is an attractive material for high performance applications due to its excellent mechanical properties and ease of processing [45]. While commercially developed PPS MEX filament is available from a few suppliers [46], various PPS composite pellets made with carbon fiber and aluminum nanofillers have been processed using MEX [47, 48].

Table 2.2: Commercially available semicrystalline MEX filaments [27-30, 32-34]

	Material	T_g [°C]	T_m [°C]	Print temperature [°C]	Key characteristics
Commodity	PLA	60-65	150-160	190-220	Biodegradable, does not require heated build platform, ease of printing
	PP	-15	160-175	235-265	Flexible, chemically inert, recyclable
Engineering	POM	-30	183	215-225	High stiffness, low friction, good dimensional stability
	PA 12	37-43	178	240-280	Tough, high impact and fatigue resistance
	PA 6	40-87	192	240-280	Tough, high impact and fatigue resistance
High performance	PVDF	-60 - -20	170-180	245-265	Uses up to 130 °C, good thermal and chemical resistance, good abrasion resistance, hydrolytic stability, resistant to nuclear radiation
	PPS	85	285	315-345	Insoluble in any known solvent under 200 °C, high thermal and mechanical properties, flame retardant and self extinguishing
	PEKK	162	335	345-375	Lower printing temperatures than PEEK with low smoke generation, outstanding mechanical, thermal and chemical resistance properties with service temperatures above 260 °C
	PEEK	150	350	400-420	Flame resistance, excellent mechanical, thermal and chemical resistance properties, service temperatures above 260 °C

2.4 Material extrusion additive manufacturing machines

Filament based MEX was developed and patented by Stratasys, Inc. under the name fused deposition modeling (FDM) in 1992. Since then, Stratasys, Inc. has continued to develop more advanced machines and their market share of commercial AM systems is 3.5 times larger than any other system manufacturer [2]. The Stratasys Fortus industrial manufacturing line of FDM machines cost from $100,000 to $500,000 and can achieve layer thicknesses as small as 0.078 mm with engineering thermoplastics such as ABS, ULTEM, PC, and PPSF [1, 7]. These systems are able to achieve very high resolution and fidelity, but operate with closed software and hardware that are only compatible with materials purchased from Stratasys.

When a key FDM patent expired, more companies began developing low cost MEX machines. Many of these systems were based on the open-source RepRap project [2, 7]. Since their introduction, these low cost personal systems have experienced very strong growth and retail businesses such as Staples, Shapeways, and Sculpteo are bringing commercial printing services directly to customers [6]. These personal systems are available from a variety of manufacturers for $1,500 - $5,000 and primarily print with only ABS, PLA, or other low temperature commodity thermoplastics [1, 7]. While the main driving force for these machines has been consumers and industries interested in low to medium fidelity prototyping in the early stages of product design, advances in MEX have the potential to significantly impact traditional production models in a variety of industries [6, 9]. Advancements in related technologies, such as improvements in available MEX materials and novel topology optimization techniques, have given rise to the development of another range of MEX machines. These machines have been designed with open

hardware and software to facilitate new MEX materials research, MEX process optimization studies, and MEX process simulation validation [1, 6, 7]. In addition, these advancements in MEX techniques can directly affect applied and basic research in other fields by providing unique capabilities unavailable to traditional manufacturing methods [6]. In this research, an MEX machine with open software and modular hardware capable of printing with a wide range of materials was used to provide insights into printing with semicrystalline polymers.

2.5 Motivation and research hypotheses

The unique capabilities of MEX compared to traditional manufacturing methods have motivated increased research in shifting MEX from a prototyping technology to a manufacturing method. This shift has necessitated printing with a wider range of materials, specifically semicrystalline polymers. Continued growth of the MEX market is dependent on continued improvement in the performance of parts produced with MEX and the development of new feedstock materials [7]. The objective of this research was to provide insights into the molecular behavior specific to semicrystalline MEX materials that influence resulting MEX part behavior. PPS was used as a case study material in this research.

A major factor hindering the growth of MEX is a limited understanding of the processing science in the thermally and mechanically complex process. Previous work with process simulation models has increased understanding of aspects of the MEX process, but these models have primarily focused on the MEX process with ABS and rely on

assumptions that simplify the complex material behavior inherent to the MEX process. In addition, few efforts have been made to simulate deformation of MEX parts due to thermal strains induced by thermal gradients developed in the part during fabrication. Process simulation models developed in this research were used to predict the temperature evolution of PPS MEX parts. This work was based on the hypothesis that process simulation models could establish correlations between material properties and warpage and deformation characteristics of PPS MEX parts. These process simulation models focused on modeling complex material property behavior exhibited by polymeric materials.

Based on the cooling rates modeled by the process simulation models, it was hypothesized that the thermal exposure during the MEX process could hinder the crystallization behavior of PPS. The crystallization behavior of PPS was examined using differential scanning calorimetry (DSC) and fast scanning calorimetry (FSC). While FSC has been utilized to examine the effects of cooling rates on crystallization in other polymer processing techniques, there have been no reports utilizing FSC to examine the MEX process. In addition, there have not been any reports of FSC to study the crystallization behavior of PPS.

Based on the crystallization behavior of PPS, it was hypothesized that control of the thermal history in the MEX process could reduce disparities between bulk and MEX parts. This was investigated through the use of design of experiments techniques to optimize the thermal exposures in MEX. The effect of MEX print temperature and post-processing heat-treatments on interlayer bonding in MEX parts were characterized through mechanical testing. While numerous process optimization studies have been performed

with design of experiments techniques on the MEX process, the majority of studies examine material independent process parameters and only use ABS as the feedstock material. The process optimization performed in this research focused on material dependent thermal exposure variables and developed a methodology for estimating print temperatures for new MEX materials based on the rheological behavior of ABS as a benchmark.

The combination of process simulation models, thermal and mechanical characterization techniques, and process optimization studies in this research developed a methodology for successfully printing high quality MEX parts using semicrystalline materials.

CHAPTER 3. EFFECTS OF MATERIAL PROPERTIES ON WARPAGE IN MEX PARTS[‡]

3.1 Background

MEX could be extended to additional production applications by using precursor polymers with the structural or functional properties desired in the part. Among these possible materials are semicrystalline polymers. Semicrystalline polymers offer advantages over amorphous polymers because they are deformable, tough and in general have higher service temperatures than amorphous polymers [39, 50]. Semicrystalline polymers present challenges in MEX processing due to the shrinkage that occurs during part cooling and crystallization. During crystallization, polymer chains are drawn together as they order to form more dense, crystalline regions. This ordering results in increased part shrinkage when compared to parts fabricated with amorphous thermoplastic polymers. Shrinkage also occurs to a lesser extent in amorphous materials, and one way that this behavior is characterized in polymers is with their coefficient of thermal expansion (CTE) value. Increased shrinkage is also an issue in molding operations with semicrystalline polymers, but mold cavity sizes can be designed to adequately account for the expected material shrinkage [51]. Specifically in MEX, the formation of the crystalline structure in polymers results in parts that warp and become detached from the build platform during

[‡] Parts of this chapter have been taken/adapted from author's publication - [49] E. R. Fitzharris, N. Watanabe, D. W. Rosen, and M. L. Shofner, "Effects of material properties on warpage in fused deposition modeling parts," *The International Journal of Advanced Manufacturing Technology,* vol. 95, no. 5, pp. 2059-2070, Mar 1 2018. https://doi.org/10.1007/s00170-017-1340-8

MEX part fabrication, resulting in difficulty in fabrication and reduced part quality. This part warpage is shown schematically in Figure 3.1.

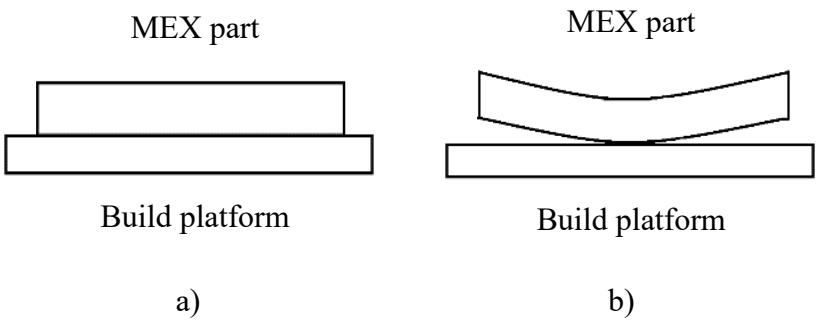

Figure 3.1: Representation of part warpage and shrinkage seen in MEX parts fabricated with (a) amorphous thermoplastic polymers and (b) semicrystalline thermoplastic polymers. Shrinkage that results from polymer chains drawing together and ordering during crystallization causes MEX parts to warp and separate from the build platform when printing semicrystalline polymers .

3.1.1 Fillers in MEX materials

Aside from the use of semicrystalline polymers, another method used to extend MEX to part production is to use fillers to increase material properties in polymer systems that are compatible with the MEX process. The tensile strength, modulus, and/or thermal conductivity of ABS have been increased through the addition of fillers such as carbon nanofiber, carbon fiber, glass fiber and metallic particles [52-56]. The material properties of other semicrystalline polymer systems, such as PP and poly(ε-caprolactone) (PCL), have been similarly modified using fillers such as thermotropic liquid crystalline polymers, bioactive glass, and glass fiber for use with MEX [57-61]. In addition, there are now a

variety of other commercially available MEX filaments with carbon fiber added, such as PLA, PETG, PA, PC, ULTEM, PEKK, and PEEK [62].

While the aforementioned studies focused primarily on enhancing the material properties of the MEX feedstock in order to increase the mechanical properties of the resulting MEX parts, others have used the addition of fillers to various polymer systems to improve the actual MEX process itself. Residual stresses and part warpage due to thermal gradients within MEX parts present challenges during the manufacturing of parts with MEX using both amorphous and semicrystalline materials. Previously, these challenges have been addressed by manufacturing MEX parts in a heated chamber to reduce the thermal gradients experienced by the parts. Love et al. showed that the addition of carbon fiber to ABS improved the strength and stiffness of final MEX parts. In addition, the carbon fiber increased the thermal conductivity and decreased the CTE of ABS. The changes in thermal conductivity and CTE led to reduced distortion or warpage in the MEX parts, especially in large-scale manufacturing of MEX parts [63].

This same concept was also applied to PPS [47]. This work used a lab-scale MEX machine developed specifically to process high temperature and high fiber content thermoplastic polymer pellets. This system differs from standard MEX machines that use thermoplastic filament as the precursor material. The addition of carbon fiber to PPS led to increased thermal conductivity and decreased CTE as seen in ABS. In addition, the carbon fiber reduced the die swell seen in PPS when extruded from the MEX nozzle, slowed down crystallization processes (both from the melt and upon heating, i.e. cold crystallization), and reduced the overall crystallinity of the composite. Because of these changes seen in the composite, large-scale PPS parts could be fabricated without significant part warpage using

MEX with an environment at room temperature. In another case, aluminum oxide and aluminum nanofillers were used to reduce the crystallinity, reduce the melt flow index, and increase the thermal properties of PA 6 to make it compatible with the MEX process [48].

3.1.2 MEX process simulation models

Continued growth of the MEX market relies on improvements in the performance and cost reduction of MEX systems and the development of new feedstock materials [7]. A major factor hindering this growth is a limited understanding of the processing science in the thermally and mechanically complex MEX process [11]. While well-developed processes such as injection molding have simulation systems such as MoldFlow® that can assist in process optimization and material development, there are limited commercial simulation options for AM. Autodesk has recently developed commercially available software known as Netfabb® that can predict the thermal and structural response of metal powder bed fusion parts [64]; however, there is no equivalent system for MEX.

Modeling of MEX processes pose interesting modeling challenges such as multi-dimensional transient heat transfer phenomena, phase changes, complex solution domains and rapidly changing and moving geometries. Process simulation models have been developed to understand the processing science in various aspects of the MEX process such as the pinch roller feed mechanism [65-70], liquefier dynamics [65, 67, 69, 71-75], road spreading [71, 76], bonding between adjacent roads [15-17, 77-79], and the thermal evolution of printed parts [15-17, 70, 71, 75, 77, 79-86].

The overwhelming majority of process simulation models only investigated ABS. Moreover, even though many process simulation models examined thermal gradients developed in MEX parts and discussed the influence of these gradients on warpage and deformation characteristics, few efforts have been reported that explicitly model thermal expansion, residual stresses, and/or warping due to thermal gradients [9]. There are also competing factors of modeling complex physics versus complex geometry given finite computational resources. Geometrical complexity has often been achieved in process simulation models through the use of element activation techniques that activate entire roads or discretized elements within a road to simulate deposition [75, 79, 82-87]. The use of element activation techniques assumes deposited MEX roads are cylindrical or rectangular and does not predict the actual geometry of deposited material. In addition, these models used solid elements and did not account for viscoelastic behavior of the polymeric MEX materials. The dependence of many polymeric material properties on temperature were also neglected and properties were constant across the wide temperature ranges simulated for MEX. Many studies also neglected heat transfer within deposited road cross sectional area and assumed only 1 dimensional heat transfer [79, 82, 87].

Process simulation models of MEX technologies developed by Bellini accounted for many of the limitations in other process simulation models [40, 71]. The models by Bellini examined the evolution of road shape, thermal gradients, and residual stresses present in MEX parts during fabrication [40, 71]. Bellini developed simulation models to study the thermo-fluid behavior of ABS in MEX in order to develop a tool that provided guidelines for the determination of process parameters and material properties during the process planning phase of MEX [71]. This tool contained five different sub-models that

described various steps present in the MEX process: melt flow in the liquefier, extrusion through the nozzle, free extrusion and swelling of the melt at the nozzle exit, evolution of the road in the first deposited layer, and evolution of the road in the successively deposited layers. A finite element approach using ANSYS® Polyflow was used to develop these sub-models through the evolution of a free surface. The viscosity of ABS was modeled as a function of both shear rate and temperature.

Previous work with collaborating authors investigated deformation characteristics in MEX of PP based on the process simulation models developed by Bellini [40]. The effects of material properties and process variable settings of MEX were examined using experiments and a multistep simulation model that simulated the deposition and cooling of two MEX filament roads. The results of that work indicated that some reductions in part warpage could be realized by changing process variables. Specifically, part warpage was reduced with increased deposition speed and increased layer height. Beyond process variables, material properties could be changed to reduce the warpage of PP parts, namely the introduction of fillers or the use of a less crystalline polymer such as propylene copolymers. Experimental results agreed qualitatively with the results obtained from the simulation model and showed that part warpage was influenced by material properties.

3.1.3 Key research objectives

In this chapter, neat PPS was investigated as a material for MEX using the same simulation model that the collaborating authors used to understand the printing behavior of PP. Due to the high melting temperature of PPS, the MEX processing temperature for PPS

is higher than the temperature for PP, 290 °C vs. 220 °C, respectively. This higher processing temperature results in faster convective cooling with the environment and could cause increased thermal gradients in the MEX part and, based on previous studies, suggests that PPS could exhibit increased warpage as compared to PP. However, produced PPS parts exhibited very little warpage when fabricated using MEX, especially compared to the warpage seen in unmodified PP. Therefore, the objective of this study was to identify what material properties of PPS caused it to exhibit minimal warpage when compared to PP through the use of process simulation models. Material parameters of PPS were parametrically changed to understand more fully which material properties have the largest effect on part warpage. This work was based on the hypothesis that process simulation models could establish correlations between material properties and warpage and deformation characteristics of PPS MEX parts.

3.2 Methods

3.2.1 Process simulation models

Two-dimensional MEX process simulation models were developed using ANSYS® Polyflow and ANSYS® Mechanical. The inputs to these simulation models were material properties, MEX process variable settings and MEX process conditions. The developed simulations predicted temperature distributions, deposited road shapes, residual stresses and warpage and deformation characteristics of MEX parts fabricated using PPS.

In the MEX process simulation models, 2 - 10 mm long roads of PPS were deposited at 290 °C onto a build platform held at a constant temperature of 85 °C. These temperatures were chosen since they matched the experimental values used to print PPS with MEX. The build platform was assumed to be glass and had a heat transfer coefficient of 100 W/m^2-°C to match the experimental MEX set up. The MEX process was broken down into 5 sequential simulation models: road 1 deposition, road 1 cooling, road 2 deposition, road 1 and 2 cooling, and residual stress and warpage analysis. These simulation models were linked together by importing the geometry and temperature profile from the previous model into the current model as the simulation progressed through the MEX process.

In the first simulation model, a road of PPS was deposited through an extrusion nozzle onto the build platform at a volumetric flow rate determined by Equation 3.1:

$$Q = vWH \tag{3.1}$$

where v was the deposition velocity, W was the width of the deposited rectangular road, and H was the road height. While the nozzle used in MEX had a round orifice, the deposited road adopted an approximately rectangular shape, so that shape was used in this calculation [66]. During the simulated deposition, the PPS filament was extruded through the nozzle in the vertical direction by applying the volumetric flow rate at the nozzle entrance with a gravitational force to cause the extrudate to flow downward from the nozzle. The volumetric flow rate calculated with Equation 3.1 was 3x10^{-6} m^3/s using the print speed of

15 mm/s and the layer height of 0.2 mm. Because the model was two-dimensional, the unit width of 1 m was used in the flow rate calculation.

The nozzle was held in a stationary position as the build platform translated horizontally at the deposition speed of 15 mm/s. In ANSYS® Polyflow, the build platform was defined as a mold with constant and uniform temperature of 85 °C. The geometry, mesh, and boundary conditions before road 1 deposition are show in Figure 3.2. The model contained 1562 nodes and 1390 elements total. The nozzle walls were represented by the top, right, and left boundaries of the modeled nozzle while the bottom boundary represented the extrudate free surface. Road 1 deposition was a two-dimensional planar, time-dependent, non-isothermal problem. The flow and thermal boundary conditions for the model were labeled at every boundary and the cross sections of the entire nozzle, extrudate, and build platform were modeled since road 1 deposition was not an axisymmetric model. As the first road was deposited on the build platform, the mesh in the extrudate deformed significantly. In order to properly mesh the changing geometry seen in the first road deposition, the remeshing technique in ANSYS® Polyflow was applied to the extrudate at the nozzle entrance to continually refresh the mesh in the first road during its deposition.

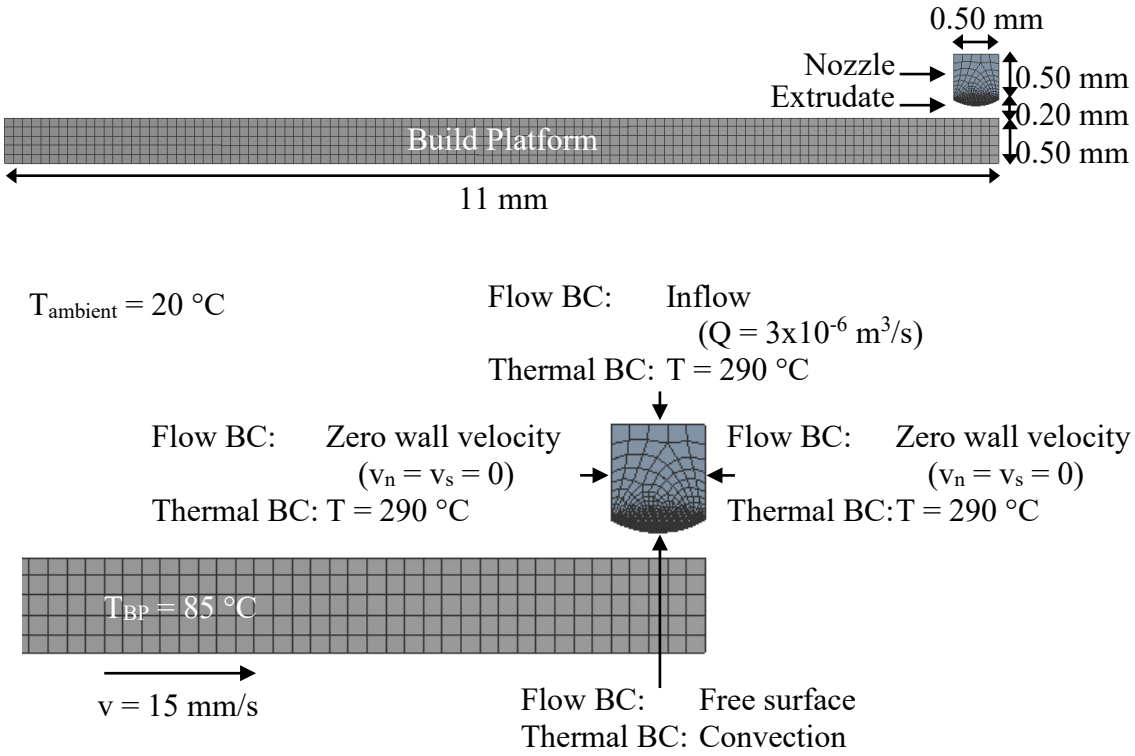

Figure 3.2: Geometry, mesh, and boundary conditions (BC) before road 1 deposition where v_n is the normal velocity and v_s is the tangential velocity.

The geometry and temperature profile of the first road were exported and used in the first road cooling model. The mesh, geometry, and boundary conditions used in this step are shown in Figure 3.3. The model contained 22,613 nodes and 21,407 elements total. Compared to the first model, the nozzle was removed and the completed road 1 replaced the extrudate. It was also a two-dimensional planar, time-dependent, non-isothermal problem, so the flow and thermal boundary conditions for the model were labeled at every boundary. In this model, the build platform temperature was applied to the bottom surface of the first road while the outer surfaces were subjected to convective cooling with air at an ambient temperature of 20 °C. The cooling simulation was run over a time equal to the deposition time plus one second. The deposition time corresponded to the horizontal movement of the build platform back to its original position, and the one second corresponded to the time required for the vertical movement of the build platform downward to prepare for the second road deposition.

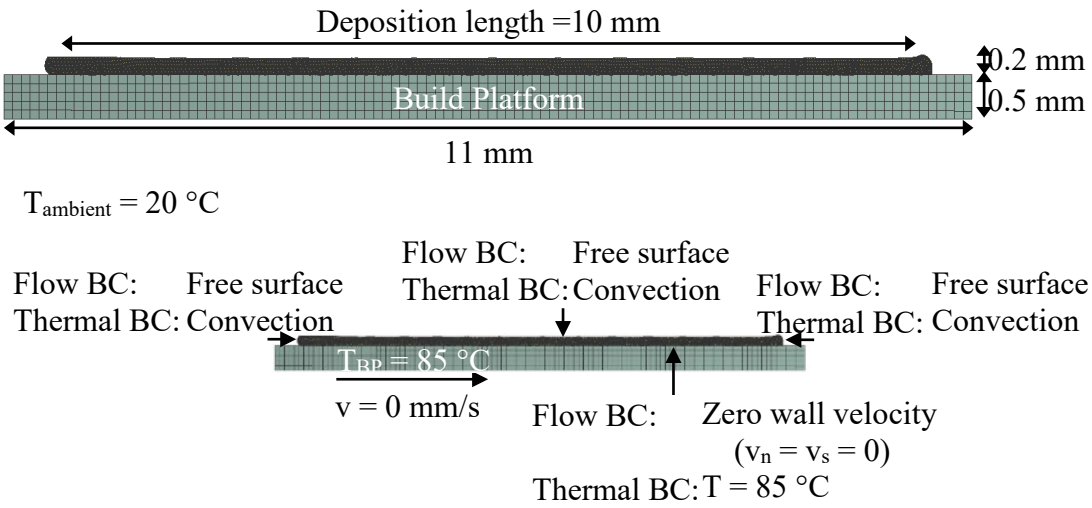

Figure 3.3: Geometry, mesh, and boundary conditions before layer 1 cooling where v_n is the normal velocity and v_s is the tangential velocity.

Road 2 deposition and cooling proceeded in a manner very similar to the first road deposition and cooling. The second road was deposited on top of the first road that was characterized by the exported geometry and temperature profile from the previous simulation model. The mesh, geometry, and boundary conditions used in this step are shown in Figure 3.4. The model contained 22,613 nodes and 21,407 elements total. During the second road deposition, conductive heat transfer occurred between the two roads by utilizing the fluid-to-fluid contact capability in ANSYS® Polyflow.

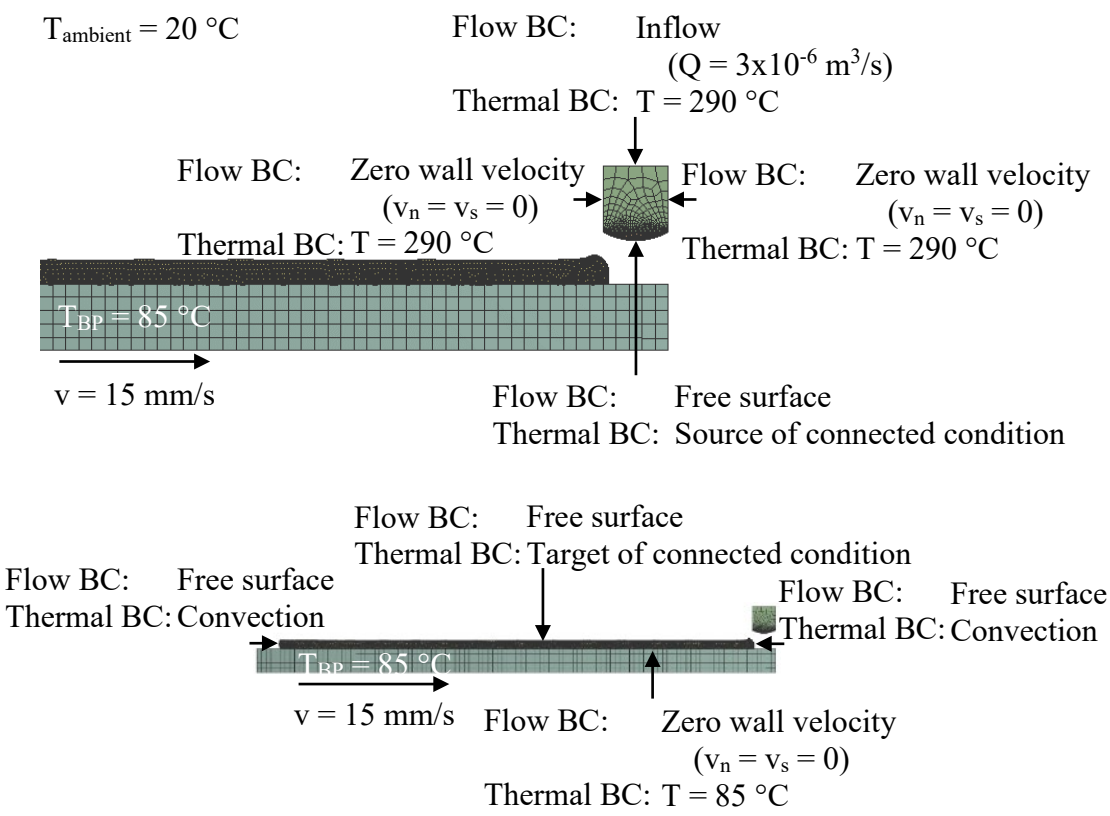

Figure 3.4: Geometry, mesh, and boundary conditions before road 2 deposition where v_n is the normal velocity and v_s is the tangential velocity. Conductive heat transfer occurred between road 1 and the second road as it was deposited by using the fluid-to-fluid contact capability in ANSYS® Polyflow.

Following road 2 deposition, road 1 and 2 cooling was performed using the exported geometry and temperature profile from road 2 deposition. In road 1 and 2 cooling, the roads were allowed to cool for 10 seconds. The mesh, geometry, and boundary conditions used in this step are shown in Figure 3.5. The model contained 131,705 nodes and 42,456 elements total. Compared to the previous model, the nozzle was removed and the completed road 2 replaced the extrudate. While the previous simulation models were performed in ANSYS® Polyflow, road 1 and 2 cooling was performed in ANSYS® Mechanical. Only thermal boundary conditions are used with ANSYS® Mechanical, so only thermal boundary conditions were applied at every boundary. The same thermal boundary conditions used in road 1 cooling were used in this simulation model.

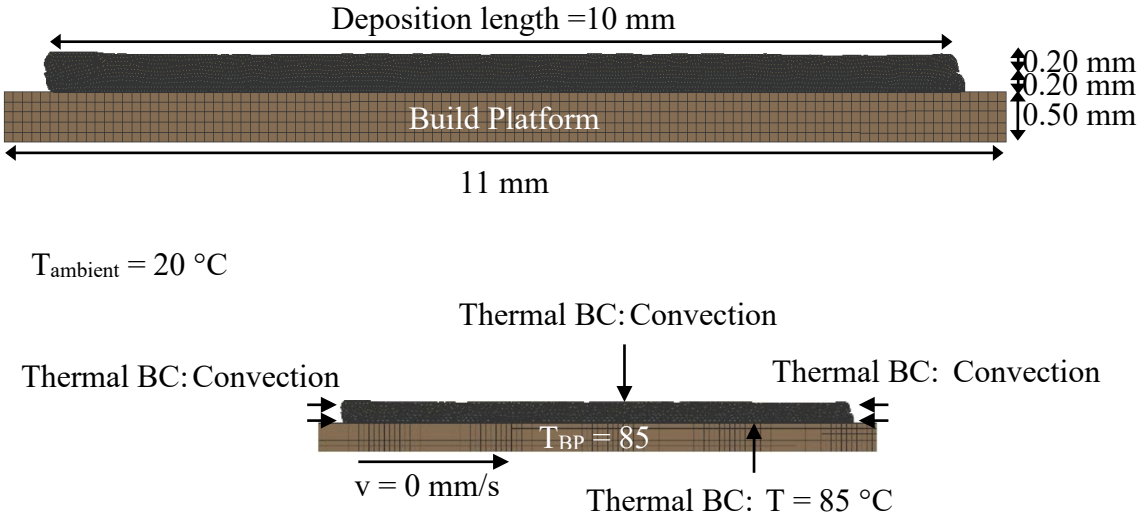

Figure 3.5: Geometry, mesh, and boundary conditions before road 1 and 2 cooling performed in ANSYS® Mechanical.

During this cooling period, the residual stress and warpage seen in the two roads were analyzed in the final simulation model. The temperature profiles and geometries of the two roads were exported from the road 1 and 2 cooling simulation model and imported into ANSYS® Mechanical to conduct structural analysis in the final process simulation model. The model contained 131,705 nodes and 42,456 elements total and the mesh, geometry, and boundary conditions used in this step are shown in Figure 3.6. The midpoint of the first road was fixed to the build platform and a zero force was applied everywhere else in order to compute the residual stress and warpage experienced in the two roads during cooling. The location of the fixed point between the first road and the build platform is shown in Figure 3.6.

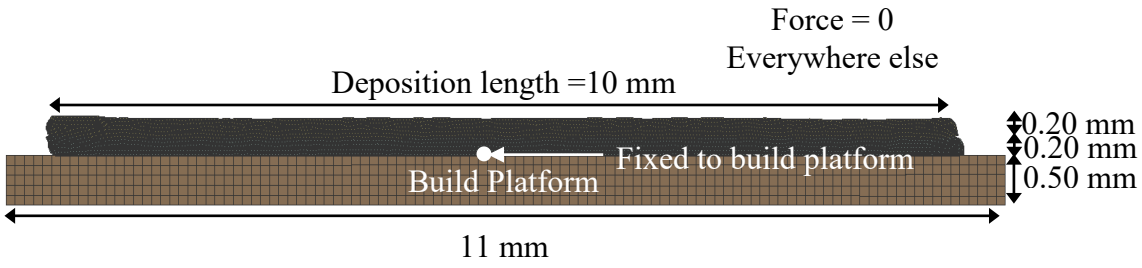

Figure 3.6: Geometry, mesh, and boundary conditions before the residual stress and warpage simulation performed in ANSYS® Mechanical.

The constitutive equations that govern the thermal and mechanical phenomena in the process simulation models are discussed in detail in APPENDIX A**.**

3.2.2 Material properties

The wide range of temperatures that occur during MEX made it necessary to consider many material parameters as a function of temperature [7]. To obtain inputs for the simulation model, the flow characteristics of PPS were characterized using both a theoretical treatment and experimental data from capillary rheology.

The dependence of PPS viscosity on both shear rate and temperature was accounted for in the MEX process by using the power-law viscosity model shown in Equation 3.2:

$$\eta = K(\dot{\gamma})^{n-1} \tag{3.2}$$

where η is viscosity, $\dot{\gamma}$ is shear rate, and K and n are power-law fit parameters. The temperature dependence of the viscosity was assumed to be described by an Arrhenius model shown in Equation 3.3:

$$H(T) = e^{\left[\alpha\left(\frac{1}{T}-\frac{1}{T_0}\right)\right]} \tag{3.3}$$

where α is the activation energy and T_0 is the reference temperature. The final viscosity equation for PPS combined the dependence of viscosity on shear rate and the dependence of viscosity on temperature [65]. This expression is given in Equation 3.4.

$$\eta = H(T)\eta_{T_0}(\dot{\gamma}) \tag{3.4}$$

Experiments were conducted on a capillary rheometer, the Dynisco LCR7001 [88], at various shear rates and temperatures to obtain a viscosity expression for PPS according to the equations given above. The L/D ratio of the capillary die was 40 with a length of 20 mm and a diameter of 0.5 mm. Shear rates representative of the MEX process, 100 to 10,000 s^{-1}, [7, 58] were used at temperatures 300 °C, 310°C, 320 °C, and 330 °C. PPS pellets used in the experimental runs were obtained from Technical Polymers with the product name Thermec S™. Two experimental runs were conducted at each temperature and a correction was made to convert apparent viscosity to true viscosity. No Bagley correction was performed due to limited capillary dies available for use. The viscosity as a function of shear rate obtained from experiments at each temperature is shown in Figure 3.7. The viscosity equation given in Equation 3.4 was fit to the experimental data and the resulting equation is given in Equation 3.5.

$$\eta = e^{\left[9345.5\left(\frac{1}{T}-\frac{1}{593.15}\right)\right]}914.61(\dot{\gamma})^{-0.25} \tag{3.5}$$

Using Equation 3.5, a viscosity surface plot was constructed to show the viscosity as a function of shear rate and temperature over a larger temperature range. This surface plot is shown in Figure 3.8.

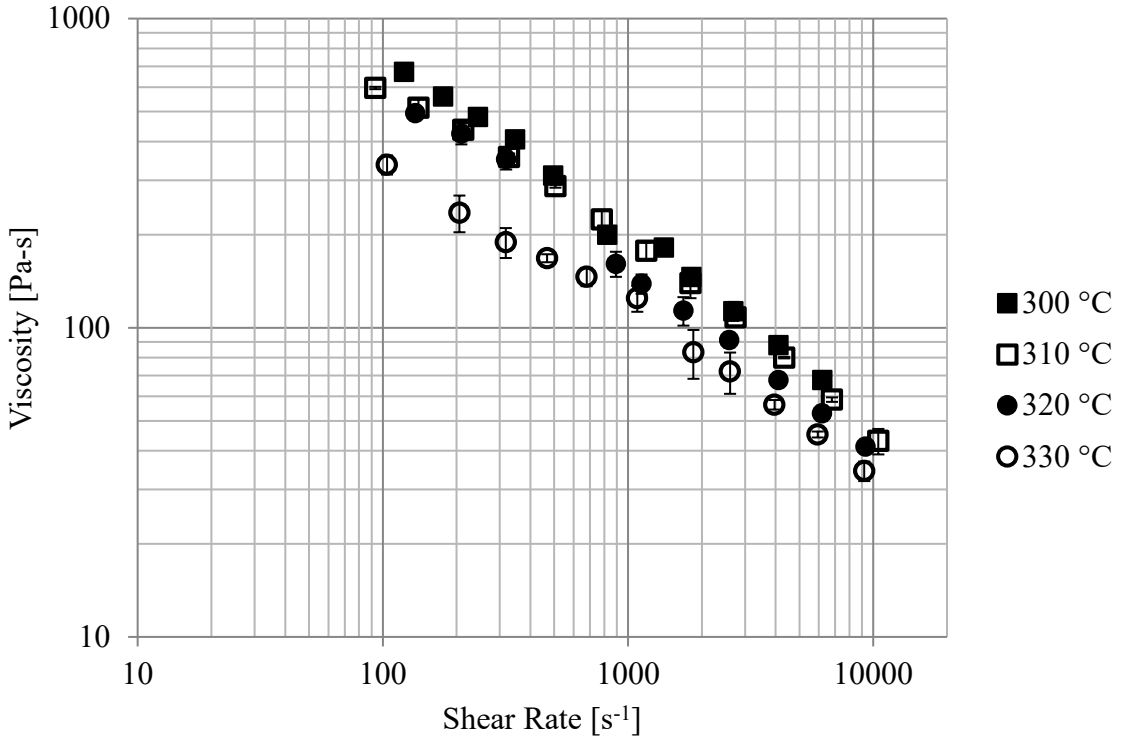

Figure 3.7: The viscosity of PPS as a function of shear rate. As expected, the viscosity decreased with increasing shear rate and increasing temperature.

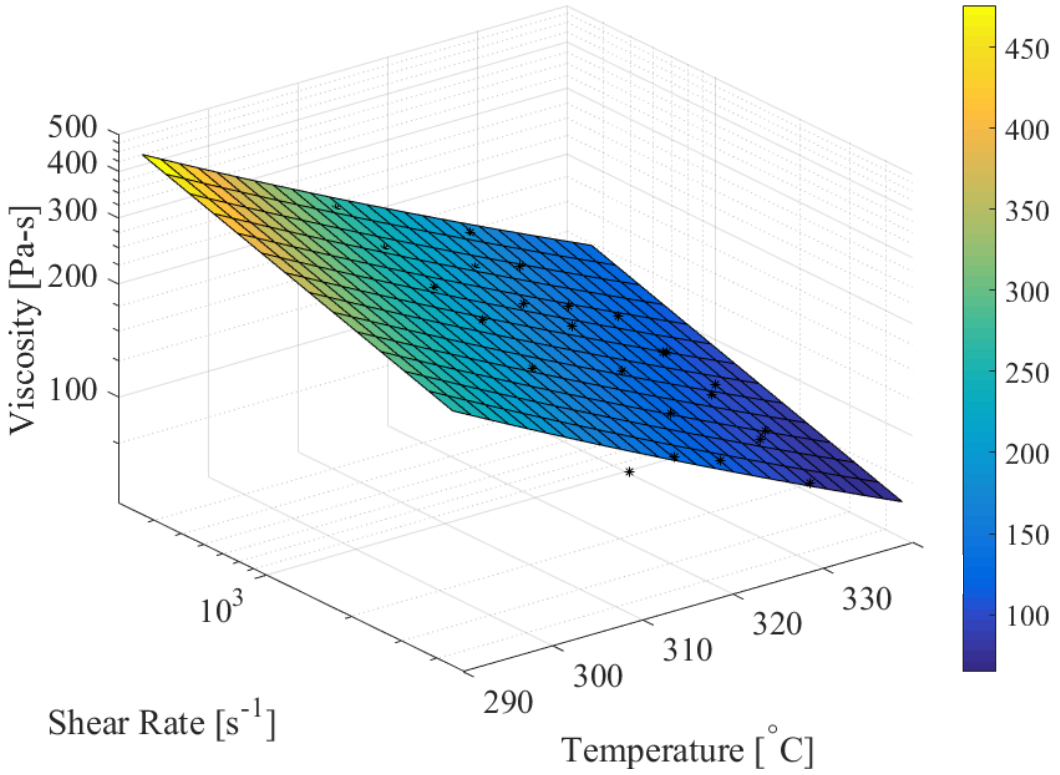

Figure 3.8: A viscosity surface plot for PPS was constructed by fitting Equation 3.4 to the experimental data. The symbols (*) represent experimental data while the surface plot was obtained using Equation 3.5, which was used to plot viscosity as a function of shear rate and temperature from 290 °C to 340 °C and from 100 s^{-1} to 10,000 s^{-1}.

Table 3.1 shows the material properties of PPS used as inputs for the simulation models compared to the same values for PP used in previous work [40]. Most of these values were obtained from general material data sheets as opposed to experiment and may not exactly represent the properties of the materials or temperatures used for validation studies. Therefore, the simulation results were used primarily as qualitative indicators of material behavior and to provide a basis for comparison between the two polymers.

Table 3.1: Material properties of PPS and PP used in the simulation models [40, 89, 90]

Material property	**PPS**	**PP**
Viscosity expression	$\eta = e^{\left[9345.5\left(\frac{1}{T}-\frac{1}{593.15}\right)\right]}914.61(\dot{\gamma})^{-0.25}$	$\eta = e^{\left[1318.9\left(\frac{1}{T}-\frac{1}{503.15}\right)\right]}3346.4(\dot{\gamma})^{-0.54}$
Density	1350 kg/m^3	900 kg/m^3
Coefficient of thermal expansion	5.04 x 10^{-5} m/(m-°C)	1.50 x 10^{-4} m/(m-°C)
Thermal conductivity	0.288 W/(m-°C)	0.200 W/(m-°C)
Heat capacity	1001 J/(kg-K)	1920 J/(kg-K)
Surface tension coefficient	38.0 mJ/m^2	30.5 mJ/m^2
Young's modulus	4.50 GPa	1.75 GPa
Poisson's ratio	0.38	0.38

3.2.3 Primary assumptions and considerations

In the developed process simulation models for the deposition and cooling of two PPS MEX roads, some assumptions and considerations were made regarding the physics of the MEX process and the behavior of PPS. The material properties of PPS given in Table 3.1, except for viscosity, were assumed to be constant values in the entire simulated temperature range. However, CTE was modeled as a function of temperature in a separate set of process simulation models described in section 3.3.3. While the viscosity of PPS was modeled as a function of shear rate and temperature using a power-law model and an Arrhenius model, other aspects of viscoelasticity were not considered. Additionally, the volume contraction during crystallization was not captured explicitly in the simulation. Instead, CTE was used to capture this behavior.

In the two-dimensional transient heat transfer behavior, radiative heat transfer was assumed to be negligible. In addition, during deposition, full contact was assumed between road 1 and the build platform during road 1 deposition and between road 1 and road 2 during road 2 deposition. Following the cooling of road 1 and road 2, the temperature result was used as a load for the following structural analysis. During the deformation calculation, the displacement constraint between the build platform and road 1 was removed in order to allow the part to deform about a fixed point in the center of the part. This was assumed in order to mimic the symmetric curling of parts observed during fabrication in MEX.

3.2.4 MEX additive manufacturing machine

The MEX AM machine used in this study was the HYREL System 30 from HYREL International [91]. The HYREL System 30 gives users a large amount of control over the MEX process through its open hardware and software. The hardware in the HYREL System 30 can accommodate temperatures up to 450 °C. The print head uses a spring-mounted roller to convey the MEX filament into the liquefier chamber. This spring-mounted roller can translate filaments with diameters of around 1.3 mm up to 1.85 mm into the chamber.

The system uses a controller software known as Repetrel, which was developed by HYREL International. Repetrel is a modified version of Repetier [92], a controller software commonly used with other MEX machines. Various process parameters can be modified in real time during part fabrication within Repetrel. Some of the process settings include extrusion temperature, build platform temperature, filament feed rate, and the z position of the extrusion nozzle. Repetrel instructs the print head where to deposit material roads based on toolpath information in a G-code file. The G-code file is written using a common slicing software known as Slic3r [93]. Slic3r has many adjustable settings that control how a CAD model is fabricated. Some of the adjustable settings that determine the produced G-code include layer height, deposition speed, solid/infill patterns, and many others. Validation parts were constructed using PP MEX filament obtained from Gizmo Dorks with a standard diameter of 1.75 mm and PPS monofilament with a diameter of 1.4 mm. An extrusion multiplier of 1.5 was used when printing with PPS to compensate for the smaller diameter.

Since Watanabe et al. showed that process variable settings, such as deposition speed and layer height affected part warpage in PP [40], a consistent set of process variables was used in the simulation and experimental work. The values of those process variables are given in Table 3.2. PPS and PP parts were fabricated using the process variables in Table 3.2. A slower deposition speed than that used for PP was chosen to reduce drool and improve surface finish. The deposition temperature was increased from 220 °C to 290 °C to accommodate the higher melting temperature of PPS, 280 °C, and the build platform temperature was increased from 80 °C to 85 °C. The deposition length was increased to 10 mm to better represent the scale of typical MEX parts without significantly increasing the computation time of the simulation models. Significantly larger deposition lengths would have resulted in much larger simulation model computation times.

Table 3.2: Process variable settings for process simulation models

Process variable setting	**PPS**	**PP**
Environmental temperature	20 °C	
Deposition temperature	290 °C	220 °C
Build platform temperature	85 °C	80 °C
Deposition length	10 mm	5 mm
Deposition speed	15 mm/s	20 mm/s
Layer height	0.2 mm	

3.3 Results and discussion

3.3.1 PPS process simulation models and experimental validation

The sequential simulation models demonstrated the MEX process of PPS. Figure 3.9 shows the temperature distribution and shape of the first road as it was deposited on the build platform in the first simulation model. Due to the higher deposition temperature used with PPS in this simulation model, the thermal gradients present in the first road deposition were larger than the thermal gradients when depositing PP in previous work. The slower deposition speed, 15 mm/s versus 20 mm/s, resulted in a longer deposition time. This contributed to an increase in thermal gradients in the road. The longer deposition length, 10 mm versus 5 mm, also resulted in a longer deposition time, allowing deposited sections more time to cool during the deposition step. The final result of the first road deposition of PP is compared to PPS in Figure 3.10. Table 3.3 shows the differences in temperatures seen in the first road deposition.

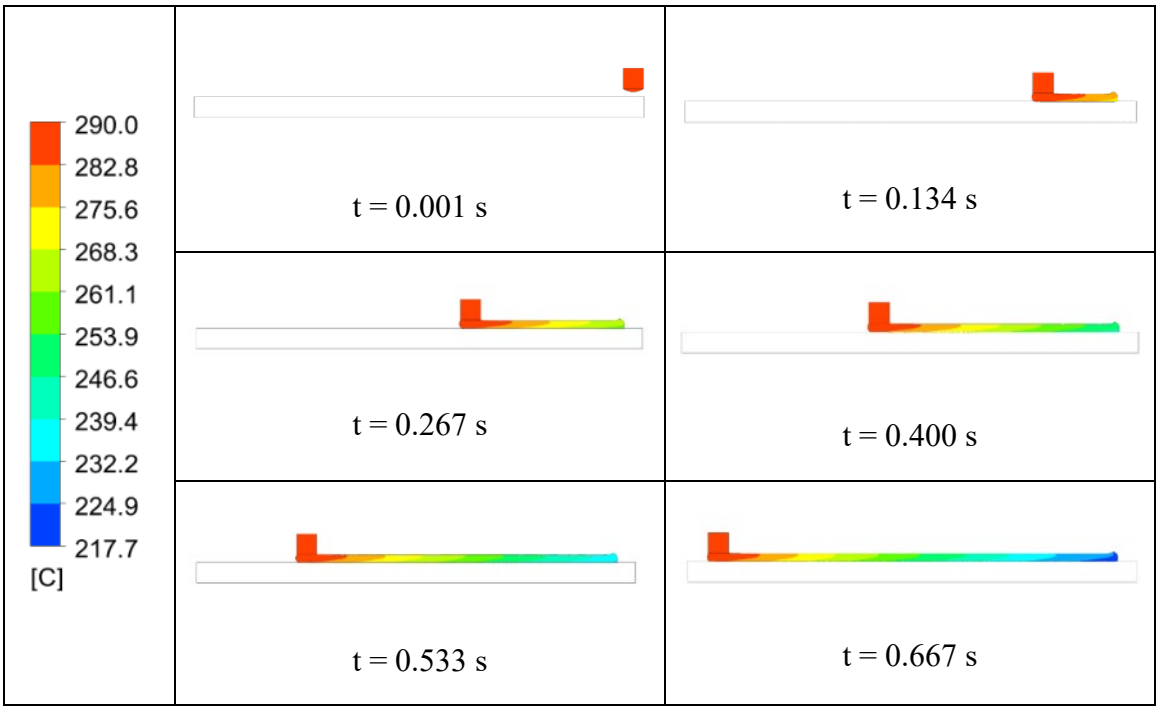

Figure 3.9: Temperature distribution and filament shape during road 1 deposition of PPS. As road 1 was deposited, it experienced convective cooling with the environment at 20 °C and conductive cooling with the build platform at 85 °C.

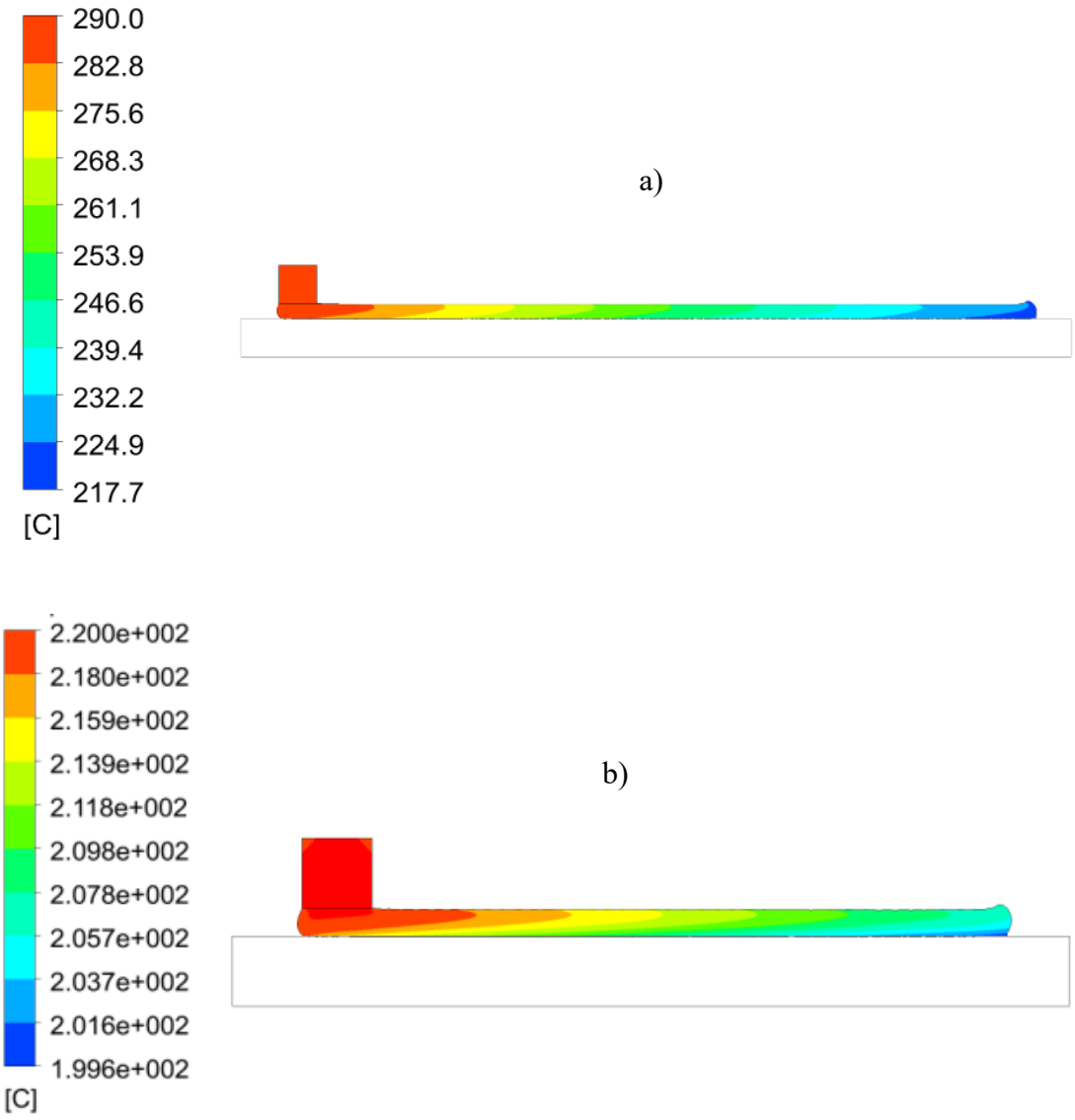

Figure 3.10: Final geometry and temperature distribution in road 1 deposition for a) PPS and b) PP [40]. The higher extrusion temperature, longer deposition length, and slower deposition speed used with PPS result in a larger temperature gradient in the PPS road 1.

Table 3.3: Temperatures seen in road 1 deposition in the PPS and PP process simulation models [40]

Temperature	PPS	PP
T_{max}	290.0 °C	220.0 °C
T_{min}	217.7 °C	199.6 °C
ΔT	72.3 °C	20.4 °C

During the cooling step, the first layer cooled for 1.67 seconds during which the build platform moved horizontally back to its original position and indexed downward to prepare for the second road deposition. The deposition nozzle was not in contact with the road during cooling. The first road was deposited at 290 °C and cooled to approximately 100 °C in 0.239 seconds. In the previous study with PP, the first road was deposited at 220 °C and cooled to approximately 122 °C in 0.25 seconds [40]. The faster cooling seen in PPS is due to the larger difference between the deposition temperature and the environmental temperature.

The temperature distributions and filament shapes during the second road deposition and roads 1 and 2 cooling are shown in Figure 3.11 and Figure 3.12, respectively. The procedure for this simulation model was similar to the procedure described for the first road deposition and cooling. During the second road deposition, conductive heat transfer occurred between road 1 and road 2. The two roads were then allowed to cool for 10 seconds to allow the roads to cool completely from their deposition.

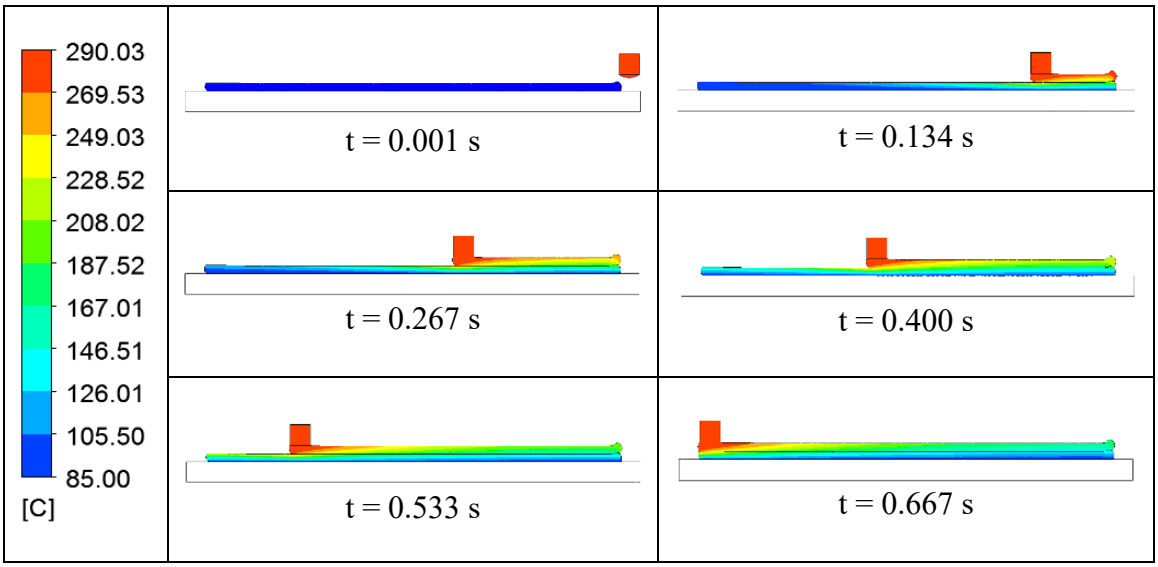

Figure 3.11: Temperature distribution and road geometries during road 2 deposition of PPS. Road 2 deposition began with a completely cooled road 1 at 85 °C. When road 2 made contact with road 1, conductive heat transfer occurred between the two roads and road 1 increased in temperature. As the deposition proceeded, the two layers began to cool together through convective cooling with the environment and conductive cooling with the build platform.

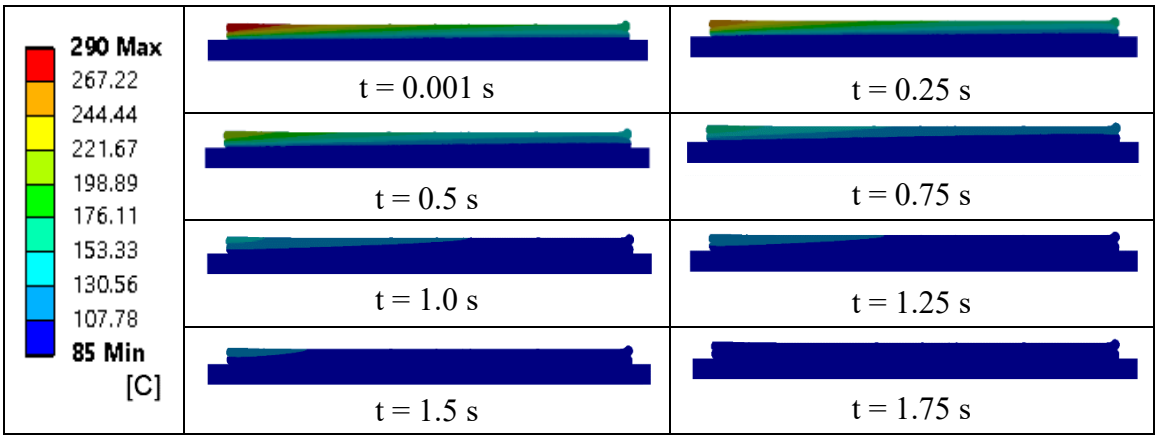

Figure 3.12: Temperature distribution during road 1 and 2 cooling of PPS. After road 2 deposition, the deposition nozzle moves off the geometry and the two roads begin cooling together through convective cooling with the environment and conductive cooling with the build platform. The roads are allowed to cool for 10 seconds, but they cool completely in 1.75 seconds.

The last simulation model was performed in ANSYS® Mechanical to predict the thermally-induced residual stresses and part warpage caused by the crystallization of the material during cooling. During road 2 deposition, road 1 was reheated as it came in contact with road 2 as shown in Figure 3.11. Road 2 and the reheated road 1 then cooled together and crystallized causing warpage and simultaneously inducing residual stresses. The part warpage and residual stresses of the two deposited roads are shown in Figure 3.13 and Figure 3.14, respectively. In Figure 3.13, the part warpage is shown in the two roads by measuring the deformation of the edges of the road from the build platform. At the edges, PPS showed a warpage of 0.017 mm. The inset in Figure 3.13 shows the warpage to scale while the main figure is shown at a magnified scale so that the shape produced by the warpage can be visualized. Figure 3.14 shows that minimal residual stresses were developed in the PPS roads during cooling. As a result, little warpage was observed, especially when compared to the warpage of 0.100 mm exhibited by PP in previous work by Watanabe et al. [40].

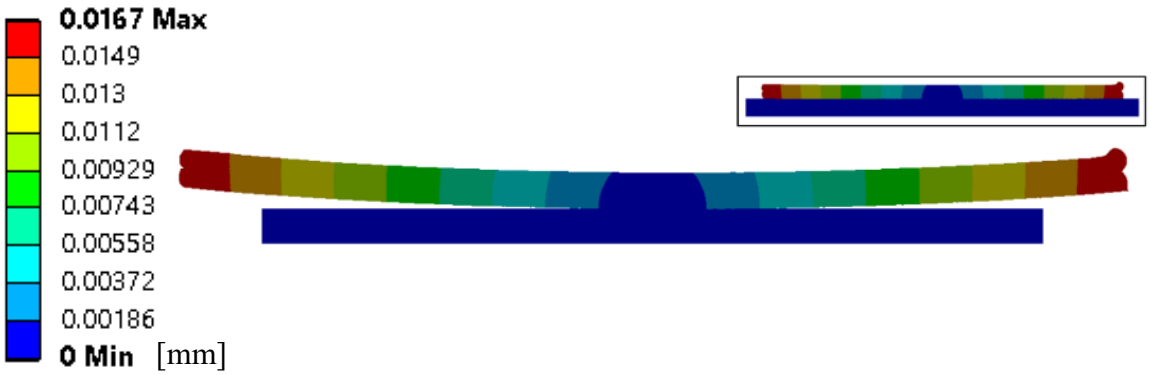

Figure 3.13: Warpage exhibited by PPS in the process simulation model performed in ANSYS® Mechanical. PPS roads 1 and 2 exhibited a warpage of 0.017 mm after cooling together for 10 seconds. The inset shows the geometry to scale while the main figure is scaled by a factor of 10 to show the shape the warpage exhibited.

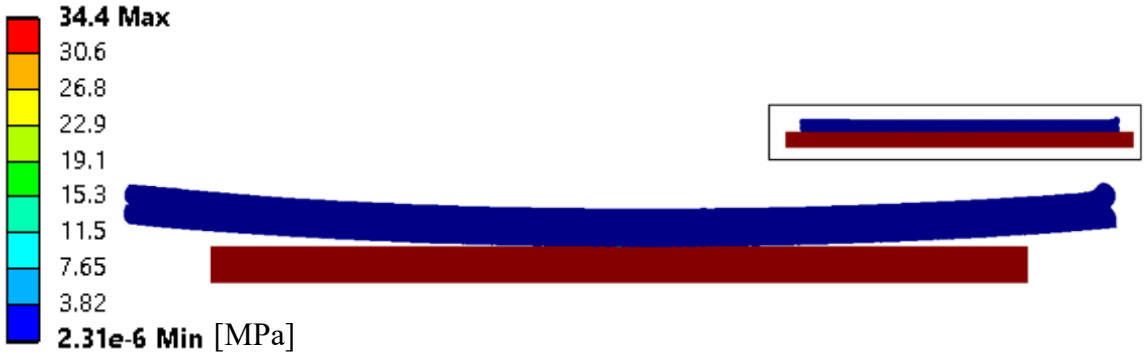

Figure 3.14: Residual stresses in road 1 and 2 at steady state. PPS roads 1 and 2 exhibit minimal residual stress after cooling. The inset shows the geometry to scale while the main figure is scaled by a factor of 10 to show the shape the warpage exhibited.

Because the process simulation models were computationally intensive, only two layers that were 10 mm long were simulated. In order to validate the model, PPS MEX parts were fabricated using the HYREL System 30. The fabricated parts were 0.4 mm tall

and 0.5 mm wide and were made using two - 0.2 mm tall layers to match the process simulation models. They were fabricated with several lengths including 10 mm, 20 mm, 40 mm, and 80 mm. The 10 mm long road matched the geometry that was modeled using the PPS process simulation models. Additional geometries were fabricated with PPS and PP to match the experimental validation used by Watanabe et al. [40]. The geometry in that work was a 20 mm by 20 mm rectangle that was 1 mm tall (5 layers). The different part lengths led to differences in absolute warpage values between the process simulation models and the fabricated parts, so the warpage values determined from the process simulation model were extrapolated to longer deposition lengths.

This extrapolation was performed by assuming that the radius of curvature of the part was constant. The radius of curvature, r, was calculated using Equation 3.6:

$$r = \frac{H}{2} + \frac{W^2}{8H} \tag{3.6}$$

where W is the deposition length and H is the warpage calculated using the process simulation models. The radius of curvature was calculated for PPS and PP using the warpage results obtained from the process simulation models [40]. These radii were then used to calculate the warpage for varying deposition lengths. The larger radius of curvature for PPS corresponded to lower warpage values when compared to the smaller radius of curvature of PP. The simulation models predicted that for a 10 mm long part, PPS would warp 0.017 mm while PP would warp 0.100 mm. Following the simulation model predictions, a 40 mm long PPS part with two layers should warp 0.270 mm and a PP should warp 1.537 mm. Additional layers would cause these warpage values to increase.

As previously described, warpage experienced by MEX parts causes them to separate from the build platform during fabrication. This behavior was observed by Watanabe et al. [40]. However, when fabricating PPS parts with MEX, no warpage was visible for any of the fabricated geometries and the entire part remained completely adhered to the build platform. This implied that there were minimal residual stresses present in the fabricated part, which was consistent with the results obtained by the process simulation model. A 20 mm by 20 mm by 1 mm PPS part that was fabricated is shown in Figure 3.15. The figure shows that the part did not warp or detach from the build platform during printing. For comparison, a 20 mm by 20 mm by 1 mm PP part was also fabricated. As shown in Figure 3.15, the part detached from the build platform during printing, implying that there were residual stresses present in the part. These results are consistent with what was observed previously [40].

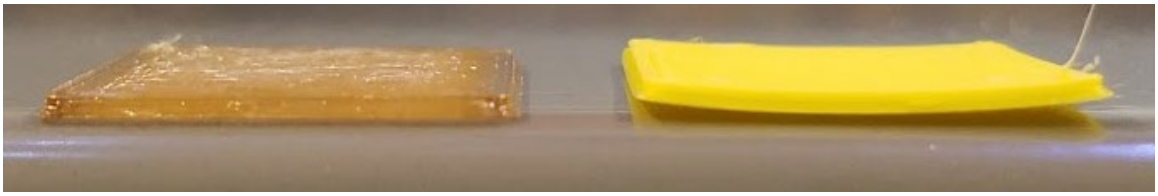

Figure 3.15: Validation parts were printed using PPS and PP. MEX was used to fabricate 20 mm x 20 mm x 1 mm parts with PPS (left) and PP (right). The PPS part exhibited no visible warpage and remained adhered to the build platform for the duration of printing. The PP part warped and separated from the build platform during printing.

3.3.2 Parametric studies based on material properties

The parametric studies of the warpage simulation model were conducted by changing the material parameters in the PPS process simulation models to determine which material properties affected part warpage. Values for PP were used in addition to other logical values. The material properties of interest were CTE, thermal conductivity, heat capacity, and Young's modulus. Table 3.4 shows the warpage value obtained from the PPS process simulation models with varied material parameters and how those material parameters compare to the original PPS value. It also shows the comparison of the warpage values from the warpage value of 0.017 mm obtained using the base PPS process simulation models.

Table 3.4: Warpage of PPS process simulation models with adjusted material properties.

PP parameter used with PPS simulation model	**Warpage (mm)**	$\frac{Parameter_{PP}}{Parameter_{PPS}}$	$\frac{Warpage_{parameter}}{Warpage_{PPS}}$
CTE	0.050	2.98	2.98
Thermal conductivity	0.017	0.69	1.01
Heat capacity	0.017	1.92	1.00
Young's modulus	0.017	0.39	1.00

The CTE showed direct scaling with the warpage value in the process simulation models. In the PPS process simulation models, when the CTE was increased by a factor of 2.98, the warpage value obtained also increased by a factor of 2.98. Changing the thermal conductivity, heat capacity, and Young's modulus by factors of 0.69, 1.92, and 0.39, respectively, did not significantly affect the warpage seen in the process simulation models.

The warpage vs. deposition length plots for PP, PPS and the PPS process simulation with a modified CTE value are shown in Figure 3.16.

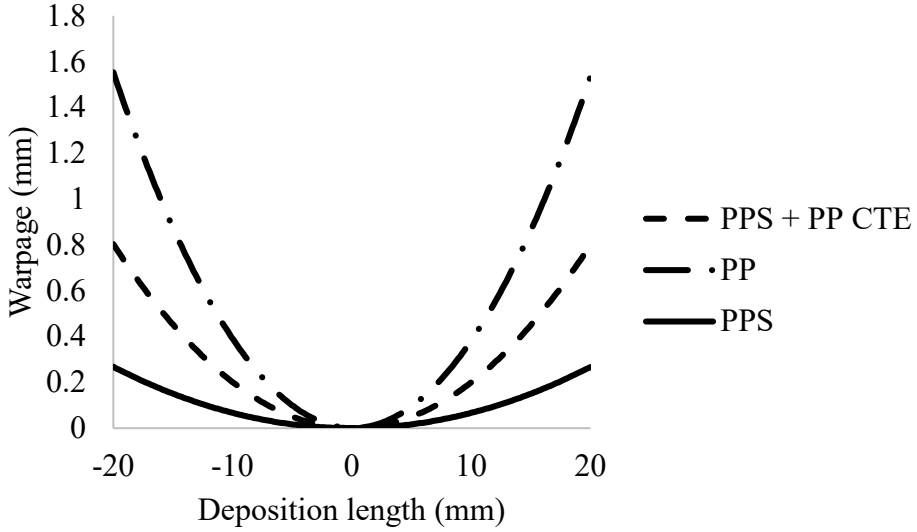

Figure 3.16: Warpage vs. deposition length plots for PP, PPS, and CTE modified PPS. The warpage value obtained using the process simulation models was used to extrapolate the warpage values at other deposition lengths. The PP simulation model exhibits more warpage than both the PPS simulation model and the PPS simulation model that used the CTE of PP.

The effects of changing multiple material properties at once were studied using different combinations of CTE, thermal conductivity and heat capacity values in the PPS process simulation model. Table 3.5 shows the warpage value obtained for the simulations along with how it compares to the warpage value from the base PPS process simulation models.

Table 3.5: Warpage of PPS simulation models with multiple adjusted material properties.

PP parameter used with PPS simulation model	Warpage (mm)	$\frac{Warpage_{parameter}}{Warpage_{PPS}}$
CTE + thermal conductivity	0.051	3.04
CTE + heat capacity	0.050	2.99
Thermal conductivity + heat capacity	0.017	1.01
CTE + thermal conductivity + heat capacity	0.051	3.03

As seen in Table 3.5, some material parameters have a more significant effect on warpage when changed in conjunction with another material parameter. Thermal conductivity appeared to have a more significant impact on warpage when combined with effects from CTE. When modifying CTE and heat capacity together, the warpage seen was slightly larger than what was seen with CTE alone. However, it did not appear that the contribution from heat capacity increases when combined with thermal conductivity.

Based on the results seen by varying the material parameters of PPS to values of PP, additional values for the CTE, thermal conductivity, and Young's modulus were explored based on work done with polymer composites. An additional CTE value was used to confirm its direct scaling with warpage. Additional values for thermal conductivity and Young's modulus were chosen in order to assess if different values could more significantly affect the warpage of PPS.

Fillers have been used in various polymer systems to modify the thermal and mechanical properties of the combined system, or polymer composite [94]. Fillers in polymer composites can have various structures, such as particles or small fibers, and can

be used in various loading amounts. Both inorganic and organic fillers have been employed such as carbon nanotubes, metal powders, cellulose nanocrystals, and glass fiber.

The CTE has been lowered by fabricating polymer composites with inorganic fillers with low thermal expansion values. Specifically, the addition of aluminum nitride (AIN) lowered the CTE and simultaneously increased the thermal conductivity of polyethylene polymer composites [95]. Lee et al. [95] showed a decrease in the CTE of polyethylene from 198 ppm/°C to 31.7 ppm/°C with the use of surface treated AIN fillers. This value is significantly lower than the values for PPS and PP. A CTE value of 31.7 ppm/°C was used in the process simulation models for PPS.

The thermal conductivity of polymers is lower than the thermal conductivity of metals and many other inorganic materials. The thermal conductivity of polymers is typically in the range of 0.1 to 0.5 W/(m-K) while metals can have values as much as 3 orders of magnitude higher [94]. The thermal conductivity of polymers can be increased through the use of fillers with high thermal conductivities, such as metal or carbon fillers. Carbon nanotubes have attracted much interest as a filler for this purpose due to their high thermal conductivity (theoretically > 6000 W/m-K) [96]. Although the carbon nanotubes do not increase the thermal conductivity of polymer matrices as much as predicted by the rule of mixtures, the thermal conductivity of polymer composites has been doubled with the introduction of carbon nanotubes [97]. Based on this possibility, the thermal conductivity value for PPS was doubled and used in the simulation model with the other PPS material parameters.

The addition of particles to polymers can increase the Young's modulus of the polymer matrix. The use of various discontinuous organic and inorganic fillers have been studied for this purpose and the effect of filler loading on the modulus can be modeled using the Guth-Gold model given in Equation 3.7.

$$\frac{E}{E_s} = (1 + 2.5\varphi + 14.1\varphi^2) \tag{3.7}$$

where E_s is the modulus of the polymer and ϕ is the filler volume fraction [98]. The use of AIN particles in polyvinylidene fluoride increased the modulus from 2.2 GPa to 15.51 GPa [99]. This value is much larger than the Young's modulus of PP and PPS. A Young's modulus value of 15 GPa was used in the simulation model with the other PPS material parameters.

Based on previous work with polymer composites, new values of CTE, thermal conductivity, and Young's modulus were used in the PPS process simulation models to further examine the effect of these material properties on part warpage. Table 3.6 shows the new material parameters used in the PPS simulation models, how they compare to the original material parameters, and how the warpage of the models was changed based on those values.

Table 3.6: Warpage of PPS simulation models with additional adjusted material properties

Adjusted parameter used with PPS simulation model	Warpage (mm)	$\frac{Parameter_{adjusted}}{Parameter_{PPS}}$	$\frac{Warpage_{adjusted}}{Warpage_{PPS}}$
CTE	0.011	0.63	0.63
Thermal conductivity	0.017	2.00	0.99
Young's modulus	0.017	3.33	1.00

The warpage value obtained from the simulation using the additional CTE value confirmed that the warpage directly scales with CTE. Even though the thermal conductivity was changed more significantly in this set of simulations, it still had a minimal effect on the part warpage. Doubling the thermal conductivity only decreased the warpage to 99% of its original value. Consistent with what was shown before, changing Young's modulus did not significantly affect the part warpage seen in the simulation.

3.3.3 Modeling material properties as a function of temperature

In the developed process simulation models, only viscosity was modeled as a function temperature even though many of the material property inputs for the models are not constant values over the studied temperature range. Because of the computational expense of modeling all the inputs as functions of temperature and the lack of experimental data detailing their dependence on temperature for PPS, many of the material properties could not be expressed as functions of temperature in the process simulation models. The parametric studies on the material properties in section 3.3.2 showed that CTE was the most influential material property input that determined MEX part warpage and

deformation characteristics. The relationship between CTE and temperature is well defined for PPS [100], so additional process simulation models were developed in which CTE was modeled as a function of temperature according to Equation 3.8.

$$CTE(T) = \begin{cases} 10.9 \times 10^{-5}, & T < 90 \\ 4.6 \times 10^{-5}, & T \geq 90 \end{cases} \tag{3.8}$$

The user defined function (UDF) capability in ANSYS® Polyflow allows value parameters, such as material properties, to be defined as functions of other quantities. In ANSYS® Mechanical, the piecewise function describing CTE was inputted in the Engineering Data Tabular capability. The use of these capabilities increased the computational time of the process simulations by 290%. The obtained warpage value was 0.015 mm, which was 12% lower than the base simulation warpage value or 0.017 mm. A large difference was not seen between the obtained warpage values because the CTE of PPS was constant for the majority of the examined temperature range of 85 °C to 290 °C.

3.4 Conclusions

In this study, the MEX process was modeled in three phases: road 1 deposition and cooling, road 2 deposition and cooling, and residual stress and warpage. The results seen in the deposition and cooling of two polymer MEX roads were consistent with process simulation models conducted previously. The temperature distribution for PPS was larger than that seen in PP and the observed cooling rates were larger. These differences were attributed to different deposition temperatures, lengths, and speeds. In the PPS process

simulation models, a higher deposition temperature, longer length, and slower deposition speed were used which resulted in larger thermal gradients throughout the MEX part.

The difference in warpage between PP and PPS experimental parts was investigated using the process simulation models. Various material properties of PPS were adjusted to the values for PP to determine their effect on part warpage.

- Decreasing the CTE decreased part warpage by the same factor.
- Changing the thermal conductivity did not appear to have a significant effect on part warpage.
- Changing heat capacity did not appear to have a significant effect on part warpage.
- Changing the Young's modulus did not appear to have a significant effect on part warpage.

Additional values for the CTE, thermal conductivity, and Young's modulus were investigated for the PPS simulation models based on existing methods used to modify these values in polymer composites. The addition of fillers has shown to decrease the CTE, increase the thermal conductivity, and increase the Young's modulus. These modifications all led to a decrease in MEX part warpage in the simulation models. In addition, CTE was modeled as a function of temperature and similar warpage values were obtained compared to the original model. Overall, these process simulation models provide insight into which material properties most affect MEX part warpage. In addition, they provide a means to determine how fillers used in polymer composites could affect their performance in the MEX process. Understanding the relationships between material properties and final part

deformation characteristics facilitates new material development strategies in order to expand the materials available for MEX.

CHAPTER 4. FAST SCANNING CALORIMETRY FOR SEMICRYSTALLINE POLYMERS IN MEX

4.1 Background

MEX parts experience cycles of heating and cooling during their fabrication as layers of liquefied thermoplastic are deposited to fabricate the three-dimensional part. Previous studies have shown the influence of temperature evolution during fabrication on MEX part properties. Temperature management during fabrication has been shown to affect the thermally driven bonding process between roads and layers [15-17, 81, 84, 86, 101, 102], and temperature gradients have been shown to induce residual stresses and strains resulting in part warpage [22, 84-86, 102, 103]. Because of the direct influence of temperature on MEX part properties, it is essential to understand thermal history during the MEX process.

Previous work regarding direct measurement and analytical modeling of temperatures experienced during MEX has shown cycles of high heating and cooling rates associated with the additive build process [15, 16, 79, 82, 84, 85, 102, 103]. Direct measurement of the temperatures experienced during FDM is limited and has been primarily focused on parts using ABS with a few examining PLA. Direct measurement has been performed by embedding k type thermocouples in the foam base plate of Stratasys systems [15, 16]. These studies showed that significant reheating occurred when depositing the first several layers of fabricated parts and reheating effects were seen in the bottom layers after over 15 successive layer depositions [15]. A deposition strategy with shorter

filament paths and increased build chamber temperature were shown to promote better bonding in parts through flexural testing. The increased bonding was the result of longer times above glass transition temperature [15]. The temperature history was also shown to vary within a part resulting in the lower layers showing better bonding strength due to their increased time above glass transition compared to subsequently deposited layers [16]. The thermal behavior within each layer was also showed to vary significantly [102]. K type thermocouples embedded in various position in the 7^{th} layer of a 13 layer ABS part showed that temperature variation was the highest at the edges of the fabricated part and was heavily dependent on tool path. The same reheating effects due to the additive deposition of layers was also demonstrated. An analytical finite element method (FEM) model developed in ABAQUS® in conjunction with the experimental work showed good agreement with the experimental data [102]. Fiber Bragg grating sensors have also been embedded in ABS MEX parts to monitor strain variations in addition to the use of k type thermocouples to monitor temperature changes [103]. Significant thermal strains were shown to develop in the first several layers due to cycles of heating and cooling and thermal variations within the entire part and within the individual layers.

Analytical techniques have also been employed to examine the effect of process parameters on temperature evolution within MEX parts. The element activation technique employed in ANSYS® showed the effect of tool path on temperature evolution and mechanical distortion in ABS parts fabricated with MEX [85]. The model showed temperature variations between and within layers and showed highest thermal stresses in the bottom layers, which was in agreement with the experimental work by Kousiatza et al. [103]. Numerical techniques have also been implemented using MATLAB that

demonstrated reheating effects within individual roads that depended on process parameters such as printing speed, filament dimensions, deposition sequence and environment temperature [82]. This work was extended to compute the adhesion quality between deposited rasters based on an algorithm that activated relevant boundary conditions based on previous work regarding bonding in ABS MEX parts [79]. A three-dimensional mathematical model was also developed for PLA that showed the reheating effects due to subsequent layer depositions were most significant in the layer thickness direction [84]. Increased layer height and print speed were shown to result in lowered cooling rates, but temperature settings, such as print temperature, build platform temperature and environment temperature, were concluded to be the most influential on the overall temperature variation within an MEX part.

Analytical and experimental studies with MEX fabrication show that the successive deposition of adjacent roads and layers causes previously deposited and cooled material to reheat to temperatures up to the print temperature. The exact thermal history seen by the part varies within the geometry and is affected by the many MEX process variable settings. The rates of the cooling have been estimated to be up to hundreds of degrees per second [21, 40, 49, 77, 84, 104]. While fast cooling rates are advantageous to prevent sagging or drooping as the polymer road solidifies quickly after deposition, the short times that the polymer remains above its glass transition temperature result in partial bonding between roads and layers [17, 77, 79, 83]. Elevated build chambers and build platforms have been utilized to decrease cooling rates in order to increase bonding and decrease temperature gradients within parts, resulting in increased mechanical properties and decreased part warpage [15, 77, 84].

The extension of MEX to semicrystalline polymers has unique challenges with these fast cooling rates and cyclic heating compared to amorphous systems. In semicrystalline polymers, cooling rate has been shown to affect the level of crystallinity developed [105]. Sufficiently high cooling rates have been shown to limit crystallization in semicrystalline polymers [105-110].

4.1.1 Differential scanning calorimetry

The percent crystallinity of semicrystalline polymers can be measured using differential scanning calorimetry (DSC), a common thermal analysis technique. In DSC, the enthalpy of melting, ΔH_m, is calculated and compared to the theoretical enthalpy of melting of a 100% crystalline material, ΔH_m^o, as shown in Equation 4.1.

$$\% \, crystallinity = \frac{\Delta H_m}{\Delta H_m^o} \times 100\% \tag{4.1}$$

In DSC, heating and cooling rates of 10 °C/min are typically used to measure thermal transitions and percent crystallinity. Semicrystalline polymers generally exist in a metastable state, and the relatively slow heating rates used with DSC can allow reorganization processes to occur during heating [105, 107, 111, 112]. Cold crystallization is a reorganization process that occurs upon heating between glass transition temperature and melting temperature. During this exothermic event, the material crystallizes and the degree of crystallinity increases [109, 113]. In other reorganization processes, crystallites become more perfect without the degree of crystallinity appreciably changing [112, 113].

Due to reorganization processes that occur during heating, the melting curve observed in DSC may not be representative of the original material [114]. The additional crystallinity developed during cold crystallization and the increased stability from perfected crystallites results in appreciably higher melting enthalpies and increased melting peak temperatures [112, 113, 115].

4.1.2 Fast scanning calorimetry

In order to suppress these reorganization phenomena and measure the melting temperature and percent crystallinity of the as-processed material, higher heating rates than what are capable with DSC are necessary [110, 115]. A recently developed technology, fast scanning calorimetry (FSC), is a DSC that uses a chip sensor based on micro-electro-mechanical system (MEMS) technology. MEMS technology and the use of small samples (<500 ng) facilitates the use of fast heating and cooling rates of 1000s of °C/s [105, 116]. These devices were originally developed by researchers to investigate materials far away from their thermodynamic equilibrium or produce materials with advanced and novel properties that were unrealizable without fast heating and cooling rates [110, 116, 117]. Because most modern materials are used in non-equilibrium states, it is essential to study their behavior over a range of thermodynamic states [110].

Fast heating rates have been shown to suppress reorganization processes in various semicrystalline polymers such as polyethylene terephtahale (PET), isotactic PP, PEEK, and polyethylene (PE) [106, 108, 111, 118-122]. Using conventional DSC on semicrystalline polymers, multiple melting peaks have been observed [114, 123-126]. These multiple

melting peaks have been theorized to be the result of multiple crystallite populations, but the use of FSC has shown that in some cases the multiple peaks resulted from a reorganization phenomena known as melting-recrystallization-remelting. In this behavior, as some crystals melt, they have chain segments that still possess some localized order in the melt and quickly recrystallize to form more stable lamellae [113, 122]. These more stable lamellae eventually melt at higher temperatures. As the heating rate was increases, the highest of the observed melting peak shifts to lower temperatures and decreases in size while the lower peaks move to higher temperatures and increase in size until only one peak is observed [120, 121]. The lower temperature melting peak results from two opposing processes: the endothermic melting of initial crystallites and the exothermic recrystallization process. With increasing heating rate, the time allowed for recrystallization decreases so the exothermic contribution of recrystallization also decreases. The decrease in exothermic recrystallization therefore leads to an increase in the peak area and the peak position. In addition, the material that was still able to recrystallize will be less perfect than at longer times and its content will be smaller, so the higher melting peak will decrease in area and its peak position will shift to lower temperatures [113, 120, 121]. The use of a sufficiently fast heating rate prevents the melting-recrystallization-remelting phenomena allowing the melting behavior of the original material to be studied. The presence of this recrystallization process has been confirmed with other experimental techniques such as small- and wide-angle X-ray scattering (SAXS and WAXS) [125, 127], transmission electron microscopy (TEM) [128], and atomic force microscopy (AFM) [129].

The high cooling rates have also been used to prevent the formation of crystallinity in semicrystalline polymers [105, 108, 109, 117, 130-148]. Depending on the crystallization kinetics, some polymers can be made amorphous using standard DSC cooling rates, such as PET and PLA [149]. Linear polymers that are very fast crystallizers, such as linear PE, are very difficult to cool to an amorphous state even with FSC [106]. Table 4.1 shows the critical cooling rates to prevent the formation of crystallinity in many semicrystalline polymers using FSC.

Table 4.1: Critical cooling rate to prevent crystallization in different semicrystalline polymers determined using FSC.

Polymer	Critical cooling rate to prevent crystallization [°C/s]	Reference
PLA	0.5	[130, 131]
PET	2 3	[133] [105]
Isotactic polybutene-1 (iPB-1)	10	[147]
Poly(butylene succinate) (PBSu)	70	[139]
PA 6	150	[105, 138, 146]
Polybutylene terephthalate (PBT)	200	[105, 132, 142, 143]
PCL	500	[141]
PA 11	500	[135]
PA 66	500-1000	[134]
Isotactic PP	1000	[108, 109, 143, 144]
Polybutylene naphthalate (PBN)	>2000	[145]
PVDF	>6000 100,000	[148] [137]
Polytetrafluoroethylene (PTFE)	>1,000,000	[136]
High-density PE	>1,000,000	[117, 140]

By cooling at sufficiently fast cooling rates, a completely amorphous material can be achieved without any homogenously formed nuclei. The amorphous material allows the study of kinetics of both non-isothermal and isothermal crystallization at all relevant cooling rates and temperatures [109, 132, 150-152]. Using traditional DSC, the analysis of crystallization kinetics at high supercooling is often impossible since the material may crystallize during cooling to the target temperatures. The study of crystallization kinetics over a wide range of crystallization temperatures using FSC and DSC together has shown that there is a change of the primary crystal nucleation mechanism at different crystallization temperatures in numerous polymer systems, such as PP, PCL, polybutylene terephthalate (PBT), and several PA [105, 132, 134, 135, 141-143, 150, 153-157]. In addition, nucleation kinetics have been studied using FSC [158-163]. FSC is one of the few available techniques that can cool sufficiently fast to prevent heterogeneous nucleation and enforce homogeneous nucleation. Previously, the study of homogeneous nucleation was primarily observed in droplet experiments with slow cooling [164-167]. The use of FSC can follow the growth of homogeneous nuclei to crystals until impingement in bulk samples while only one homogeneously formed nucleus was commonly used in small droplet experiments [141, 162, 163, 168].

In addition, understanding the effects of polymer processing operations on morphology is important to predicting the final part properties. However, polymer processing techniques often experience cooling rates that are several orders of magnitude faster than rates available using conventional DSC [108, 110]. Because of the high cooling rates experienced during polymer processing operations, metastable states far away from equilibrium are often formed in polymers which are difficult to study with conventional

characterization techniques [169]. The heating and cooling rates available to FSC make it a suitable technique for examining polymer morphology resulting from processing conditions [108, 110].

4.1.3 Key research objectives

The use of FSC to mimic thermal processing conditions can be extended to replicate the conditions in MEX. Therefore, the objective of this research was to evaluate FSC as a technique for replicating the conditions in MEX utilizing its high heating and cooling rates. The effect of these heating and cooling rates on crystallization of semicrystalline polymers was examined. PPS was used as a case study material and experimental results were compared to previous work performed with PP. Based on the cooling rates modeled in CHAPTER 3, it was hypothesized that the thermal exposure during the MEX process could hinder the crystallization behavior of PPS.

4.2 Materials and methods

PPS in monofilament form with a diameter of 1.4 mm was used as the printing feedstock and was dried in a cuum oven at 100 °C for 3 hrs. before printing. Printed samples for examination with DSC were fabricated using the HYREL System 30 from HYREL International, described in section 3.2.4 [91].

4.2.1 Differential scanning calorimetry experiments

DSC samples were cut from the center of a 40 mm by 40 mm part with a height of 0.4 mm, fabricated with 100% rectilinear infill with a layer height of 0.2 mm. The build platform was held at 80 °C, and the print temperature was 290 °C. The build area was enclosed at room temperature.

DSC experiments were performed using a TA Instruments Discovery DSC. A procedure based on ASTM E794 was used to determine the melting temperature and percent crystallinity as defined in Equation 4.1. The sample was heated at 10 °C/min from 25 to 330 °C in a nitrogen environment. The sample was held isothermally for 5 min before cooling to 25 °C at 10 °C/min. Samples were prepared in standard aluminum pans.

Annealing studies were also performed using conventional DSC at possible build chamber temperatures for MEX to examine if isothermal crystallization could occur. The sample was heated from 25 to 330 °C in a nitrogen environment and held isothermally for 5 min to ensure full melting. Next, it was cooled to the desired annealing temperature at a rate of 85 °C/min (1.4 °C/s) and held isothermally for 5 min. The sample was then cooled to 25 °C at a rate of 85 °C/min (1.4 °C/s) and heated to 330 °C at 10 °C/min to measure the percent crystallinity developed in the sample using the melting enthalpy and Equation 4.1. For PPS, the studied build chamber temperatures were 85, 90, and 95 °C. These temperatures were selected to be at the onset, midpoint, and endset of the glass transition. Additional higher temperatures, 100, 110, and 120 °C were also investigated based on the results from the lower temperatures. The theoretical enthalpy of melting of 100% crystalline PPS used in this work was 79.8 J/g [170].

4.2.2 Fast scanning calorimetry experiments

FSC was performed on the commercially available Flash DSC 1 from Mettler Toledo using MultiSTAR UFS 1 sensor chips made by Xensor Integration. The STARe software version 10.00d was used for analysis. A razor blade microtome was used to cut a thin slice of the PPS monofilament with a thickness of about 20 μm. The slice was further cut down to a small grain using a razor blade. A hair with a native tip was used to pick up and transfer the PPS grain to the UFS1 sensor. The sample was then adhered to the chip by heating to 350 °C at a rate of 50 °C/s. The mass of the sample was estimated by examining the step height of the specific heat capacity at the glass transition for a completely amorphous sample [171]. This value was used in Equation 4.2,

$$m = \frac{\Delta c_{p,a}}{\Delta c_p} \tag{4.2}$$

where $\Delta c_{p,a}$ is the step height of the specific heat capacity of the glass transition in J/°C for a completely amorphous sample measured using FSC and Δc_p is the step height of the specific heat capacity for amorphous PPS in J/°C-g. This value was determined using equations for heat capacity as a function of temperature defined by Cheng et al.[172]. The mass estimated from Equation 4.2 was 505 ng.

Before all subsequently described FSC procedures, a heating step of 50 °C/s, isothermal hold of 2 seconds at 350 °C, and a cooling step of 4 °C/s to 30 °C were performed in order to erase the thermal history of the material. After the procedures, the same set of steps was performed and the melting behavior was analyzed to ensure the

sample did not degrade during testing. Degradation of the sample would result in changes in the melting temperature [171].

4.2.2.1 Critical heating rate to prevent reorganization

In order to determine the critical heating rate necessary to suppress reorganization processes, cycles of heating above the melting temperature at increasing rates and cooling back to room temperature at a constant rate were performed. The temperature range used for PPS was 30 °C to 350 °C. A sufficiently low cooling rate was used in order to ensure crystallization of the material. For PPS, the cooling rate used was 4 °C/s. The heating rates examined were 50, 100, 200, 300, 400, 500, 600, 700, 800, 900, 1000, 2000, 3000, 4000, and 5000 °C/s. Isothermal periods of 2 seconds were used between each heating and cooling step. The melting peak temperature for each heating rate was recorded to determine at what heating rate reorganization processes were suppressed. Reorganization processes lead to increases in melting temperature [105, 108]. Therefore, with increasing heating rates, the melting temperature is expected to decrease until the critical heating rate is reached where all reorganization is prevented [105, 106, 108, 111]. As heating rate continues to increase, increases in the melting temperature are again observed as thermal lag in the material increases at very high heating rates [105, 106].

4.2.2.2 Critical cooling rate to prevent crystallization

The critical cooling rate for prevention of crystallization in a semicrystalline material was determined using the critical heating rate to suppress reorganization

processes. Cycles of heating above melt temperature at the critical heating rate and cooling back to room temperature at increasing rates were performed. The same temperature range used when determining the critical heating rate was utilized for critical cooling rate examination. The cooling rates examined with PPS were 1, 2, 3, 4, 5, 6, 7, 8, 9, 10, 20, 30, 40, 50, 60, 70, 80, 90, and 100 °C/s. The critical cooling rate for prevention of crystallization of the material was determined by observing the melting peak. The enthalpy of melting decreased as percent crystallinity decreased and disappeared when an entirely amorphous material was achieved with sufficiently high cooling rate. Depending on the material, different cooling rates than those examined with PPS may be required to achieve an amorphous material.

4.2.2.3 Annealing studies at possible build chamber temperatures

Annealing studies on FSC were performed at possible build chamber temperatures for MEX, similar to the studies performed with conventional DSC. In these tests, the sample was heated above the melting temperature at the critical heating rate, held isothermally for 5 seconds, cooled at the critical cooling rate to the annealing temperature, and held at that temperature for 5 minutes. The sample was then cooled to room temperature at the critical cooling rate and then heated above melting temperature again at the critical heating rate to examine the crystallinity developed during annealing. The temperatures examined for PPS were 85, 90, 95, 100, 110, and 120 °C.

4.2.2.4 Thermal cycling in MEX

The effect of heating and cooling cycles experienced during MEX on the crystallinity of PPS was examined using FSC. During MEX part fabrication, the successive deposition of material reheats previously deposited roads and layers. Thermal cycling was performed on the sample at a heating and cooling rate of 740 °C/s, the cooling rate estimated during MEX of PPS in CHAPTER 3 [49]. Multiple heating and cooling cycles were completed for four temperatures chosen below the print temperature of PPS: 240, 200, 160 and 120 °C. Decreasing temperatures were chosen to mimic the reheating of previously deposited layers that decreased in intensity as the nozzle moved further away from the base layer as the part height increased. A cycle consisted of heating from 100 °C to the chosen temperature at 740 °C/s. The sample was held isothermally for 0.1 seconds and then cooled back to 100 °C at 740 °C/s and held isothermally for 0.5 seconds. The temperature profile applied to the sample during a run with *n* cycles at each temperature is shown in Figure 4.1. Multiple cycles were performed at each temperature to mimic the nozzle passing by a point multiple times as additional roads were deposited within the same layer. Tests were performed with 10, 20, 30, 40 and 50 cycles at each temperature. After the completion of the cyclic heating, the sample was then cooled to room temperature at the critical cooling rate and then heated above melting temperature at the critical heating rate to examine the crystallinity developed during the heating and cooling cycles.

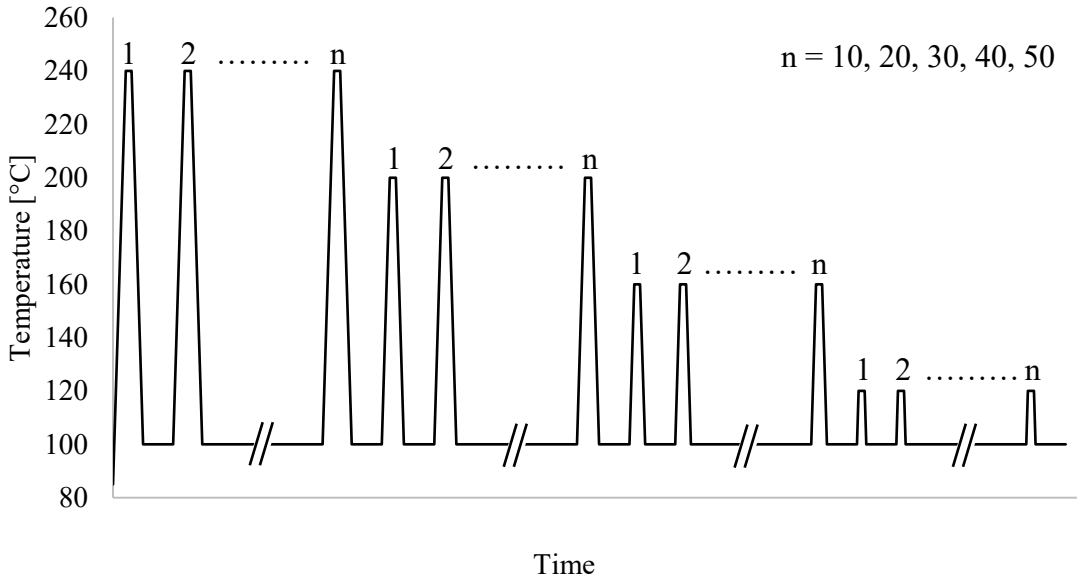

Figure 4.1: Temperature profile applied to the sample during FSC to mimic heating and cooling cycles experienced during FSC fabrication of PPS. Tests were performed with 10, 20, 30, 40 and 50 cycles at each temperature.

4.3 Results and Discussion

4.3.1 Differential scanning calorimetry

DSC was performed on the PPS part fabricated with MEX and the resulting curve is shown in Figure 4.2. An exothermic peak between the glass transition temperature (90 °C) and the melting temperature (279 °C) was observed during the heating curve. This exothermic peak, located at 134 °C with an enthalpy of 25.9 ± 0.8 J/g, showed that cold crystallization occurred in the MEX sample while it was heated at 10 °C/min during the testing. Therefore, the percent crystallinity obtained from the melt enthalpy was not reflective of the as-processed material. The percent crystallinity of the original sample was

estimated by subtracting the enthalpy of the cold crystallization peak from the melt enthalpy, resulting in a percent crystallinity of 15.1 ± 1.2%. However, this estimation generally underestimates the amount of crystallinity formed during cold crystallization because the enthalpy of melting of the 100% crystalline material is measured at the equilibrium melting temperature, while the enthalpy of crystallization is expected to be lower at lower temperatures [106]. As a result, the actual percent crystallinity of the PPS MEX part was likely lower than 15%. During the subsequent cooling cycle, an exothermic peak, representative of melt crystallization, was observed at 211 °C.

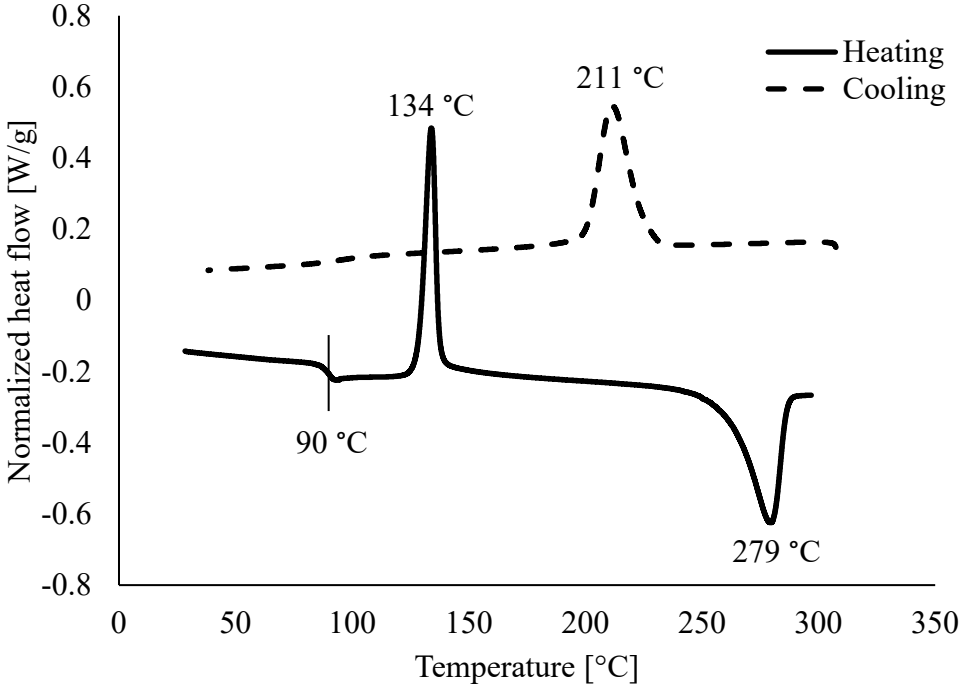

Figure 4.2: Heat flow data for a printed PPS part performed at a heating and cooling rate of 10 °C/min. Cold crystallization was observed during heating and is shown on the heating curve with a peak at 134 °C.

Annealing studies were performed using conventional DSC at possible build chamber temperatures for MEX. Figure 4.3 shows the cold crystallization peaks observed upon heating after annealing at the chosen temperatures, T_a. Table 4.2 gives their enthalpy values and the percent crystallinity for the samples calculated using Equation 4.1. During the 5 min annealing time for 85, 90, and 95 °C, no crystallization peak was observed. In addition, during the subsequent heating step above the melting temperature, a cold crystallization peak was observed. The enthalpy of the cold crystallization peak was similar for annealing temperatures of 85, 90, and 95 °C. A representative peak is shown in Figure 4.3. This cold crystallization peak observed after the isothermal treatment was smaller than the cold crystallization peak observed for an as-printed sample. The reduction of the cold crystallization peak implied that more crystallinity was developed in the sample compared to the as printed part. However, since no crystallization peak was observed during the annealing step, it was assumed that most of the crystallinity developed in the sample during the cooling from melt to the annealing temperature at a rate of 85 °C/min (1.4 °C/s).

Since little or no crystallinity occurred during the isothermal steps at 85, 90, or 95 °C, additional higher temperatures, 100, 110, and 120 °C, were investigated. At annealing temperatures 100 °C and 110 °C, no exothermic crystallization peak was observed during the annealing step, similar to the results seen at the lower temperatures. The cold crystallization peak seen upon heating after the isothermal treatment had an enthalpy similar to that observed at lower temperatures. A representative peak is shown in Figure 4.3. Isothermal tests performed at 120 °C yielded different results than the lower temperatures. At an annealing temperature of 120 °C, the end of an exothermic peak was observed at the beginning of the 5 min isothermal hold, suggesting that crystallinity was

able to develop at 120 °C. In addition, the cold crystallization peak observed upon heating had the smallest enthalpy value, 9.0 ± 0.3 J/g, of any of the studied annealing temperatures. This peak and the percent crystallinity of the samples are given in Figure 4.3 and Table 4.2, respectively.

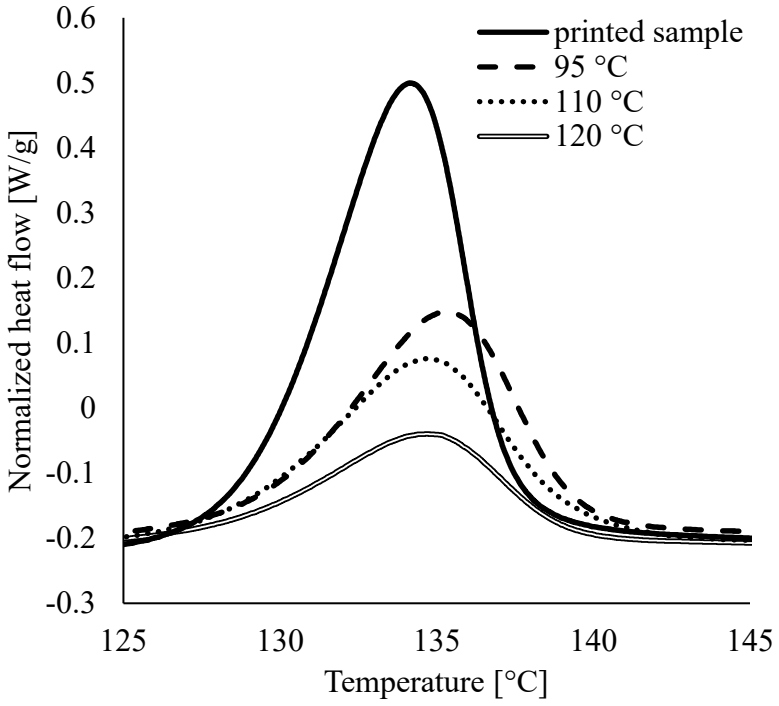

Figure 4.3: Cold crystallization peaks for as printed PPS compared to samples annealed at 95, 110, and 120 °C. Samples annealed at 85 and 90 °C behaved similarly to those annealed at 95 °C and samples annealed at 100 °C showed the same behavior as those annealed at 110 °C. Decreasing cold crystallization peaks indicated higher levels of crystallinity. Annealing at 120 °C showed crystallization occurring while lower temperatures only developed crystallinity during cooling from melt to the isothermal temperature at a rate of 85 °C/min (1.4 °C/s).

Table 4.2: Cold crystallization and melting peak and enthalpy values for PPS MEX parts as printed and after exposure to elevated annealing temperatures (T_a).

T_a [°C]	$T_{c,\ cold}$		T_m		Total crystallinity [%]	Crystallinity without cold crystallization [%]
	Peak [°C]	Enthalpy [J/g]	Peak [°C]	Enthalpy [J/g]		
As printed	134 ± 0.1	25.9 ± 0.8	280 ± 0.8	38.0 ± 0.6	47.6 ± 0.8	15.1 ± 1.2
85	136 ± 0.2	15.5 ± 0.8	280 ± 0.3	37.3 ± 0.9	46.7 ± 1.1	27.2 ± 0.8
90	136 ± 0.1	15.6 ± 0.7	280 ± 0.3	38.4 ± 0.4	48.1 ± 0.4	28.5 ± 0.5
95	135 ± 0.1	15.6 ± 0.3	280 ± 0.4	38.3 ± 0.4	48.0 ± 0.5	28.4 ± 0.4
100	135 ± 0.1	14.3 ± 0.7	280 ± 0.2	38.8 ± 0.2	48.7 ± 0.2	30.7 ± 0.7
110	135 ± 0.1	14.8 ± 0.6	280 ± 0.1	39.0 ± 0.2	48.9 ± 0.2	30.3 ± 0.6
120	135 ± 0.2	9.0 ± 0.3	281 ± 0.3	39.0 ± 0.1	49.0 ± 0.1	37.7 ± 0.4

4.3.2 Fast scanning calorimetry

The slow heating and cooling rates available to DSC prevented it from effectively studying the target annealing temperatures relevant to the MEX process and reorganization processes also affected its accuracy measuring crystallinity. The fast heating rates available with FSC were utilized to suppress reorganization phenomena, notably cold crystallization, that were observed in conventional DSC tests. Figure 4.4 shows the heating cycles performed on a PPS sample with heating rates from 50 to 5,000 °C/s and a constant cooling rate of 4 °C/s. It is worth noting that the slowest heating rate used in these experiments was 300 times faster than the heating rate used in the conventional DSC tests in order to suppress the reorganization phenomena observed in conventional DSC. The melting

temperatures observed for each heating rate are shown in Figure 4.5. The initial decrease in melting peak from 259 to 254 °C resulted from the suppression of reorganization processes at 300 °C/s. The subsequent increase in melting peak to 262 °C starting at 2000 °C/s was assumed to result from thermal lag [105, 116, 171]. The melting temperature of PPS measured with FSC (254 °C) was lower than the melting temperature measured with conventional DSC (279 °C) likely because of the suppression of reorganization behavior using FSC. In addition, the use of a faster cooling rate in FSC may have resulted in the formation of thinner crystals, which could also result in a decreased melting temperature compared to conventional DSC [117].

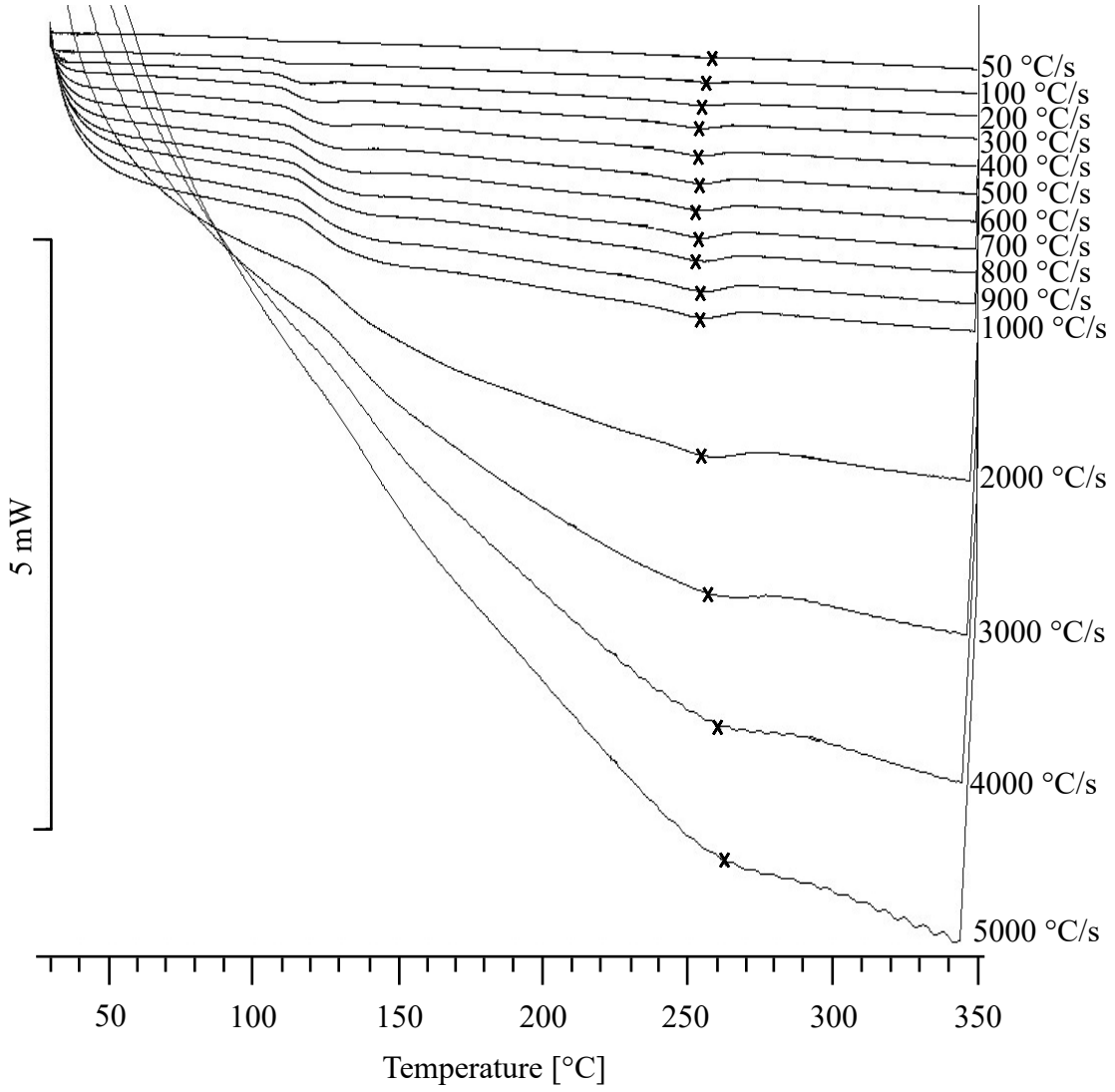

Figure 4.4: Heating rates ranging from 50 to 5,000 °C/s were used on FSC to determine the critical heating rate to prevent reorganization processes. The initial decrease in melting peak (X) resulted from the suppression of reorganization processes at 300 °C/s. The subsequent increase in melting peak starting at 2000 °C/s was the result of thermal lag.

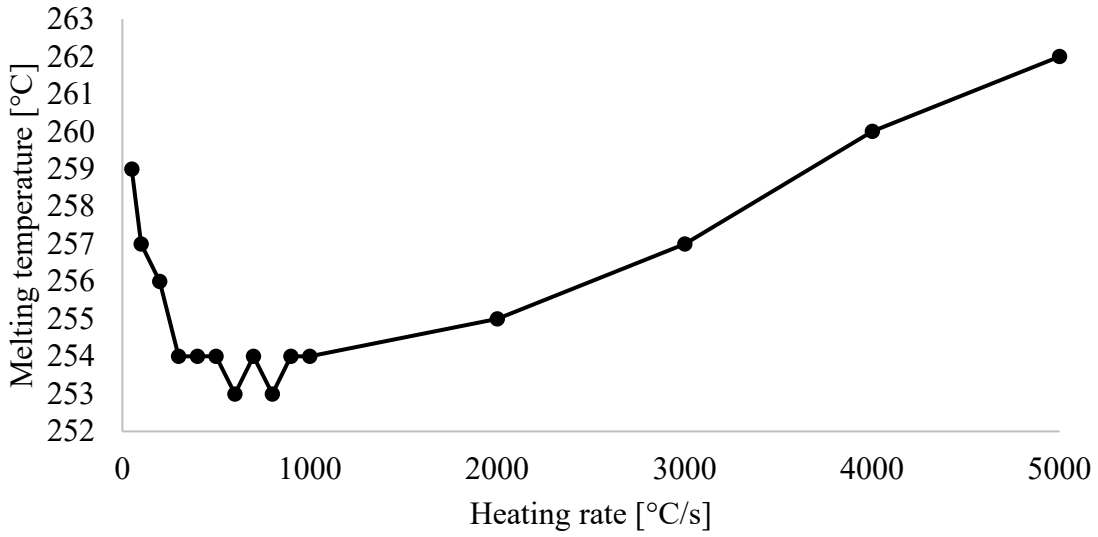

Figure 4.5: Peak melting temperatures of PPS measured using FSC at different heating rates. The initial decrease in melting peak resulted from the suppression of reorganization processes at 300 °C/s while the subsequent increase starting at 2000 °C/s was the result of thermal lag.

Following the determination of the critical heating rate, the critical cooling rate required to suppress crystallization was determined by running a series of heating and cooling cycles at the critical heating rate, 300 °C/s, and a range of cooling rates, β. The explored cooling rates ranged from 1 to 100 °C/s, and the heating cycles following the cooling at those rates are given in Figure 4.6**.** The critical cooling rate to prevent crystallization in the sample was determined to be 40 °C/s. Figure 6 shows that increasing the cooling rate decreased the melting enthalpy, indicating a decrease in percent crystallinity. Heat flow data for cooling rates of 1-10, 20, and 30 °C/s showed measurable melting peaks while data for higher cooling rates, 40 – 100 °C/s, did not show any melting peaks. The critical cooling rate of 40 °C/s was over 28 times faster than the fastest cooling rate attained by conventional DSC (85 °C/min, 1.4 °C/s) when investigating annealing.

These results supported the earlier conclusion that crystallization was occurring during cooling in conventional DSC annealing studies.

In addition, the glass transition was affected by the cooling rate. The amorphous portion of the sample that contributed to the glass transition decreased with decreasing cooling rates as the sample was able to crystallize more at slower rates. The decrease in amorphous portion contributing to the glass transition resulted in a broad and small glass transition step. As the cooling rate was increased, the sample became increasingly amorphous, resulting in a larger step as more of the sample was able to relax during this transition. Moreover, crystals formed in the semicrystalline samples hinder the mobility of the amorphous chains in between crystalline regions, resulting in increased glass transition temperature. Therefore, as crystallinity decreased, the onset of glass transition decreased as the amorphous phase had more mobility with less crystallinity present. Increased enthalpic relaxation, shown as the peak before the endset of glass transition, was seen at the highest cooling rates as polymer chains were immobilized in less enthalpic favorable positions at these rates.

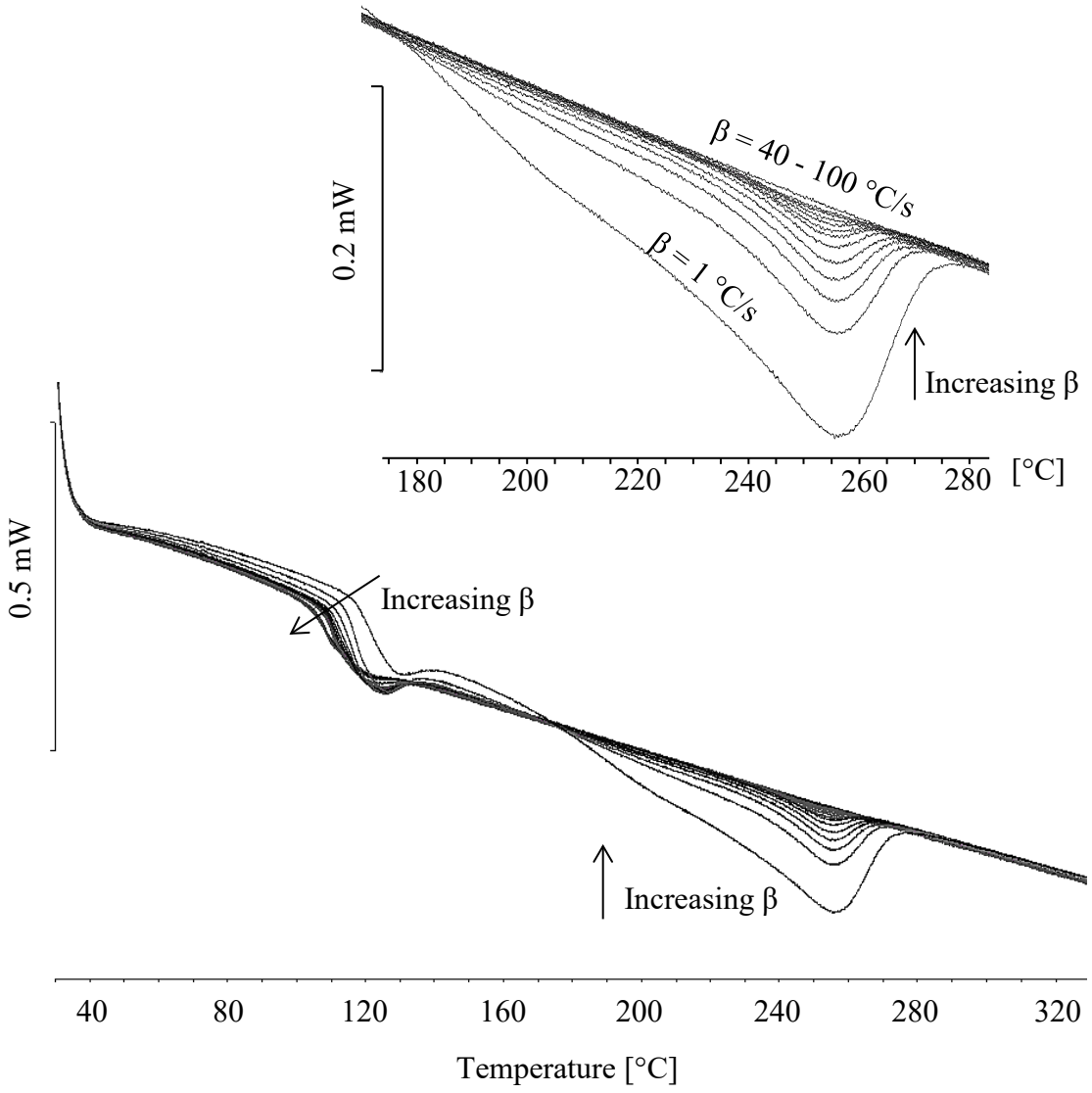

Figure 4.6: Heating curves performed after cooling from melt at a range of cooling rates showed decreasing melting enthalpies with increasing cooling rate. Less crystallinity formed in the material during cooling resulted in a decrease in glass transition temperature onset and a decrease in melting enthalpy. At cooling rates between 40 and 100 °C/s, no crystallinity was formed in the material and no melting peak was observed.

With the critical heating rate to prevent reorganization and the critical cooling rate to prevent crystallization determined, FSC was used to examine crystallization behavior at possible elevated build chamber temperatures for MEX. In these tests, samples were heated above melt at the critical heating rate and cooled to the annealing temperature at the critical cooling rate and held isothermally for 5 min. The sample was again heated above melt at the critical heating rate and these curves are shown in Figure 4.7. Figure 4.7 shows that only annealing at 120 °C resulted in a semicrystalline sample, which agreed with annealing studies performed on conventional DSC. The melting peak was located at 247 °C, which is lower than the melting temperature recorded during the critical heating rate measurements due to the lower temperature at which the material crystallized.

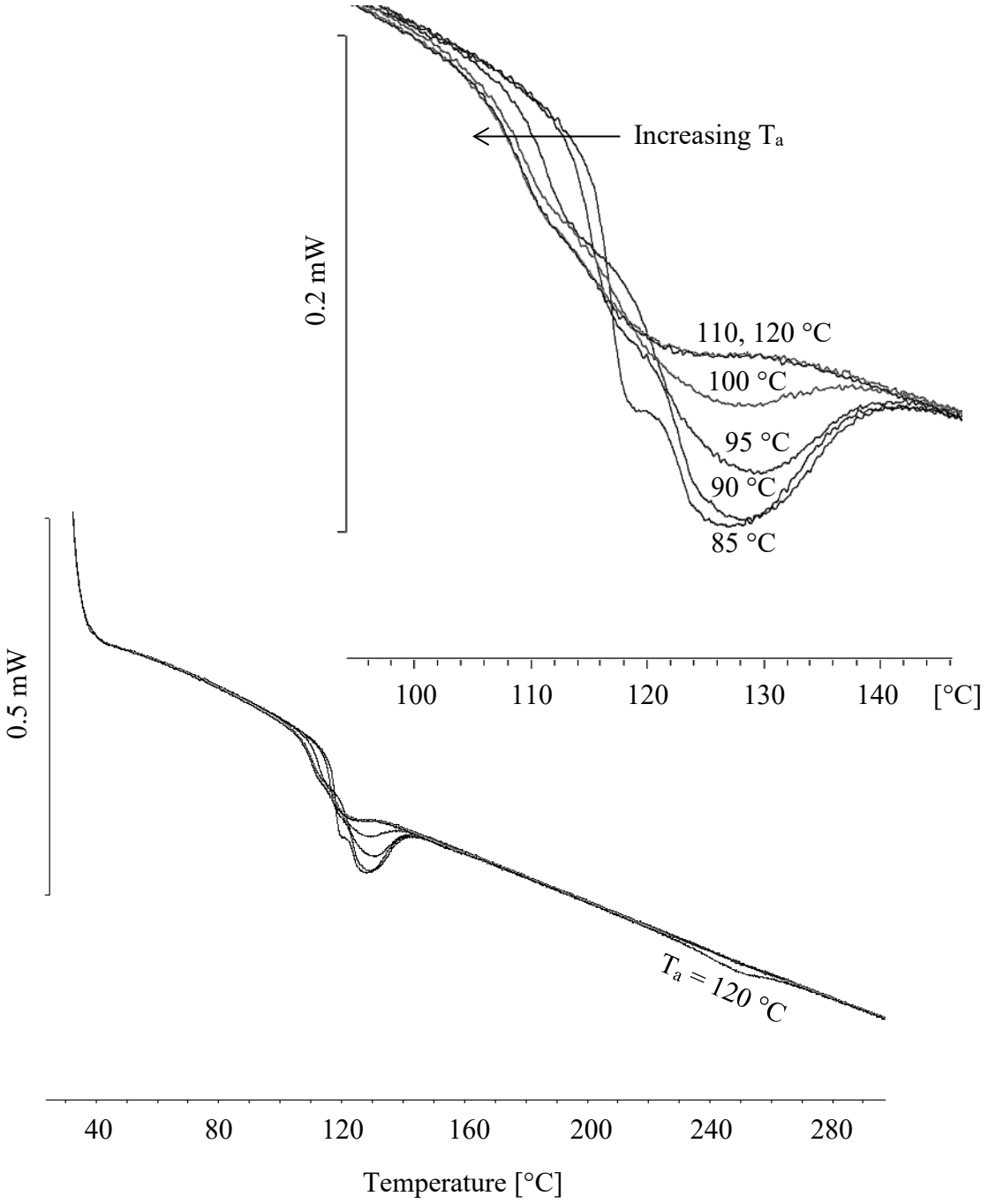

Figure 4.7: Heating curves performed at the critical heating rate (300 °C/s) after annealing at possible build chamber temperatures, 85, 90, 95, 100, 110, and 120 °C. The only sample showing a melting peak was annealed at 120 °C. The inability of the other samples to crystallize support the presence of a RAF. The peak around 128 °C that increased with decreasing annealing temperature shown in the inset image resulted from the relaxation of increasing RAF as the sample was annealed at lower temperatures.

The effect of low annealing temperatures on the glass transition temperature is shown in the inset image in Figure 4.7. Samples annealed at 120, 110, and 100 °C had similar onset glass transition temperatures around 103.8 ± 0.3°C. The onset glass transition temperature then increased with decreasing annealing temperature, having values of 108, 112, and 114 °C for isothermal temperatures of 95, 90, and 85 °C, respectively. Previous work has shown an increase in onset glass transition for PPS annealed at low temperatures due to increases in the rigid amorphous fraction (RAF) [172-176]. RAF is a fraction of the amorphous phase that couples the crystalline regions to amorphous regions. It does not become mobile at the glass transition temperature and instead relaxes between glass transition and melt. The RAF has molecular mobility ranging from the mobile amorphous phase to crystalline phase. Crystals formed at lower crystallization temperatures are less perfect and the interface regularity decreases with decreasing crystallization temperature. The increased interface irregularity leads to an increase in RAF with decreasing crystallization temperature as the RAF exists at the boundary between crystals and the mobile amorphous phase. The increase in the portion of RAF results in an increase in glass transition onset as fewer amorphous chains are mobile to participate in glass transition because the existence of RAF hinders molecular motion at the glass transition [172-174]. This work was consistent with the results seen in Figure 4.7.

In addition to changes in onset temperature, the enthalpic relaxation observed during glass transition was affected by the annealing temperature. The highest annealing temperatures of 120 and 110 °C exhibited the smallest amount of enthalpic relaxation. As the annealing temperature decreased, a peak near 128 °C associated with enthalpic relaxation became more pronounced. Enthalpic relaxation has been shown to increase with

decreasing annealing temperatures as stresses between mobile amorphous chains and the RAF increase [172-175].

The determined critical cooling rate of 40 °C/s for PPS was slower than measured and simulated cooling rates for MEX reported in previous studies [40, 49, 77, 84, 104]. Samples cooled at the higher rates associated with MEX would result in completely amorphous samples in FSC. Conventional DSC analysis on as printed parts showed very little crystallinity (15%), which agreed with FSC results indicating a critical cooling rate slower than MEX cooling rates. The crystallinity that was shown in MEX parts could be the result of underestimation of the contribution of the cold crystallization to the melting enthalpy [106] or the result of thermal cycling experienced during the MEX build process [15, 79, 102, 103]. Thermal cycling above 120 °C, where crystallinity has been shown to develop using conventional DSC and FSC, could increase the crystallinity of the amorphous material.

Thermal cycling studies were also performed using FSC to mimic the cycles of heating and cooling that occur during MEX fabrication as successive roads and layers are additively deposited causing the reheating of previously deposited material. Heating and cooling was performed at a rate of 740 °C/s from 100 ° C to four chosen temperatures: 240, 200, 160 and 120 °C. Runs with 10, 20, 30, 40 and 50 cycles at each temperature were performed according to the temperature profile shown in Figure 4.1. After the thermal cycling, the sample was heated above the melt temperature at the critical heating rate, 300 °C/s. These curves are shown in Figure 4.8.

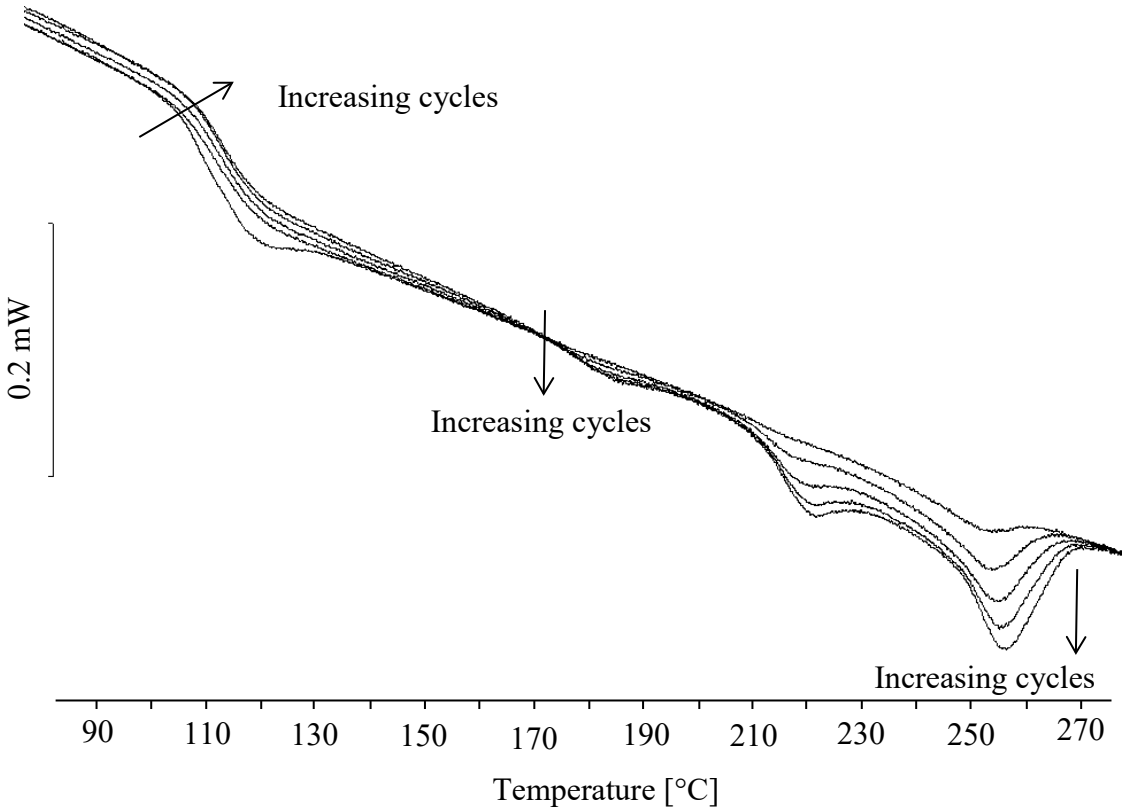

Figure 4.8: Heating curves performed at the critical heating rate (300 °C/s) after thermal cycling for 10, 20, 30, 40, and 50 cycles of four temperatures, 240, 200, 160, and 120 °C. The heating curves showed increases in onset of glass transition, increases in the RAF transition at 184 °C, increases in reorganization processes around 220 °C, and increases in melt enthalpy at 256 °C with increasing number of heating and cooling cycles.

The heating curves in Figure 4.8 showed increases in the enthalpy of melting at 256 °C with increasing heating and cooling cycles. The percent crystallinity for each curve was calculated and plotted with respect to cycles in Figure 4.9. The percent crystallinity increased to 11% after 50 heating and cooling cycles at each temperature. In addition, increasing the number of cycles increased the transition at 184 °C and the endothermic peak at 220 °C and also increased the onset of glass transition. The transition at 184 °C was attributed to the relaxation of the RAF and the peak at 220 °C was due to reorganization phenomena that resulted from the relaxation of the RAF. RAF increased with increasing heating and cooling cycles because with the development of more crystalline regions, a higher content of RAF was needed to couple the crystalline regions to the mobile amorphous regions [172-176]. In addition, the increase in RAF inhibited molecular motion at glass transition and decreased the number of mobile chains available to participate, resulting in an increased glass transition onset.

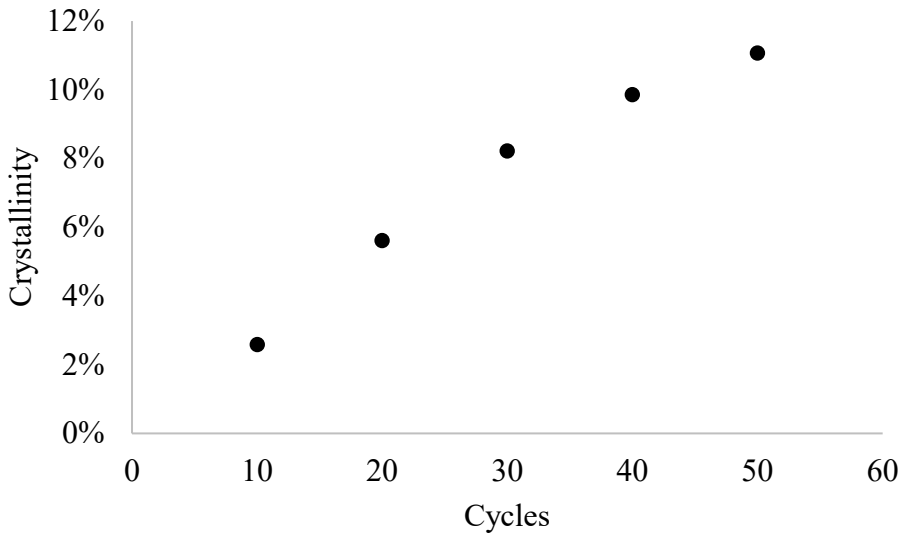

Figure 4.9: Thermal cycling performed to mimic the temperature exposure of MEX resulted in increasing percent crystallinity of PPS with increasing heating and cooling cycles.

The effect of cyclic heating at the four studied temperatures was examined in the 50-cycle test by performing a heating run after cycling to each of the temperatures. The resulting heating curves are shown in Figure 4.10 along with the temperature profile that indicates where each heating curve was performed.

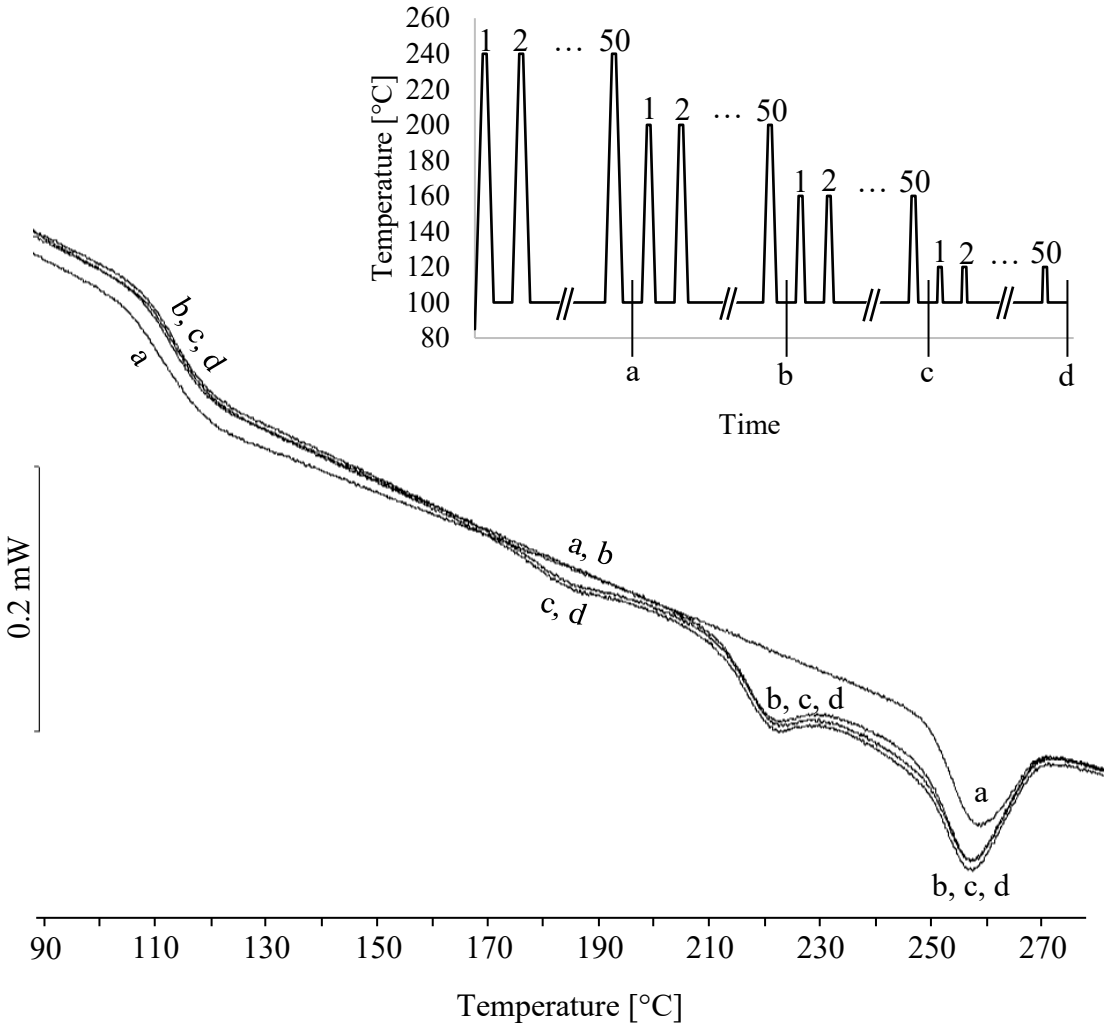

Figure 4.10: Heating performed at various points, shown by the inset temperature profile, during the 50 heating and cooling cycle run. The melting peak at 257 °C measured after 50 cycles to 240 °C (a) indicated the development of crystallinity. The increase in the melting peak after cycling to 200 °C (b) indicated increases in crystallinity. The development of a peak at 220 °C was attributed to reorganization with relaxation of increased RAF which also increased the onset of glass transition after cycling to 200 °C (b). Cycling to 160 °C (c) resulted in the formation of RAF in less energetically favorable configurations as shown by the development of a separate glass transition at 185 °C. Cycling to 120 °C (d) did not result in the development of any new transitions.

Cycling to 240 °C developed crystallinity in the sample and resulted in a melting peak at 256 °C in Figure 4.10. Subsequent cycling to 200 °C increased the crystallinity in the sample that led to a larger melting peak at 256 °C. In addition, the onset of glass transition increased as a result of increasing RAF. The new peak observed at 210 °C was attributed to reorganization behavior resulting from the increased RAF content. With the increased crystalline regions, RAF increased in order to couple the crystalline regions to mobile amorphous regions. The increase in RAF led to an increased onset of glass transition, as fewer amorphous chains were mobile at that temperature to participate in the transition. Fast heating rates available with FSC allowed reorganization phenomena to be suppressed resulting in the direct measurement of a glass transition of RAF observed at 210 °C. Cycling to lower temperatures at 160 and 120 °C resulted in RAF regions with increased strains due to the lower mobility present at lower crystallization temperatures. The lower mobility available resulted in the formation of RAF in less energetically favorable configurations [177, 178]. The increased strains present in RAF regions developed at lower crystallization temperatures resulted in a separate glass transition for RAF at 185 °C connected to enthalpy recovery following structural relaxation of the RAF. The observation of a separate transition associated with RAF relaxation has been observed in previous work using modulated DSC [177-179]. However, a separate glass transition for RAF cannot typically be directly identified using conventional DSC because of the reorganization phenomena, such as recrystallization, that occur with the relaxation of RAF [180]. While reorganization behavior at 220 °C still followed the RAF glass transition at 185 °C, fast heating rates available with FSC allowed reorganization phenomena to be

separated resulting in the direct measurement of a glass transition of RAF observed at 185 °C.

FSC was used to examine the crystallization behavior of PPS at heating and cooling rates associated with MEX. Observed crystallization behavior demonstrated the influence of RAF in PPS on its behavior during annealing at potential build chamber temperatures for MEX and during thermal cycling inherent to the MEX fabrication process. Crystallization did not occur at temperatures below 120 °C, which was 30 °C above the midpoint of glass transition at 90 °C. The RAF prevented the formation of crystallinity at these temperatures resulting in increased stability. This added stability could be advantageous when selecting an elevated build chamber temperature for MEX. Previous work has shown the importance of temperature history on bond formation and the resulting mechanical properties of MEX parts [15-17, 77, 79, 81, 83, 84, 86, 101, 102]. A higher build chamber temperature would result in increased time above glass transition temperature leading to increased bonding and increased mechanical properties. In addition, higher build chamber temperatures would reduce cooling rates in MEX, which would reduce thermal gradients responsible for residual stresses and strains. Reduction in residual stresses could lead to reduced warpage in the parts. However, reduced cooling rates could also decrease dimensional stability in the part through increased drooping and sagging in the deposited roads. The effect of the temperature history imposed on the part during MEX fabrication was demonstrated through thermal cycling studies that showed the reheating of the part during successive deposition of new roads and layers could increase the crystallinity and RAF of the part. Increases in crystallinity are typically associated with increases in mechanical properties [181]. However, in MEX parts, this increase in

crystallinity could also lead to increased part warpage through shrinkage. Increased mechanical properties accompanied by losses in dimensional accuracy are two competing factors to be considered when assessing the thermal environment experienced by semicrystalline polymers in MEX. In addition, because of the role of the RAF in coupling crystalline regions to amorphous regions in semicrystalline polymers, increases in RAF have also been shown to affect the mechanical properties of semicrystalline materials [177].

4.3.3 FSC of PPS compared to work with PP

Experimental comparison of PPS to PP has shown that PP exhibits significantly more warpage than PPS. Simulated thermal gradients and cooling rates experienced in PPS were shown to be larger than those experienced by PP in the process simulation models developed in CHAPTER 3. The process simulation models determined that CTE was the material property that had the largest influence on the warpage behavior modeled by the process simulation models; however, the simulations did not explicitly capture crystallization behavior of the two materials.

Printed PP parts exhibited a percent crystallinity of 39%, which was larger than the 15 % shown by PPS samples. PP has been extensively studied using FSC to investigate its crystal morphology, which has been shown to be highly dependent on cooling rate and annealing conditions [108, 109, 144, 151, 153-157, 182]. The critical cooling rate for PP determined from these studies was 1000 °C/s. This cooling rate is faster than the cooling rate of 392 °C/s simulated by Watanabe et al. [40]. Because the cooling rates experienced

during MEX fabrication of PP are not sufficiently large to prevent crystallization, PP parts crystallize during fabrication, leading to increased shrinkage and warping. By understanding the cooling rates in the MEX process and comparing them to the critical cooling rates that prevent crystallization, the warpage behavior of semicrystalline MEX materials can be predicted.

4.4 Conclusions

In this chapter, FSC has been used to understand the effect of thermal exposures on semicrystalline polymers used in MEX. The shift of MEX from a prototyping method to a manufacturing strategy has necessitated understanding how to control the resulting part performance. FSC was shown in this work to capture aspects of the MEX process such as the high cooling rates and the successive heating and cooling cycles that occur during the additive build process. FSC was able to mimic this cyclic heating and cooling and show the evolution of crystallinity in an MEX part based on thermal variables from process simulation models. The use of fast heating rates in FSC also showed the presence of a RAF in PPS. This structure is likely present in printed parts because of the repeated exposure to low crystallization temperatures. The use of FSC provided a method to investigate the effects of high heating and cooling rates and thermal cycling experienced during MEX on crystallization behavior.

CHAPTER 5. INTERLAYER BONDING IMPROVEMENT OF MEX PARTS USING THE TAGUCHI METHOD[§]

5.1 Background

5.1.1 Material extrusion process parameters

MEX is a complex process with many settings, or process parameters, that affect the quality of the produced part. MEX process parameters can be grouped into two categories: deposition strategy and thermal management variables. Deposition strategy variables dictate how the part is additively realized. Figure 5.1 and Figure 5.2 show several deposition strategy variables. Additionally, commonly used MEX deposition strategy variables are described below [20].

- Deposition or build orientation is the way in which the MEX part is oriented on the build platform with respect to the X, Y, and Z-axes. Three common deposition orientations are shown in Figure 5.1.
- Layer thickness is the thickness of the layer or slices deposited by the MEX nozzle. For MEX, the layer thickness typically varies between 0.1 mm and 0.4 mm [1].
- Air gap, or wire width compensation, is the gap between adjacent rasters on the same layer. The air gap is shown in Figure 5.2.

§ Parts of this chapter have been taken/adapted from author's publication – [21] E. R. Fitzharris, I. Watt, D. W. Rosen, and M. L. Shofner, "Interlayer bonding improvement of material extrusion parts with polyphenylene sulfide using the Taguchi method," *Additive Manufacturing,* vol. 24, pp. 287-297, 12/01/2018. https://doi.org/10.1016/j.addma.2018.10.003

- Raster angle is the angle between the raster pattern and the X-axis of the MEX part. The raster angle is shown in Figure 5.2 and can vary from 0° to 90°.
- Cross-hatching refers to the rotation of the raster angle by 90° after each layer, which creates a crosshatch effect. This setting is turned either on or off.
- Raster width is the width of the deposited material in each raster that make up a layer. The values of raster width used in MEX depend on the size of the MEX nozzle.
- Infill pattern is the tool path used when depositing the rasters. There are a variety of infill patterns available. In Figure 5.2, the infill pattern used is a rectilinear infill pattern.
- Infill density is the percent of the total part layer occupied by the raster fill pattern.
- Contours, or perimeters, are roads deposited around the outside of the MEX part shown in Figure 5.2.
- Contour width is the width of the deposited material in a contour.
- Contour depth refers to the number of contours used in the MEX part or the distance they occupy from the outside of the part. This is shown in Figure 5.2.
- Deposition speed is the velocity of the print head during road deposition.
- Deposition style, or build style, refers to the way in which a part is filled. In general, deposition style can be characterized by the density of the infill pattern as follows:
    - "Solid" fills the interior of the MEX part completely.
    - "Sparse" leaves gaps between the rasters to minimize the material used and the build time. It typically utilizes unidirectional rasters.

- "Sparse double dense" reduces the material used and build time similarly to the "Sparse" deposition style, but uses a crosshatch raster pattern instead of unidirectional rasters.

- Support style refers to how the support structures are deposited to prevent overhanging areas of the MEX part from collapsing during fabrication. Not all MEX machines are designed to fabricate support structures. Some common types of support styles are described below:
  - "Basic" refers to the standard support style in which all MEX part features are supported with small support raster curves.
  - "Sparse" is a support style in which support material volume is reduced.
  - The "Surround" support style builds support structures around small areas of the MEX part.
  - The "Break-away" support style is similar to sparse, but the raster patterns are specifically designed in discrete boxes so it is easier to remove than the other support styles.

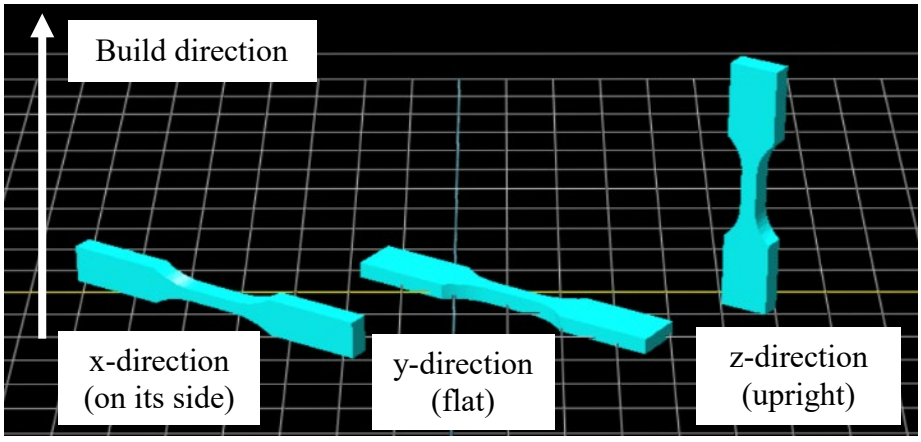

Figure 5.1: Deposition orientation of a D638 Type V dogbone

a)

b)

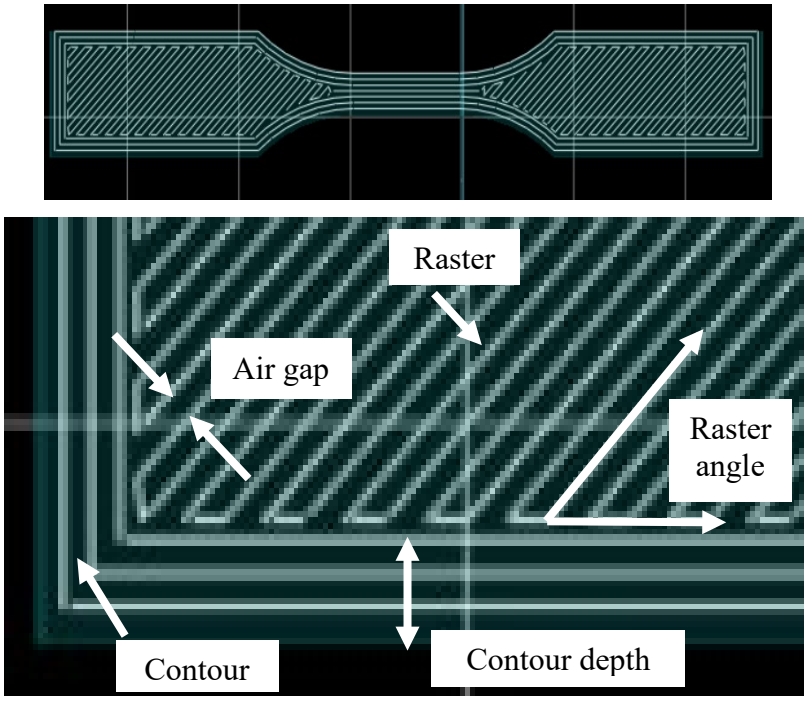

Figure 5.2: Tool path for a D638 Type V dogbone fabricated with in the y-direction build orientation with a raster and contour width of 0.5 mm. The dogbone had 3 contours, a rectilinear infill pattern with 100% infill density, a raster angle of 45°, and an air gap of -15% (a). The tool path is magnified to show various MEX process parameters (b).

While deposition strategy variables describe how the MEX part is additively realized, thermal management variables control the thermal exposure experienced by the part during fabrication. The three main MEX thermal management variables are: print temperature, build platform temperature, and build chamber temperature. The print temperature is the temperature at which the material is extruded through the MEX nozzle. The build platform temperature is the temperature of the surface on which MEX parts are fabricated and the build chamber temperature is the temperature of the enclosed space that houses the part during fabrication. While fabricating parts in an elevated temperature build chamber could improve MEX part quality by decreasing thermal gradients and increasing time above T_g to increase bonding between layers, only high end systems have the ability to control the chamber temperature [9].

5.1.2 Robust design through design of experiments techniques

As described in section 2.2, MEX process parameters influence the orientation of roads and layers and also affect the thermally driven bonding process. Therefore, the proper selection of MEX process parameters is essential to the success of the MEX process and the resulting part quality [20]. Various design of experiment (DOE) methods or robust design methods have been used to examine the effect of different design parameters on overall product quality and reliability [183]. Robust design is a design insensitive to variations that has been developed to improve product quality and reliability [183]. A DOE method commonly used in engineering fields is the Taguchi method [184]. The Taguchi method provides a systematic and efficient approach for design optimization that offers

several advantages such as the simplification of the experimental plan [185-187]. This simplification leads to a reduction in both time and cost of production of parts and greatly reduces the product development cycle time in product design and production [186-188].

The Taguchi method can be divided into three main stages: system design, parameter design, and tolerance design [189-191]. The general procedure is shown in Figure 5.3 [188]. In system design, the system configuration is developed and suitable working levels are determined for the design factors of interest. In the parameter design stage, the design factors or parameters are optimized in order to meet the quality requirements of the product. In this optimization process, the factors that reduce the product's sensitivity to noise are identified so that the robustness can be enhanced. The steps included in the parameter design stage are: selecting the proper orthogonal array according to the number of control factors or parameters, performing the experiments based on the orthogonal array, identifying the optimum condition for the control factors, analyzing the data, and performing confirmation runs with the optimum levels of the control factors. The parameter design phase examines two types of factors: control factors and noise factors. Control factors are parameters that are set and held at specific values or levels, while noise factors are parameters that cannot be easily controlled, such as environmental conditions [183, 184, 188, 192, 193].

During the parameter design stage, experiments are performed based on the selected orthogonal array. An orthogonal array is a subset of control parameter combinations that can be statistically analyzed to determine which control parameters are significant to the design output. The orthogonal array defines the experimental space to be tested. For each experiment, control factors are held at specific levels while the noise

factors cannot be controlled. For each control factor experiment, a response is obtained and the mean and variance of the responses are then calculated with the goal of reducing the influence of the noise parameters. The measured mean and variance of the responses are used to calculated the performance characteristic used by the Taguchi method known as Signal-to-Noise (S/N) ratio. Taguchi proposed different S/N measures depending on the design objective. The three S/N ratio characteristic types are known as "nominal is best", "smaller is better", and "larger is better". When a specific target value for the response is known, the "nominal is best" S/N ratio is used. When the design objective is to minimize or maximize the response, the "smaller is better" or "larger is better" S/N ratios are used, respectively. The equations for the three characteristic type S/N ratios are given in Table 5.1 as Equation 5.1, 5.2, and 5.3, where η is the S/N ratio, n is the total number of experiments, $\hat{y}$ is the response target value, and y_i is the response for the ith experiment [183, 193].

Table 5.1: Signal-to-Noise (S/N) ratio equations used in the Taguchi method

Characteristic type	S/N ratio equation	
Nominal is best	$\eta = -10log\left[\frac{1}{n}\sum_{i=1}^{n}(y_i - \hat{y})^2\right]$	(5.1)
Smaller is better	$\eta = -10log\left[\frac{1}{n}\sum_{i=1}^{n}y_i^2\right]$	(5.2)
Larger is better	$\eta = -10log\left[\frac{1}{n}\sum_{i=1}^{n}\frac{1}{y_i^2}\right]$	(5.3)

Analysis of variance (ANOVA) is also used in the parameter design phase to determine which control parameters are statistically significant to the design output. With this analysis, the optimum control parameter combination can be determined for a specific process. Finally, a confirmation run is conducted to validate the optimal control parameters obtained from the ANOVA [183, 186-188, 192]. In the last stage of the Taguchi method, the tolerance design stage, the allowable deviations in the parameter values are specified so that the optimum levels of the control factors obtained in the second stage can be fine-tuned [183, 184, 188, 192, 193].

System design	Determination of suitable working levels of the design parameters
Parameter design	1. Select appropriate orthogonal array 2. Conduct experiments 3. Identify optimum condition (S/N ratio analysis) 4. Analyze data (ANOVA) 5. Perform confrimation runs
Tolerance design	Tighten the tolerance of the significant parameters determined in the parameter design.

Figure 5.3: The Taguchi method is made up of a 3-phase iterative approach. Based on the results of the parameter design phase, the tolerances of the significant parameters may be tightened. Following the modification of the parameter levels, the parameter design phase can be performed again until the desired robustness is achieved.

Several studies that utilized the Taguchi method to examine the effect of MEX process parameters on part quality have been conducted with ABS and PLA. These studies have optimized MEX part surface roughness, mechanical properties, and dimensional accuracy by examining a variety of process parameters [13, 14, 26, 185, 186, 194-199].

Optimization studies on dimensional accuracy and surface roughness commonly examined the effects of layer thickness, deposition orientation, raster angle, deposition speed, air gap, and contours [14, 185, 195-199]. For dimensional accuracy, layer thickness, deposition orientation, raster angle, contour width, and air gap were significant parameters. Wang et al. and Sood et al. both concluded that a flat build orientation yielded the best dimensional accuracy [14, 197]. In addition, Chang and Huang showed that increasing contour width increased dimensional accuracy [198]. However, other studies had conflicting findings on how layer thickness, raster angle, and air gap affected the dimensional accuracy [195, 196, 199]. Concerning surface roughness, a small layer thickness was determined to be the most significant parameter that resulted in a low surface roughness [14, 185].

5.1.3 Use of the Taguchi method with MEX

Several authors have investigated the effects of MEX process parameters on the mechanical properties of MEX parts using the Taguchi method [13, 14, 26, 194]. These studies showed that significant process parameters that affected the mechanical properties of MEX parts included deposition orientation, layer thickness, infill density, and deposition temperature. Flat deposition orientations that were tested in line with the deposited rasters

yielded the best mechanical properties. In addition, larger layer thickness, higher infill density, and higher deposition temperature resulted in improved mechanical properties. Torres et al. also investigated the effect of heat-treatments on mechanical properties in MEX parts. Long heat-treatment times were associated with an increase in strength, but a loss in ductility, especially in low infill density parts. Therefore, short heat-treatment times were suggested to improve strength while maintaining ductility [26].

Various post-processing methods have been used with different AM processes in order to improve material property anisotropy and part quality of the produced parts. The use of heat-treatments, or annealing, in polymers has been shown to reduce residual stresses and strains, increase dimensional stability, reduce defects, and improve physical properties [200]. Increases in bonding between amorphous polymer interfaces are driven by wetting and inter-diffusion mechanisms [18, 19]. In addition, previous studies have shown that amorphous polymers have the ability to crack heal and strengthen interface adhesion at temperatures below their glass transition temperatures [201-203]. In semicrystalline polymers, studies have shown that heat-treatments can change the crystal structure, the degree of crystallinity, and the orientation of both crystalline and amorphous regions [200, 204-208]. Increases in crystallinity have been shown to improve various material properties such as elastic modulus, yield strength, and thermal stability [181]. In addition, interfacial bonding can be enhanced by mechanisms such as co-crystallization. Previous work has shown that co-crystallization can reinforce polymer interfaces if some inter-diffusion of chains occurs before crystallization [209].

Some studies have been conducted that show the benefits of post processing heat treatments on MEX parts. Previous studies on ABS parts fabricated with MEX showed that

toughness increased during post-processing heat-treatments above glass transition temperature according to the time to the one-fourth power, consistent with polymer diffusion mechanisms [81]. Torres et al. demonstrated that heat-treating PLA MEX parts increased the tensile strength but resulted in a loss in ductility [26]. Wang et al. also showed the benefits of heat-treating MEX parts produced with Polywax, a PE wax material [210]. MEX parts made with Polywax showed an increase in tensile strength, increase in compressive strength, and decrease in porosity when heat-treated. Yang et al. showed that various thermal processing conditions, including heat treatments, affected the crystallinity of PEEK MEX parts [211]. Yang et al. showed that heat-treating semicrystalline polymers increased their crystallinity, which could improve material properties. In addition, they suggested that the improved material properties that resulted from heat-treating the parts may also be a result of reduced residual stresses and reduced internal defects instead of just a result of increased crystallinity.

Even though heat-treating parts produced with MEX could improve their material properties, these methods have not been extensively investigated. With MEX, post-processing heat-treatments could improve bonding between roads and layers, improve overall material properties, and decrease the porosity present in produced parts [26, 210, 211]. PPS MEX parts were heat-treated to examine the phenomena specific to semicrystalline polymers. Increases in crystallinity resulting from post-processing heat-treatments of PPS could increase resulting MEX part properties.

5.1.4 Key research objectives

The objective of this chapter was to use the Taguchi method to improve the interlayer bonding of MEX parts fabricated with PPS. The control parameters of interest included material dependent parameters such as print temperature, heat-treatment time, and heat-treatment temperature. These parameters were selected due to their influence on the thermally driven bonding process in MEX and it was hypothesized that control of the thermal history in the MEX process could reduce disparities between bulk and MEX parts. ASTM D638 Type V dogbones were fabricated and heat-treated at various conditions. They were then mechanically characterized in order to determine the effects these control parameters have on interlayer bonding. The effect of the heat-treatments on MEX part crystallinity were investigated. These studies showed that post-processing heat-treatments improved interlayer bonding in PPS parts printed using MEX. Similar studies were also performed with an amorphous polymer, NORYL, as described in APPENDIX C.

5.2 Materials and Methods

5.2.1 Materials

PPS in monofilament with a diameter of 1.4 mm was used as the printing feedstock. The properties of this material are given in Table 5.2. Glass transition temperature and melting temperature were measured using DSC described in section 4.2.1 and the ultimate tensile strength (UTS) and Young's modulus were measured by mechanically testing a

compression molded film described in section 5.2.4. Before printing, the filament was dried in a vacuum oven at 100 °C for 3 hrs.

Table 5.2: Material properties of bulk PPS

Material Property	**Units**	**Value**
Density [170]	g/cm^3	1.35
T_g (midpoint)	°C	90
T_M	°C	282
UTS	MPa	76.6
Young's modulus	MPa	3180

5.2.2 Taguchi method

In order to examine the effects of the selected control parameters on the interlayer bonding of PPS MEX parts, proper levels must be selected for each parameter in the system design phase of the Taguchi method. Table 5.3 shows the three levels selected for each of the three control parameters: print temperature, heat-treatment time, and heat-treatment temperature. The print temperature range was determined by examining the viscosity of PPS, shown in Equation 3.5 in section 3.2.2. It was hypothesized that the viscosity of ABS at MEX conditions could be used as a benchmark to determine the printing temperature of other materials used in MEX. The shear rate of the HYREL System 30 was estimated based on Newtonian flow through a pipe according to Equation 5.4,

$$\dot{\gamma} = \frac{4Q}{\pi r^3} \tag{5.4}$$

where $\dot{\gamma}$ is the shear rate, Q is the volumetric flow rate, and r is the radius of the MEX nozzle. The shear rate was determined to be 400 s^{-1}. At the HYREL System 30 shear rate and at the known printing temperature of ABS, ABS exhibited a viscosity of 500 Pa-s. This viscosity value and the HYREL System 30 shear rate were used in Equation 3.5 to calculate the theoretical print temperature of PPS of 288 °C. Based on this calculation, the print temperature levels selected for Taguchi analysis were 290 °C, 300 °C and 310 °C because higher print temperatures have been associated with increases in bonding and mechanical properties in MEX parts as described in section 2.2 [17].

Heat-treatment times were defined as the amount of time the printed dogbone was exposed to the heat-treatment temperature. Isothermal crystallization studies were performed using DSC using a TA Instruments Discovery DSC to determine heat-treatment time and temperature levels to be investigated. The sample was heated past melt and held isothermally for 5 min to ensure full melting. It was then equilibrated at the desired temperature and held isothermally for 5 min. The sample was then equilibrated at room temperature and heated past the melting temperature at 10 °C/min to measure the percent crystallinity developed in the sample. The percent crystallinity was calculated by integrating the melting peak obtained from DSC and using the peak area in Equation 4.1.

Isothermal crystallization studies showed that PPS developed 48.1 ± 1.1% crystallinity in less than 5 minutes for temperatures from 120 °C to 220 °C. The selected heat-treatment times were chosen to allow significant crystallization to occur at all times. The selected heat-treatment times were also based on polymer chain diffusion studies that showed the time scales necessary for polymer chains to diffuse across interfaces according

to the reputation model [201]. These studies showed increases in interfacial bonding at times from 2 min up to 4 days. The selected heat-treatment temperatures were chosen at temperatures at which PPS would experience cold crystallization. Room temperature was also chosen as a heat-treatment temperature to act as a control experiment. The effect of time on samples heat-treated at room temperature was not expected to be significant.

Table 5.3: Control parameters and levels for Taguchi analysis of PPS

Control Parameter	Level		
	1	2	3
Print temperature (A)	290 °C	300 °C	310 °C
Heat-treatment time (B)	10 min	100 min	24 hrs.
Heat-treatment temperature (C)	Room temperature	140 °C	180 °C

Based on the number of control parameters of interest and their corresponding levels, an L_9 orthogonal array was used for the process optimization. The L_9 array is a fractional-factorial experiments matrix with nine trials developed by Taguchi. A fractional-factorial experiments matrix uses a portion of the total possible combinations of the control parameters to estimate the main control parameter effects [212]. The L_9 array given in Table 5.4 details the levels of each control parameter that were used in the performed experiments.

Table 5.4: Taguchi experimental plan using an L_9 orthogonal array

Experiment number	**Parameter/level**		
	A	B	C
1	1	1	1
2	1	2	2
3	1	3	3
4	2	1	2
5	2	2	3
6	2	3	1
7	3	1	3
8	3	2	1
9	3	3	2

Following the experimental plan given in Table 5.4, three ASTM D638 Type V dogbones were fabricated for each experiment number, resulting in 27 total dogbones.

The S/N ratio measures the sensitivity of the property being investigated to uncontrollable external factors. In this study, the objective was to maximize the Young's modulus and UTS, therefore the "larger is better" S/N ratio equation was used given in Equation 5.3 [183, 193]. The optimum control parameter condition for each design output was determined by maximizing the average S/N ratio for each parameter. Additional experiments were performed to confirm that the optimum control parameter condition for each design output resulted in a maximized value.

Following the S/N ratio analysis, ANOVA was performed for each design output to determine which control parameter(s) were significant to each design output. The data were analyzed in MATLAB using the "anovan" function for multi-way ANOVA. ANOVA is based on the sum of the squares (SS), degrees of freedom (DOF), variance of each control

parameter (Var_i), and variance of the noise factors or experimental error (Var_e). The F-ratio, or variance ratio, was calculated using Equation 5.5.

$$F = Var_i/Var_e \tag{5.5}$$

When the ratio becomes large enough, the variances were accepted to be unequal at some confidence level. When the F ratio for a control parameter was large enough, that parameter was considered statistically significant to the design output. This indicated that the variation seen in the data was due to the changing control parameter and not due to the error variation from noise factors.

The percent contribution of each control parameter (P_i) and the error (P_e) was calculated according to Equation 5.6.

$$P = SS_i/SS_T \tag{5.6}$$

where SS_i is the sum of squares for a control parameter or the error and SS_T is the total sum of squares. The percent contribution due to error provided an estimate of the efficacy of the process optimization. If the contribution due to error was less than 15%, the control parameters were under precise control and no important parameters were excluded from the analysis. Conversely, if the contribution from error was greater than 50%, this indicated that important factors were overlooked or the control parameters were not adequately controlled.

5.2.3 MEX dogbone fabrication

The MEX AM machine used in this study was the HYREL System 30 from HYREL International described in section 3.2.4 [91]. The HYREL System 30 was used to fabricate ASTM D638 Type V dogbones using the PPS monofilament. An extrusion multiplier of 1.5 was used to accommodate the non-standard filament diameter of 1.4 mm. The dogbones were fabricated at a print speed of 15 mm/s with a layer thickness of 0.2 mm, which were standard settings for the printer hardware, and a 0.5 mm diameter nozzle was used. They were fabricated in the upright z direction in order to characterize the interlayer bonding strength, which has been shown to be the weakest interface in MEX parts. They were constructed using a 90° raster angle with an infill density of 100%. The dogbones had a rectilinear infill with no contours. Contours were not used so that road-to-road bonding could be observed on the outside of the part. Additionally, eliminating contours in the printed parts allowed changes in the interfaces with changing process parameters to be studied more directly. The print temperature for the dogbones was chosen based on the orthogonal array given in Table 5.4. Three dogbones were fabricated for each experiment number given in the orthogonal array.

The heat-treatment protocol was started 24 hrs. after the dogbones were fabricated. For the elevated temperature heat-treatments, the dogbones were placed inside a preheated furnace at the specified heat-treatment temperature for the given heat-treatment time according to the Taguchi experimental plan. Upon completion, the samples were removed from the furnace and allowed to cool to room temperature for 30 minutes before mechanical testing. Room temperature heat-treated samples were left at room temperature for their

heat-treatment time plus an additional 30 min before testing to provide consistency between the elevated temperature heat-treated samples.

5.2.4 Mechanical testing of MEX dogbones

Tensile testing was performed on an Instron® 5566 static tensile testing frame using a 1 kN load cell with a rate of elongation of 2 mm/min. The Young's modulus was calculated from the initial slope of the stress vs. strain curves generated from this testing. The UTS was calculated using the maximum load experienced during testing and the cross sectional area of the gage area.

5.2.5 Compression molding and mechanical testing of PPS films

PPS films were compression molded using a Carver® auto series (model no. 4389) bench top press with heated platens. The PPS MEX monofilament was cut into small pellets and used as the feedstock material. The platens were heated to 300 °C and the PPS pellets were placed on glass reinforced Teflon mold release sheet. The platens were closed and allowed to come back to 300 °C for 2 min. 5 tons of pressure was then gradually applied to the platens and held for 5 min. After this time, the platens were cooled down to room temperature using the water-cooling on the Carver® press and the film was removed from the mold release sheets. ASTM D638 type V dogbones were cut from the center of the film using a die cutter. The films were tested using the same procedure outlined in section 5.2.4 for the printed MEX dogbones.

5.2.6 Imaging MEX dogbones

Three surfaces of the fabricated dogbones were characterized including the fracture surface, a non-failure cross section, and a side image in the grip area of the dogbone. The non-failure cross section was obtained by starting a crack in the sample at a layer interface using a razor blade. The sample was then broken at that layer interface by bending the sample. The samples heat-treated at elevated temperatures were brittle and cleanly broke at the desired interface. Samples that were heat-treated at room temperature were more ductile and were bent after placing the samples in the freezer for 24 hrs. to induce brittle behavior.

An Olympus BX51 microscope in reflectance mode was used with StreamEssentials software and an Olympus UC30 camera to take digital images of the non-failure cross section and the side image of the fabricated dogbones. Images of the fracture surface were taken using a Leica DVM6 A microscope. The custom z-stack feature was used to obtain in focus images of the irregular fracture surfaces.

5.2.7 Differential scanning calorimetry

After mechanical testing, DSC was performed on the PPS dogbones to determine the percent crystallinity of the parts using a TA Instruments Discovery DSC. The DSC procedure was based on ASTM E794 described fully in section 4.2.1. The percent crystallinity was calculated by integrating the melting peak obtained from DSC and using the peak area in Equation 4.1.

5.3 Results and Discussion

The ASTM D638 type V dogbones fabricated according to the orthogonal array given in Table 5.4 were mechanically characterized and their percent crystallinity was calculated. The average UTS, Young's modulus and percent crystallinity for each experiment are given in Table 5.5. Figure 5.4 and Figure 5.5 show the stress vs. strain curves for experiments representative of the overall stress vs. strain behavior of the tests.

Table 5.5: Average UTS, Young's modulus, and percent crystallinity for Taguchi Experiments with PPS MEX dogbones.

Experiment	UTS [MPa]	Young's modulus [MPa]	Percent Crystallinity
1	39.5 ± 4.1	1800 ± 157	26.0 ± 4.8 %
2	45.4 ± 1.1	1860 ± 153	46.1 ± 2.0 %
3	57.1 ± 3.8	2050 ± 144	47.1 ± 1.1 %
4	58.7 ± 4.3	2160 ± 36	48.1 ± 1.1 %
5	59.3 ± 4.2	2190 ± 89	47.0 ± 2.2 %
6	50.1 ± 0.3	1860 ± 29	25.7 ± 1.6 %
7	61.1 ± 3.3	2230 ± 54	48.0 ± 0.5 %
8	44.8 ± 2.8	1810 ± 47	20.3 ± 1.2 %
9	60.9 ± 2.5	2160 ± 32	47.0 ± 2.8 %

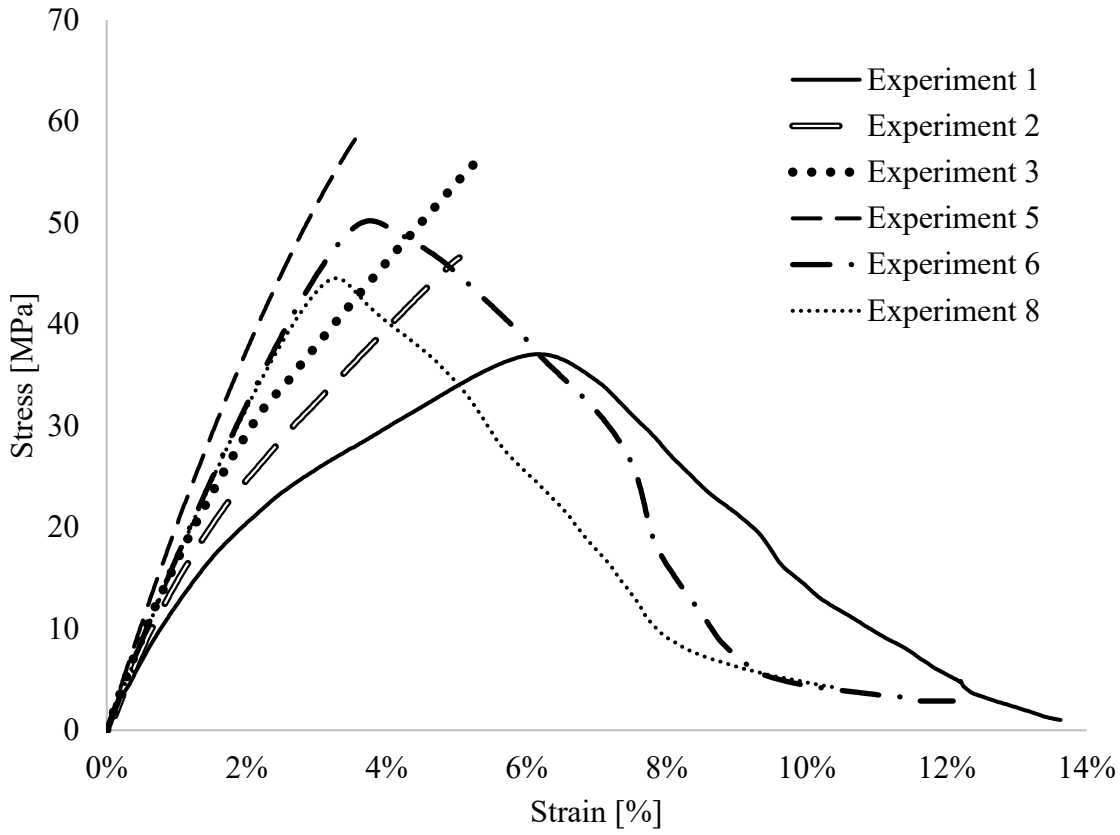

Figure 5.4: Stress vs strain behavior for PPS MEX dogbones for the Taguchi experiments. Experiments 4, 7, and 9 are excluded from this figure and instead shown in Figure 5.5 because they overlapped experiment 5.

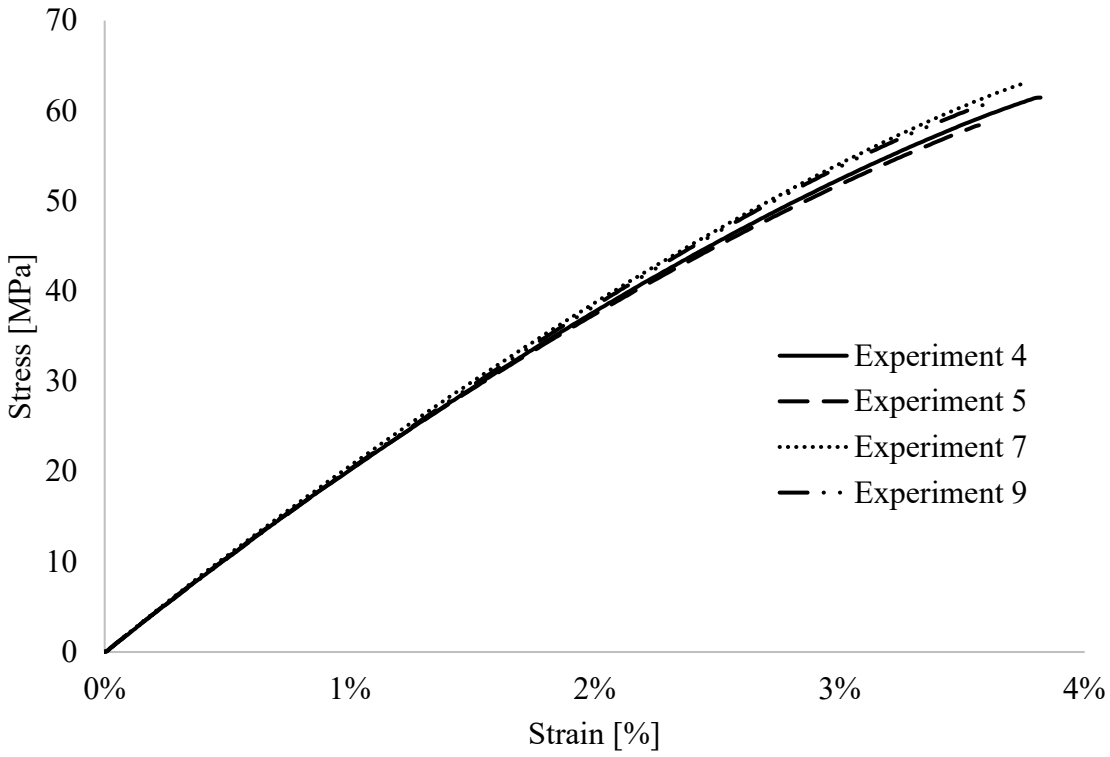

Figure 5.5: Stress vs. strain behavior for PPS dogbones for Taguchi experiments 4, 5, 7, and 9.

As shown in Figure 5.4, room temperature heat-treated samples (experiments 1, 6, and 8) yielded during mechanical testing, resulting in higher strain to failure values from 10% to 14%. Sample sets that were heat-treated at elevated temperatures exhibited more brittle behavior and had strain to failure values between 3% and 6%. Experiments 2 and 3, which were printed at the lowest print temperature of 290 °C, exhibited more ductility than other samples heat-treated at elevated temperatures and failed between 5% and 6% strain. The other experiments heat-treated at elevated temperatures, experiments 4, 5, 7 and 9, were the most brittle and failed around 3% strain. In Figure 5.4, experiments 4, 7, and 9

were not plotted as they overlapped experiment 5. These experiments were plotted separately in Figure 5.5 to show their similarity to experiment 5.

Compression molded films fabricated with the PPS MEX filament were mechanically tested and had a UTS of 76.6 ± 6.0 MPa and a Young's modulus of 3180 ± 32 MPa. The UTS values of the printed dogbones ranged from 52-80% of the PPS compression molded films and the Young's modulus values ranged from 57-70%. These values characterize the interlayer bonding strength of the MEX part because the samples were built in the vertical build direction. Testing MEX parts perpendicular to the layer has been shown to result in the lowest mechanical properties [1, 6, 10, 12-14]. The UTS values exhibited by room temperature heat-treated dogbones were consistent with decreased UTS values of MEX parts fabricated with ABS. The ABS parts fabricated in previous work with similar print settings used in this work exhibited a UTS of 50% of injection molded ABS UTS [10].

The percent crystallinity of the compression molded films, characterized using DSC, was 51.1 ± 1.1%. The percent crystallinity of room temperature heat-treated dogbones was 24.0 ± 4.0% and the percent crystallinity of elevated temperature heat-treated dogbones was 47.3 ± 1.9%. The high cooling rates experienced by the dogbones during MEX printing resulted in low levels of crystallinity as discussed in CHAPTER 4. The high cooling rates resulted in room temperature heat-treated dogbones that were less crystalline than the PPS compression molded films. In addition, the larger variation in percent crystallinity of room temperature samples compared to heat-treated dogbones was likely due to print temperature variation, with the sample printed at the highest temperature having the lowest crystallinity.

5.3.1 S/N ratio analysis for PPS MEX dogbones

The S/N ratio for UTS, Young's modulus, and percent crystallinity were calculated using the experimental data in Equation 5.3. The average S/N ratio for each control parameter level was also calculated. These results are shown graphically in Figure 5.6.

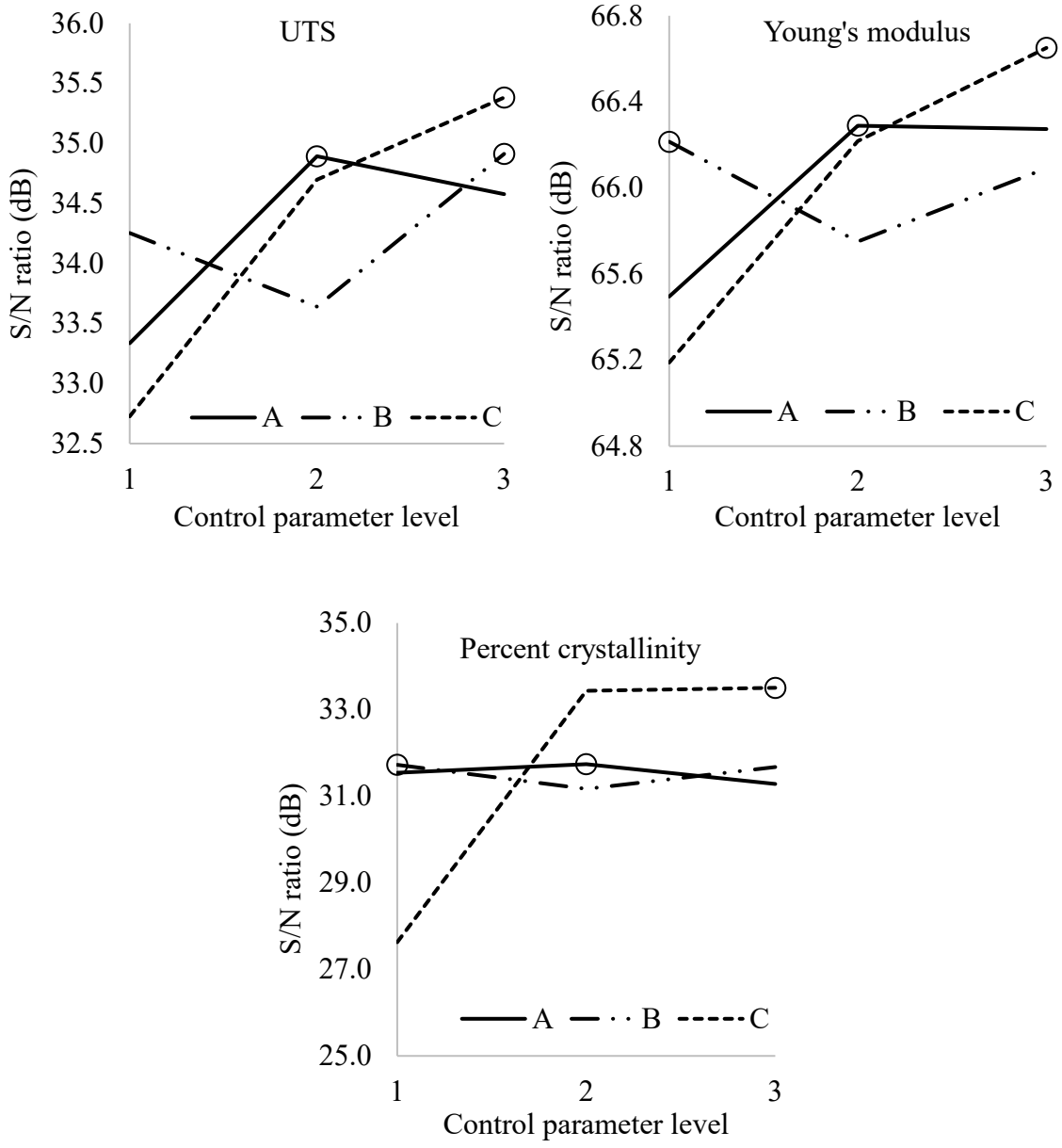

Figure 5.6: Parameter level effect plots for UTS, Young's modulus, and crystallinity. The optimum parameter condition for UTS, Young's modulus and crystallinity were determined by maximizing the S/N ratio for each control parameter, indicated by ○ on the plot. The optimum print temperature (A) and heat-treatment temperature (C) for UTS, Young's modulus, and crystallinity were 300 °C and 180 °C, respectively. The optimum heat-treatment time (B) for UTS was 24 hrs. while the optimum heat-treatment time for Young's modulus and crystallinity was 10 min.

The optimum control parameter condition for each design output was determined by maximizing the average S/N ratio for each parameter. The parameter levels with the maximum average S/N ratio for UTS were a 300 °C print temperature, 24-hour heat-treatment time, and 180 °C heat-treatment temperature (A2 B3 C3). For print temperature (A), the two highest print temperatures yielded higher S/N ratios for UTS. Higher print temperature could improve road-to-road and layer-to-layer bonding. However, a print temperature that was too high could result in sagging in the roads and layers, which could be detrimental to UTS. While levels 2 and 3 for print temperature resulted in higher S/N ratios than level 1, the S/N ratio for level 3 was smaller than the ratio for level 2 indicating that the highest print temperature used adversely affected UTS. The longest heat-treatment time (B) of 24 hrs. resulted in the largest UTS. However, the range of S/N ratios for print temperature and heat-treatment time were much smaller than the range seen with heat-treatment temperature. The average S/N ratio for samples exposed to elevated heat-treatment temperatures were much higher than the average S/N ratio of samples treated at room temperature. This indicated that heat-treatment temperature had a larger influence on UTS than the other two control parameters.

The optimum parameter condition for Young's modulus was a 300 °C print temperature, 10-minute heat-treatment time, and 180 °C heat-treatment temperature (A2 B1 C3). The middle print temperature yielded the highest average S/N ratio, similar to what was seen with UTS. However, the shortest heat-treatment time resulted in the highest average S/N ratio instead of the longest heat-treatment time seen with UTS. This result was consistent with previous studies that showed decreases in Young's modulus with longer heat-treatment times [26]. Similarly to what was observed with UTS, the range of S/N

ratios for print temperature and heat-treatment time were much smaller than the range seen with heat-treatment temperature, with heat-treatments at elevated temperatures resulting in the highest average S/N ratios.

The optimum parameter condition for percent crystallinity was the same as the optimum parameter condition for Young's modulus, a 300 °C print temperature, 10-minute heat-treatment time, and 180 °C heat-treatment temperature (A2 B1 C3). The range of the average S/N ratio for print temperature and heat-treatment time were small, and the average S/N ratios were similar for all levels. In comparison, the range associated with heat-treatment temperature was large. In addition, the average S/N ratios for both elevated heat-treatment temperatures were similar. This resulted from the similar levels of crystallinity that were achieved at both of the selected heat-treatment temperatures.

5.3.2 ANOVA of PPS MEX dogbones

Following the S/N ratio analysis that was used to analyze the effect of control parameter levels, ANOVA was performed for each design output to determine which control parameter(s) were significant to each design output. The ANOVA tables for UTS, Young's modulus, and percent crystallinity are given in Table 5.6, Table 5.7, and Table 5.8, respectively. The percent contribution of each of the control parameters to each design output is shown visually in Pareto plots in Figure 5.7. The significance of the control parameters was evaluated with 99% confidence.

Table 5.6: ANOVA table for the UTS PPS MEX dogbones.

Parameter	SS	DOF	Var	F-ratio	% contribution	Significant
A	390.6	2	195.3	14.15	19%	Yes
B	234.8	2	117.4	8.50	12%	Yes
C	1137.1	2	568.6	41.19	56%	Yes
Error	276.1	20	13.8		13%	
Total	2038.6	26				

Table 5.7: ANOVA table for the Young's modulus of PPS MEX dogbones.

Parameter	SS	DOF	Var	F-ratio	% contribution	Significant
A	163492.8	2	81746.4	5.9	16%	Yes
B	54071.3	2	27035.7	1.95	5%	No
C	527307	2	263685	19.03	52%	Yes
Error	277157.8	20	13857.9		27%	
Total	1022091.9	26				

Table 5.8: ANOVA table for the percent crystallinity of PPS MEX dogbones.

Parameter	SS	DOF	Var	F-ratio	% contribution	Significant
A	7.49	2	3.75	0.51	0.2%	No
B	24.84	2	12.42	1.71	0.8%	No
C	3086.32	2	1543.16	212.14	94.6%	Yes
Error	145.49	20	7.27		4.5%	
Total	3264.14	26				

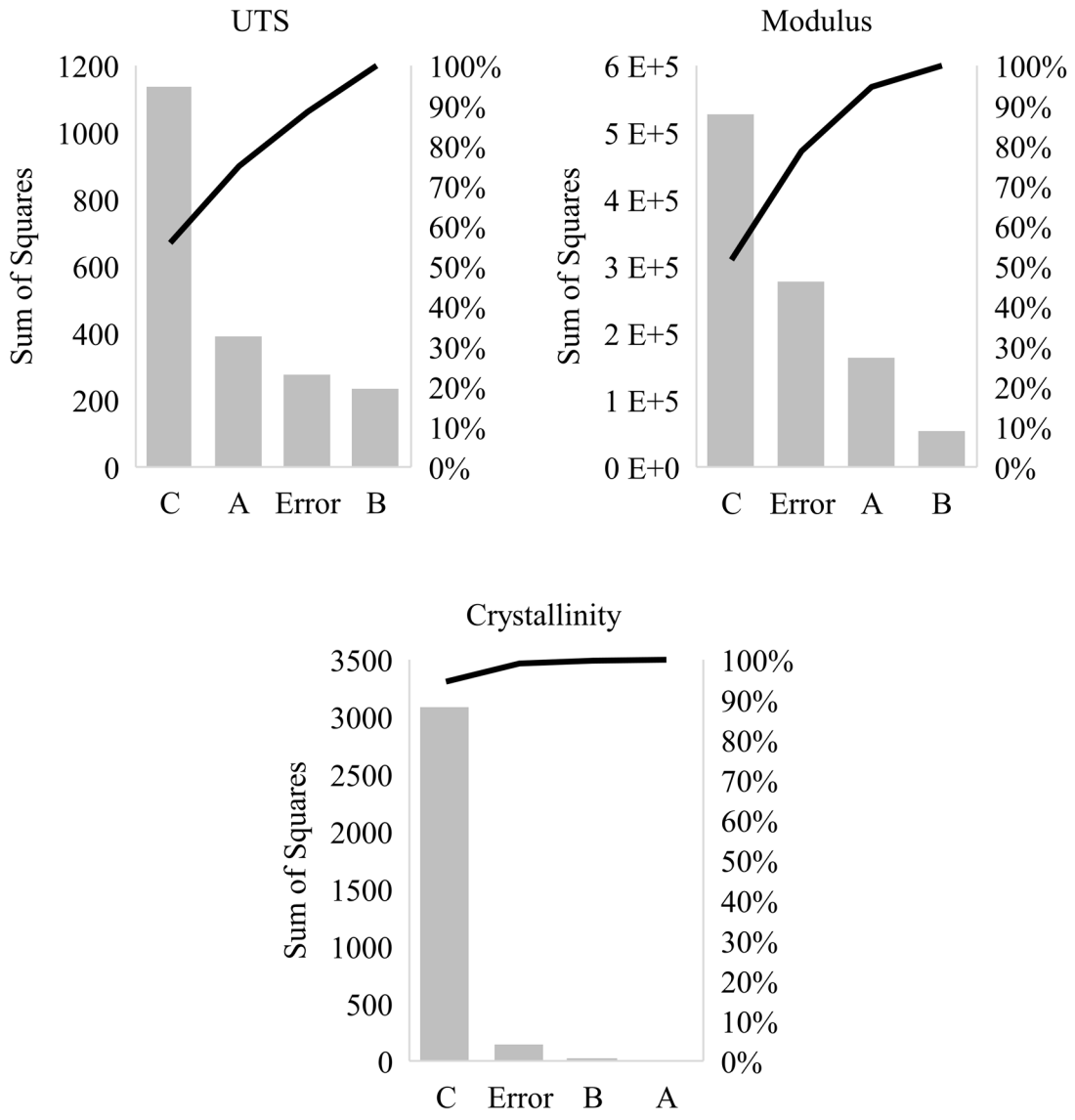

Figure 5.7: Pareto plots for UTS, Young's modulus, and crystallinity showed the percent contributions of each control parameter based on the SS analysis. Heat-treatment temperature (C) had the largest contribution to all design outputs and was statistically significant in all outputs. In addition to heat-treatment temperature, both print temperature (A) and heat-treatment time (B) were significant to UTS. Print temperature was also significant to Young's modulus, while only heat-treatment temperature was significant to percent crystallinity.

For UTS, all three control parameters were determined to be significant parameters that affected UTS with a 99% confidence level. Heat-treatment temperature (C) had the highest percent contribution, followed by print temperature (A) and heat-treatment time (B). The percent contribution of error was below 15%, which indicated that the control parameters were under precise control and no major parameters that affected UTS were excluded from the analysis. When examining Young's modulus, print temperature and heat-treatment temperature were significant parameters that affected Young's modulus. The contribution of error was larger in this analysis compared to the UTS analysis, but its contribution of 27.1% was still small enough to conclude that control parameters significant to Young's modulus were controlled. Lastly, only heat-treatment temperature was determined to have a significant effect on the percent crystallinity. The percent contribution from heat-treatment temperature accounted for 94.6% of the total, with only 1% coming from the other two control parameters. This result was in agreement with PPS isothermal crystallization studies that suggested the chosen time scales were long enough to allow significant crystallization to occur. While room temperature samples showed larger variation in percent crystallinity likely due to differences in print temperature, the effect of heat-treatment temperature on crystallinity was large enough to outweigh its contribution. The contribution from error of 4.5% was well below 15%, which indicated that the control parameters were under precise control and no major parameters were left uncontrolled.

The results of the ANOVA with respect to UTS, Young's modulus, and percent crystallinity indicated that heat-treatment temperature was a control parameter that affected many properties of MEX parts. Heat-treatment time was not significant to Young's

modulus or percent crystallinity and made a smaller percent contribution when it was significant to UTS. The small percent contribution of heat-treatment time was the result of the heat-treatment times investigated that were all at time scales that allowed significant crystallization to occur.

However, other phenomena besides crystallization contributed to improvements in UTS and Young's modulus at higher heat-treatment temperatures. The average S/N ratios for the elevated heat-treatment temperatures (levels 2 and 3) for crystallinity shown in Figure 5.6 were similar. The similar values showed that similar levels of crystallinity were achieved at both elevated heat-treatment temperatures. However, larger differences in the average S/N ratios between levels 2 and 3 of the heat-treatment temperatures were seen in the UTS and Young's modulus analysis. The larger differences between levels 2 and 3 implied that the highest heat-treatment temperature could result in further improvements in the MEX parts when testing perpendicular to the layer. Improvements that could result in increased mechanical properties at the highest heat-treatment temperature were decreased internal defects, improvements in layer interfacial bonding, improvements in road-to-road bonding, or further reduced internal stresses or strains.

5.3.3 Optical microscopy of PPS MEX dogbone interfaces

In order to investigate these factors, optical microscopy images were taken of the samples. The side, failure cross section, and non-failure cross section of the samples were characterized. In the side images, the testing direction is perpendicular to the road direction while the testing direction is out of the page for the failure and non-failure cross section

images. Figure 5.8 shows these images for samples from experiments 2, 5, and 8. These experiments were chosen for Figure 5.8 in order to examine the effects of print temperature and heat-treatment temperature while the heat-treatment time was kept constant at 100 min. Images obtained for all of the experiments are given in APPENDIX B in section B.1.

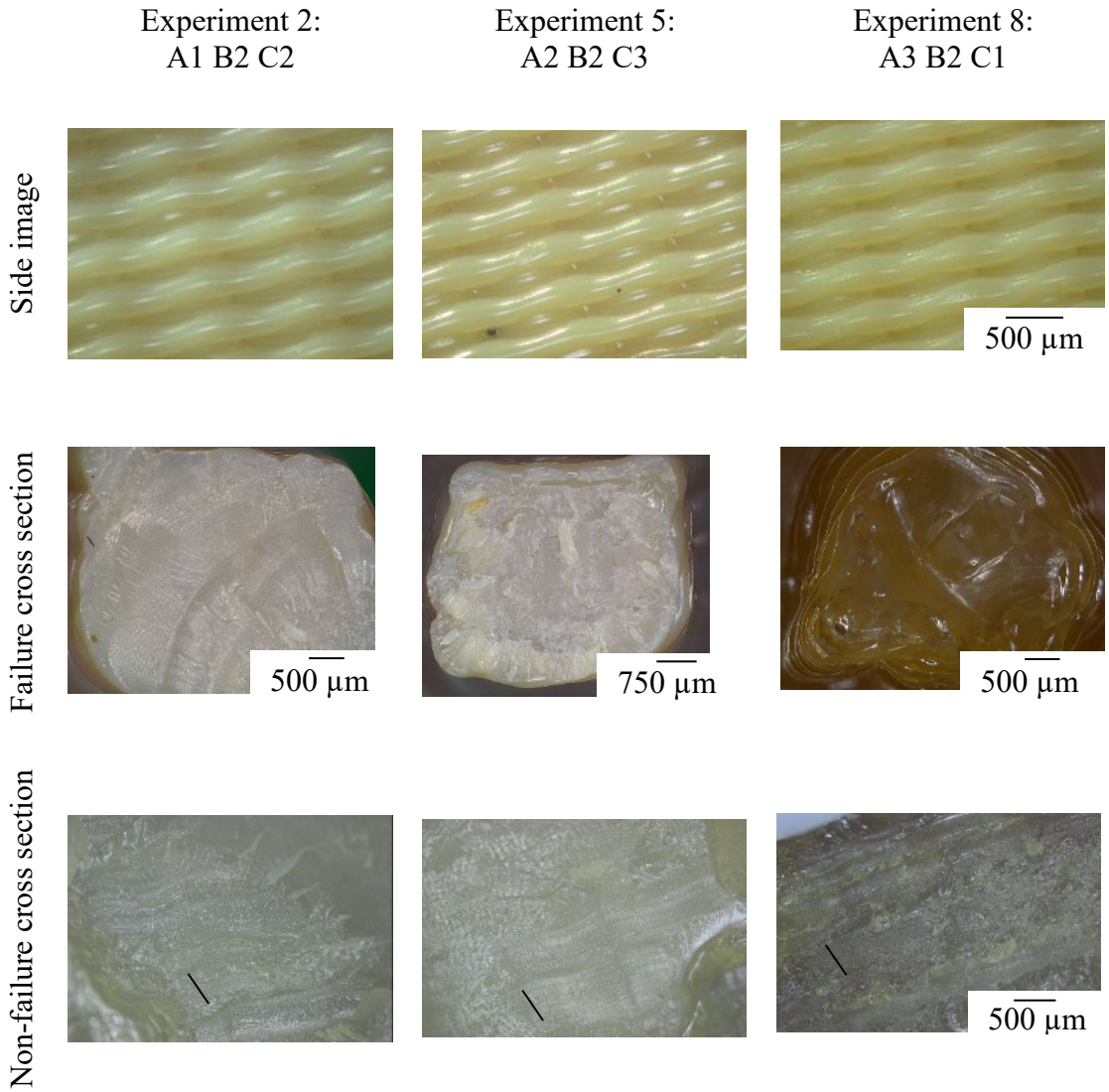

Figure 5.8: Side, failure cross section, and non-failure cross section images for Experiments 2, 5 and 8. In the side images, the testing direction is perpendicular to the road direction while the testing direction is out of the page for the failure and non-failure cross section images. Heat-treated samples were opaque while non heat-treated samples were translucent. Black bars on the non-fracture cross section images show the road width of 0.5 mm.

The side images for elevated heat-treated and room temperature heat-treated samples were similar. The individual roads with a 90° raster angle can be observed. The elevated heat-treated samples were opaque due to the crystallinity that developed during heat-treating at all heat-treatment times. The failure cross sections were similar for elevated heat-treated samples. No individual roads were visible in these cross sections at all heat-treatment times. Individual roads were visible in the non-failure cross sections for all heat-treatment temperatures and print temperatures. However, the appearance of roads, shown by the horizontal ridges visible on the non-failure cross section images, decreased with increasing heat-treatment temperature. The decrease in interfaces between roads with increasing heat-treatment temperature was an example of internal improvements in the MEX parts that resulted in improved mechanical properties. No differences in side, failure cross section, or non-failure cross section were observed with different heat-treatment times, which was consistent with the ANOVA results that suggested that heat-treatment time had the least effect on the studied properties and was only found to be statistically significant to UTS.

In addition, the appearance of roads decreased with increasing print temperature in both elevated temperature heat-treated and room temperature heat-treated samples. This is demonstrated more fully in Figure 5.9. Figure 5.9 shows non-failure cross sections of experiments heat-treated at the highest heat-treatment temperature, 180 °C. As the print temperature increased, the horizontal ridges that showed the interfaces between roads became less visible. The decrease in road interfaces was attributed to increased bonding between the roads, which resulted from the increased energy from the higher print temperature.

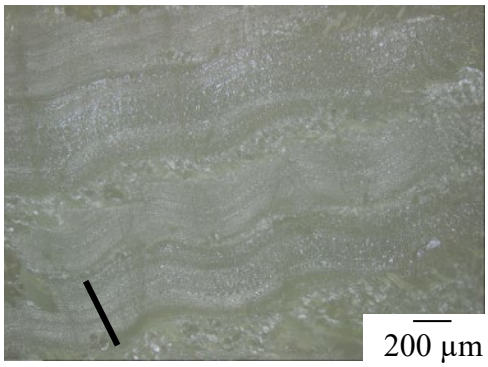

Experiment 3: A1 B3 C3

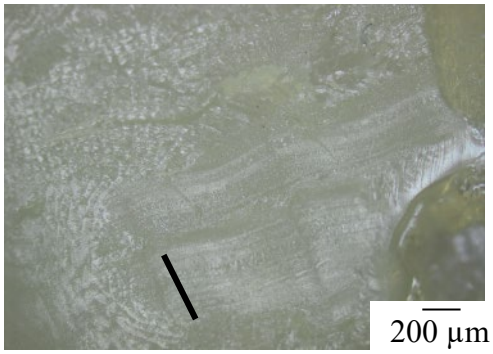

Experiment 5: A2 B2 C3

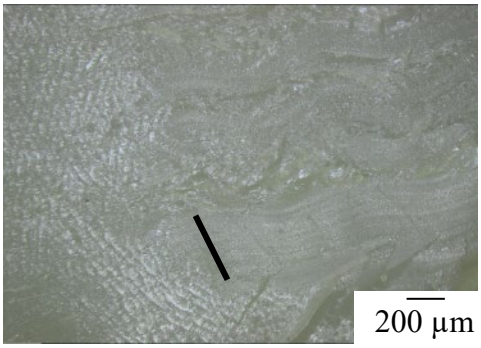

Experiment 7: A3 B1 C3

Figure 5.9: Non-failure cross sections showed that increasing the print temperature decreased the appearance of roads in elevated temperature heat-treated samples. Black bars on the images show the road width of 0.5 mm. In the images, the testing direction is out of the page.

5.3.4 Confirmation experiments for PPS MEX dogbones

Confirmation experiments were performed at the determined optimum parameter conditions of a 300 °C print temperature, 24-hour heat-treatment time, and 180 °C heat-treatment temperature (A2 B3 C3) for UTS and a 300 °C print temperature, 10-min heat-treatment time, and 180 °C heat-treatment temperature (A2 B1 C3) for Young's modulus and percent crystallinity based on the S/N analysis. The results of these experiments are

given in Table 5.9 and were compared to the maximum values obtained in the original Taguchi experiments. The confirmation experiment dogbones are shown compared to a room temperature heat-treated dogbone in Figure 5.10. The confirmation experiments did not warp during their heat-treatment, similar to the original Taguchi experiments. The shrinkage that occurred as a result of the heat-treatments was measured using printed PPS bars. The 30 mm x 6 mm x 3 mm bars were printed using the same settings used for the Taguchi dogbones. The volume reduction was calculated by measuring the dimensions of the bars before and after heat-treatment. The volume reduction exhibited by the optimum parameter combinations A2 B3 C3 and A2 B1 C3 were 2.83 ± 0.22% and 3.20 ± 0.50%, respectively.

Table 5.9: Results of confirmation experiments for PPS MEX dogbones.

		UTS [MPa]	Young's modulus [MPa]	Percent crystallinity
Confirmation Exp	A2 B3 C3	60.1 ± 2.6	2300 ± 123	48.4 ± 2.0 %
Confirmation Exp	A2 B1 C3	59.9 ± 1.6	2250 ± 39	48.3 ± 2.2 %
Exp 7	A3 B1 C3	61.1 ± 3.3	2230 ± 54	48.0 ± 0.5 %

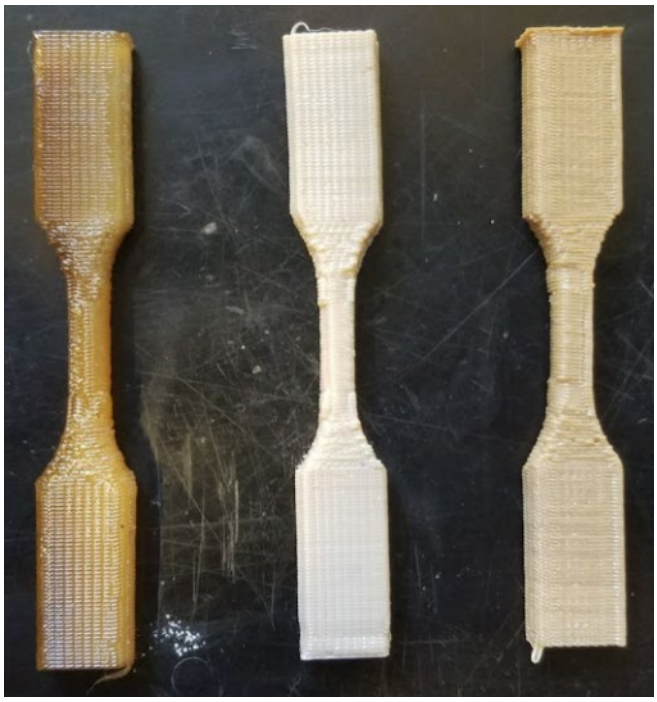

Figure 5.10: ASTM D638 type V dogbones fabricated according to experiment 1 (left), confirmation experiment A2 B1 C3 (middle) and confirmation experiment A2 B3 C3 (right).

In the original Taguchi experiments, the maximum UTS and Young's modulus were obtained from experiment 7, which had control parameter settings of A3 B1 C3. The results of the UTS confirmation experiment A2 B3 C3 were not statistically different from experiment 7. The similar results were consistent with the ANOVA for UTS that showed that print temperature (A) and heat-treatment time (B) were statistically significant control parameters but had lower percent contributions to affecting UTS.

The confirmation experiment A2 B1 C3 was used to maximize Young's modulus and percent crystallinity. The Young's modulus and percent crystallinity measured from confirmation experiment A2 B1 C3 were not statistically different from the results of the

original Taguchi experiment 7. The only control parameter difference between confirmation experiment A2 B1 C3 and experiment 7 was the print temperature (A). The ANOVA for Young's modulus showed that print temperature was a statistically significant control parameter, but it had a low percent contribution for the range of print temperatures examined in this study. The ANOVA for percent crystallinity showed that the only statistically significant control parameter to percent crystallinity was heat treatment temperature. The confirmation run and experiment 7 only differed in print temperature, so the statistically similar results agreed with the conclusions from these ANOVA studies.

5.3.5 Interaction between heat-treatment time and heat-treatment temperature

While the chosen heat-treatment times were all long enough for significant crystallization to occur, the diffusion of polymer chains across interfaces associated with increases in bonding in MEX has been shown to be dependent on time and temperature. A full factorial experiment (FFE) set was performed at the optimized print temperature, 300 °C, in order to determine if the interaction between heat-treatment time and heat-treatment temperature was significant. After completion of the confirmation experiments, only four additional combinations of parameters were needed to understand the interaction between heat-treatment time and temperature. The control parameter combinations of the FFE are shown in Table 5.10 along with the results of the experiments. Interaction plots between heat-treatment time and temperature are shown for UTS, Young's modulus, and percent crystallinity in Figure 5.11.

Table 5.10: FFE control parameter combinations used to examine the interaction between heat-treatment time (B) and heat-treatment temperature (C) at the optimized print temperature (B) level, 300 °C (2) for PPS MEX dogbones.

Experiment	**parameter/level**			**UTS [MPa]**	**Young's modulus [MPa]**	**Percent Crystallinity**
	A	B	C			
Exp 4	2	1	2	58.7 ± 4.3	2160 ± 36	48.1 ± 1.1 %
Exp 5	2	2	3	59.3 ± 4.2	2190 ± 89	47.0 ± 2.2 %
Exp 6	2	3	1	50.1 ± 0.3	1860 ± 29	25.7 ± 1.6 %
Confirmation Exp	2	1	3	59.9 ± 1.6	2250 ± 39	48.3 ± 2.2 %
Confirmation Exp	2	3	3	60.1 ± 2.6	2300 ± 123	48.4 ± 2.0 %
	2	1	1	45.2 ± 0.9	1790 ± 9	24.3 ± 1.0 %
	2	2	1	45.3 ± 1.2	1780 ± 17	22.8 ± 0.8 %
	2	2	2	61.9 ± 2.0	1960 ± 108	47.0 ± 1.8 %
	2	3	2	58.6 ± 0.1	1970 ± 28	47.6 ± 1.2%

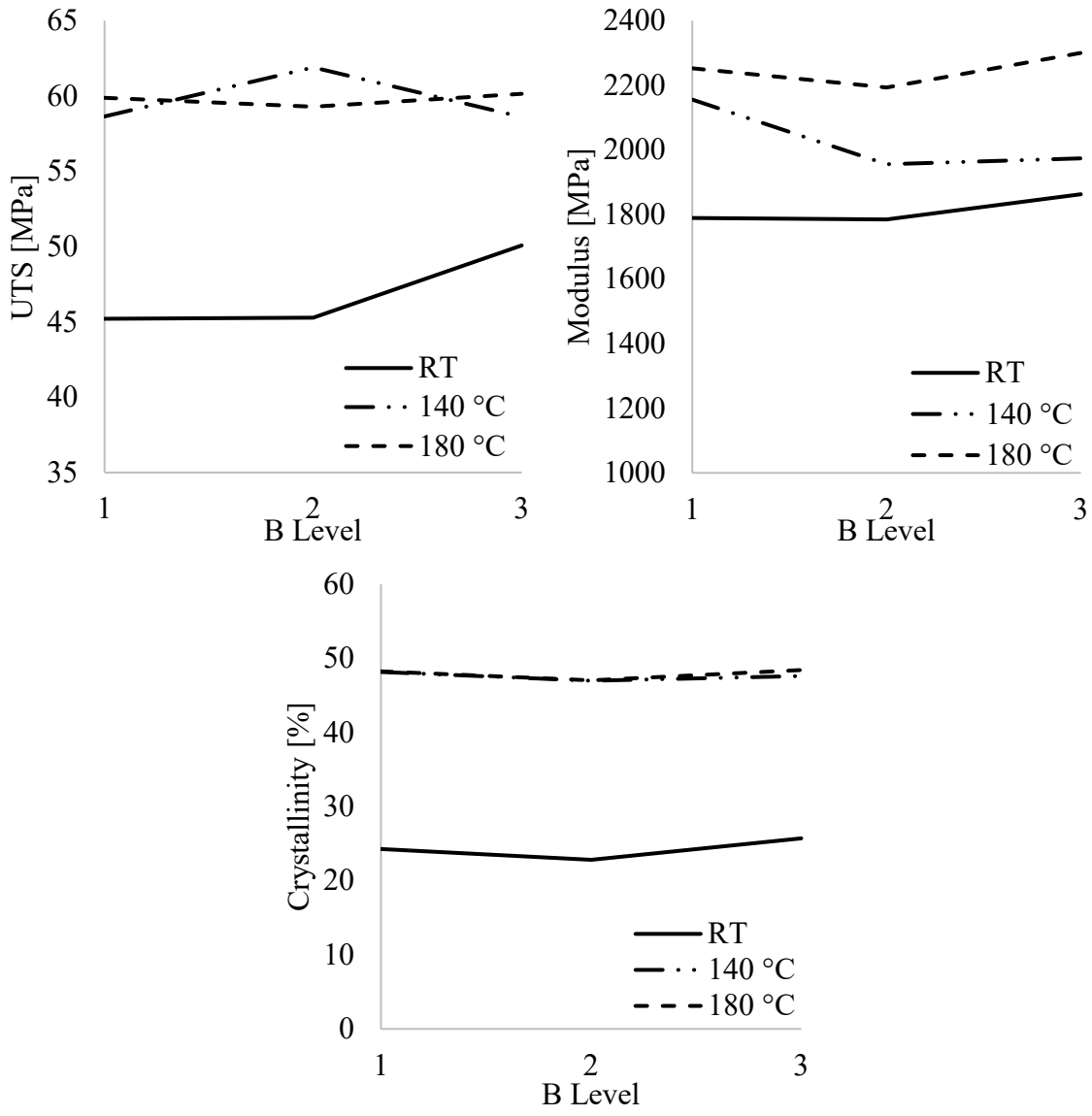

Figure 5.11: Interaction plots between heat-treatment time (B) and temperature (C) for UTS, Young's modulus and crystallinity showed similar trends between heat-treatment temperatures, which indicated that the interaction between the two parameters was not significant for the three quality aspects.

The similar trends shown by the heat-treatment temperatures at different heat-treatment times in the interaction plots indicated that the interaction between heat-treatment time and temperature was minimal. This was confirmed through ANOVA which showed that the interaction between heat-treatment time and temperature had a 1%, 3%, and 0.1% contribution to UTS, Young's modulus, and percent crystallinity, respectively. The ANOVA tables along with the Pareto plots for the FFE analysis are given in APPENDIX B in section B.2 .

Considering that the further analysis showed negligible interaction between heat-treatment time and temperature, the results obtained from the original analysis were sufficient to identify the optimal conditions for improving interlayer bonding in MEX parts. The maximized UTS and Young's modulus values that resulted from the confirmation experiments indicated that post-processing heat-treatment protocols were effective in improving interlayer bonding of MEX parts fabricated with PPS. The examination of percent crystallinity indicated that other phenomena, such as improvements in interlayer bonding, increases in inter-road bonding, or reduction of internal stresses or strains in the MEX parts contributed to increased mechanical properties at higher heat-treatment temperatures.

5.4 Conclusions

The objective of this chapter was to use the Taguchi method to maximize the interlayer bonding of MEX parts fabricated with PPS to test the hypothesis that controlling the thermal exposure of MEX parts could decrease disparities between the MEX parts and

bulk materials. The control parameters that were studied included print temperature and post-processing heat-treatment time and temperature. The selected parameters differed from previously studied parameters because they were material dependent instead of strictly process dependent parameters.

Mechanical testing was performed perpendicular to the layer in order to characterize the interlayer bonding in the PPS MEX parts. The interlayer bonding was examined because it has been shown to exhibit the lowest mechanical properties in MEX parts compared to when parts are tested parallel to the layer direction. Mechanical testing showed that samples that were not exposed to elevated temperature heat-treatments possessed the lowest mechanical properties of the tested samples. Utilizing elevated temperature post-processing heat-treatments improved the mechanical properties and increased the crystallinity of the PPS MEX parts.

The S/N ratio analysis was used to determine the optimum control parameter combination. For UTS, a 300 °C print temperature, 24-hour heat-treatment time, and 180 °C heat-treatment temperature resulted in the highest S/N ratio. For Young's modulus and percent crystallinity, a 300 °C print temperature, 10-minute heat-treatment time, and 180 °C heat-treatment temperature resulted in the highest S/N ratio. ANOVA showed that heat-treatment temperature was the most significant control parameter to UTS, Young's modulus, and percent crystallinity. Similar levels of crystallinity were achieved in samples at both elevated heat-treatment temperatures. The similar levels of crystallinity suggested that other phenomena besides crystallinity contributed to the improvement in UTS and Young's modulus of samples heat-treated at the 180 °C heat-treatment temperature. Optical

microscopy images showed increases in inter-road bonding with increasing print temperature and increasing heat-treatment temperature.

Utilizing post-processing heat-treatments on PPS MEX parts increased their mechanical properties when tested perpendicular to the layer. The UTS increased from 52% of the PPS film UTS to 80%. Similar increases were seen in the Young's modulus, from 57% of the PPS films Young's modulus to 72%. The study showed that utilizing post-processing heat-treatments on MEX parts could improve the interlayer and inter-road bonding in these parts and increase the use of MEX parts in end use applications.

CHAPTER 6. CONCLUSIONS AND FUTURE WORK

The objective of this dissertation was to examine semicrystalline polymers for use in MEX and determine how molecular behavior unique to semicrystalline materials affects the realized MEX part properties. PPS was used as a case study material in process simulation models, FSC, and process optimization studies using the Taguchi method.

Process simulation models were developed for MEX to test the hypothesis that correlations between material properties and the deformation characteristics of MEX parts could be established. The process simulation models showed that the CTE was directly proportional to MEX part warpage and were able to predict the thermal exposures experienced during MEX part fabrication. The process simulation models could be used in new material development strategies for MEX to expand the available MEX materials. In future work, some of the assumptions and limitations in the developed process simulation models could be addressed. Modeling additional material properties as functions of temperature could increase the accuracy of the model since many of the parameters are known to vary with temperature. In addition, modeling the viscoelasticity of PPS could result in changes in the calculated stresses and deformations. While the use of the power-law model did express viscosity as a function of shear rate, it did not account for a yield stress in PPS and has shown limitations in wide ranges of shear rates. Modeling viscosity using a Bird-Carreau law dependence would more accurately describe the evolution of the deposited roads since it is bounded at vanishing shear rates. In addition, accounting for the relaxation exhibited by viscoelastic materials may reduce the calculated residual stresses.

Increasing the geometrical complexity of the model could also yield interesting results. By increasing the number or road depositions, relationships could be made between the print temperature and the number of layers that are reheated during the subsequent depositions. Increasing the model to three-dimensions could also allow the variation of cooling rates and temperatures within a part to be studied more extensively. Three-dimensional examination of MEX could also provide better predictions of road geometry evolution which could in turn be used to improve the contact assumption between roads. Improvements to the material property assumptions and increasing in geometrical complexity of the process simulation models would likely drastically increase the computational expense of the simulations.

Additional experimental validation of the model would also be beneficial. Case studies could be performed with additional semicrystalline polymers that exhibit large, measureable warpage. Composite filaments could be fabricated with reduced CTE and increased thermal conductivity and the changes in warpage could be used to validate the process simulation models.

The effects of the MEX thermal exposures simulated by the process simulation models on the crystallization behavior of PPS were examined using FSC. FSC was shown to capture aspects of MEX processing through the use of its high heating and cooling rates. It showed the evolution of crystallinity during cycles of heating and cooling experienced during MEX fabrication and confirmed the hypothesis that MEX thermal exposures hindered PPS crystallization. FSC could be used with other semicrystalline polymers considered for use with MEX to understand what thermal exposures would result in crystallization during fabrication. This method could be used in conjunction with process

simulation models to predict the warpage and deformation characteristics based on material properties, cooling rates, and crystallization behavior. Additional knowledge of the exact thermal cycling and heating and cooling rates seen for standard parts produced with MEX could also be used in the future to develop a protocol for using FSC to predict the crystallinity and warpage behavior of MEX parts.

Based on the effect of thermal exposures on the crystallization behavior of PPS, it was hypothesized that control of the thermal exposure of MEX parts could decrease the disparities in mechanical properties between MEX and bulk parts. This hypothesis was confirmed using the Taguchi method for process optimization. Post-processing heat-treatment methods were shown to increase MEX part crystallinity and interlayer and inter-road bonding in PPS MEX parts leading to increased mechanical property performance. In addition, increasing print temperature was shown to increase inter-road bonding and resulting mechanical properties of MEX parts. In future work, the observations on using post-processing heat-treatments to increase the interlayer bonding of MEX parts fabricated with PPS could be used as a guide for developing post-processing heat-treatment strategies for other semicrystalline polymers. In addition, the effect of post-processing heat-treatments on the mechanical properties of PPS MEX parts fabricated in the horizontal build orientation could also be explored. When using post-processing heat-treatments on increasingly complex geometries, dimensional changes due to shrinkage from crystallization may become significant. Further study of dimensional changes from post-processing annealing would aid in the application of heat-treatments to improve MEX part mechanical property performance with semicrystalline materials.

The combination of process simulation models, thermal and mechanical characterization, and process optimization techniques studied in this dissertation developed a methodology for successfully printing high quality MEX parts using semicrystalline materials. This research suggests that slowly crystallizing polymers would be well suited for use in MEX. Controlling thermal exposure variables during fabrication would result in a largely amorphous part that could be further crystallized in post-processing heat-treatments to increase the inter-road and interlayer bonding, which would increase the resulting mechanical properties. In order to fully understand semicrystalline polymers in MEX, additional work studying semicrystalline polymers with a wide range of crystallization kinetics is needed. Cooling sufficiently quickly during fabrication to produce amorphous parts with faster crystallizing materials may decrease the warpage due to crystallization, but could increase the warpage resulting from larger thermal gradients within the part. Understanding how to balance these effects while maintaining adequate interlayer bonding could increase the use of semicrystalline polymers as MEX materials.

APPENDIX A. CONSTITUITIVE EQUATIONS IN PROCESS SIMULATION MODELS

A.1 Governing equations used in process simulation models

The process simulation models road 1 deposition, road 1 cooling, and road 2 cooling described in CHAPTER 3 were modeled in ANSYS® Polyflow using the generalized Newtonian non-isothermal flow solver. Using this category, PPS was modeled as an inelastic non-Newtonian flow. The generalized Newtonian non-isothermal flow solver has the capability to model aspects of polymer non-Newtonian behavior, such as the shear rate dependence of viscosity, but the other characteristics of viscoelastic flows, such as memory effects associated with elasticity, were not modeled.

In the process simulation models, the momentum equation, the incompressibility equation, and the energy equation were solved for simultaneously. The momentum equation is given by Equation A.1,

$$-\nabla p + \nabla \cdot \boldsymbol{T} + \boldsymbol{f} = \rho \boldsymbol{a} \tag{A.1}$$

where p is the pressure, $\boldsymbol{T}$ is the extra-stress tensor, $\boldsymbol{f}$ is the volume force, ρ is the density, and $\boldsymbol{a}$ is the acceleration. The extra-stress tensor is given by Equation A.2,

$$\boldsymbol{T} = 2\eta \boldsymbol{D} \tag{A.2}$$

where $\boldsymbol{D}$ is the rate-of-deformation tensor and η is the viscosity. The viscosity was modeled as a function of shear rate using the power-law model (Equation 3.2) and as a function of temperature using the Arrhenius model (Equation 3.3). The local shear rate,$\dot{\gamma}$, is related to $\boldsymbol{D}$ through Equation A.3.

$$\dot{\gamma} = \sqrt{2tr(\boldsymbol{D^2})} \tag{A.3}$$

The incompressibility equation is given in Equation A.4,

$$\nabla \cdot \boldsymbol{v} = 0 \tag{A.4}$$

where $\boldsymbol{v}$ is the velocity. The energy equation used in the process simulation models is given in Equation A.5,

$$\rho c_p \frac{DT}{Dt} = -\nabla \cdot \boldsymbol{q} + r + \boldsymbol{\sigma}: \boldsymbol{D} \tag{A.5}$$

where ρ is the density, c_p is the specific heat capacity, $\frac{DT}{Dt}$ is the material derivative of the temperature, r is the heat generated per unit volume by external sources, $\boldsymbol{q}$ is the heat flux, $\boldsymbol{\sigma}$ is the Cauchy stress tensor, and $\boldsymbol{D}$ is the rate-of-deformation tensor. In the energy equation, the term $\boldsymbol{\sigma}: \boldsymbol{D}$ represents the viscous dissipation. Additionally, heat conduction within the flow is governed by Fourier's law, so the heat flux is given as Equation A.6,

$$\boldsymbol{q} = -k\nabla T \tag{A.6}$$

where k is the thermal conductivity and ∇T is the change in temperature. The material derivative of the temperature is given by Equation A.7,

$$\frac{DT}{Dt} = \frac{\partial T}{\partial t} + \boldsymbol{v} \cdot \nabla T \tag{A.7}$$

In ANSYS® Mechanical, residual stresses were calculated in the structural analysis as von Mises stress, σ_{VM}, given by the Equation A.8,

$$\sigma_{VM} = \sqrt{\frac{3}{2}\boldsymbol{\sigma}' : \boldsymbol{\sigma}'} \tag{A.8}$$

The total deformation was calculated using the total strain in the system. The total strain was the sum of the mechanical strain, $\boldsymbol{\varepsilon}_M$, and the thermal strain, $\boldsymbol{\varepsilon}_{th}$, given in Equation A.9.

$$\boldsymbol{\varepsilon} = \boldsymbol{\varepsilon}_M + \boldsymbol{\varepsilon}_{th} \tag{A.9}$$

The mechanical strain was given by Equation A.10 and the thermal strain was given by Equation A.11,

$$\boldsymbol{\varepsilon}_M = \boldsymbol{C}^{-1} : \boldsymbol{\sigma} \tag{A.10}$$

$$\boldsymbol{\varepsilon}_{th} = \Delta T \boldsymbol{\alpha}(T) \tag{A.11}$$

where $\boldsymbol{C}$ is the elasticity stiffness matrix and $\boldsymbol{\alpha}(T)$ was the CTE. The CTE was assumed to be isotropic and was treated as both a constant and a function of temperature in different process simulation models as described in CHAPTER 3.

The constitutive equation for the relationship between stress in strain in the model was therefore defined as Equation A.12.

$$\boldsymbol{\varepsilon} = \boldsymbol{C}^{-1}{:}\boldsymbol{\sigma} + \Delta T\boldsymbol{\alpha}(T) \tag{A.12}$$

The components of the elasticity stiffness matrix were related to Young's modulus (E), Poisson's ratio (v), and shear modulus (G) through the constitutive relationship for a linear elastic homogeneous material given in Equation A.13,

$$C_{ijkl} = \lambda\delta_{ij}\delta_{kl} + \mu\left(\delta_{ik}\delta_{jl} + \delta_{il}\delta_{jk}\right) \tag{A.13}$$

where δ_{ij} is the Kronecker-delta, and λ and μ are the Lamé constants given in Equation A.14 and A.15, respectively:

$$\mu = G \tag{A.14}$$

$$\lambda = \frac{vE}{(1+v)(1-2v)} \tag{A.15}$$

A.2 Thermal boundary conditions

The thermal boundary conditions applied to road 1 deposition, road 1 cooling, and road 2 deposition included imposed temperature and convection. For an imposed temperature boundary condition, the surface was maintained at the specified temperature. This boundary condition is known as a Dirichlet condition. A convective boundary condition was applied using a heat flux equation given in Equation A.16,

$$q = h(T - T_{ambient}) \tag{A.16}$$

where h is the heat convection coefficient, T is the temperature at the boundary, and $T_{ambient}$ is the environment temperature. This boundary condition is known as a Newton boundary condition. Heat exchange by radiation was assumed to be negligible in the process simulation models.

A.3 Flow boundary conditions

The flow boundary conditions applied to road 1 deposition, road 1 cooling, and road 2 deposition included inflow, zero wall velocity, and free surface. In the inflow boundary condition, a volumetric flow rate was applied to simulate the inflow of PPS material into the MEX nozzle. It was defined by a volumetric flow rate calculated in Equation 3.1. The zero wall velocity condition set the normal and tangential velocity components on the boundary section to 0 as given in Equation A.17,

$$\boldsymbol{v_n} = \boldsymbol{v_s} = 0 \tag{A.17}$$

where $\boldsymbol{v_n}$ is the normal velocity component and $\boldsymbol{v_s}$ is the tangential velocity component.

The last flow boundary condition utilized in the process simulation models was a free surface. A free-surface problem involves a boundary whose position is computed as part of the solution, since it is not known in advance. The free surface boundary condition in conjunction with the remeshing technique was used to simulate the evolution of MEX roads as they were deposited. The forces in the free surface that must be prescribed include the tangential surface force, the normal force, and the normal velocity. In the process simulation models, the normal force was set to zero and the normal velocity was determined from the inflow of the material defined by the volumetric flow rate.

In addition, the two requirements that must be satisfied for a free surface boundary include the dynamic condition and the kinematic condition. The dynamic condition for the free surfaces describes the normal force. No normal force was applied to the free surface so the dynamic condition was given by Equation A.18.

$$\boldsymbol{f} = 0 \tag{A.18}$$

The kinematic condition was set for the time-dependent problem as given in Equation A.19,

$$\left(\frac{\partial \boldsymbol{x}}{\partial t} - \boldsymbol{v}\right) \cdot \boldsymbol{n} = 0 \tag{A.19}$$

where $\boldsymbol{x}$ is the position of a node on the free surface. The direction of displacement is defined by directors, $\boldsymbol{D}$, set normal to the mesh surface. The amplitude of the nodal displacement in the $\boldsymbol{D}$ direction is called the geometrical degree of freedom, h. This geometrical degree of freedom is introduced because the position of the free surface is unknown and must be computed in the simulation. Let ψ_i^h be the shape function associated with the geometrical degree of freedom. The kinematic condition can be associated with the geometrical degree of freedom. Along the free surface, the kinematic condition, given in Equation A.20, must be satisfied,

$$\ll \boldsymbol{v} \cdot \boldsymbol{n} - \frac{\delta \boldsymbol{x}}{\delta t};\ \psi_i^h \gg = 0 \tag{A.20}$$

where << ; >> denotes the scalar product along the free surface and $\delta\boldsymbol{x}$ is the displacement of the node given as Equation A.21.

$$\delta \boldsymbol{x} = h_i \boldsymbol{D}_i \tag{A.21}$$

The tangential forces applied to the free surfaces were defined by surface tension in the process simulation models. This was defined for a curved surface as shown in Figure A.1.

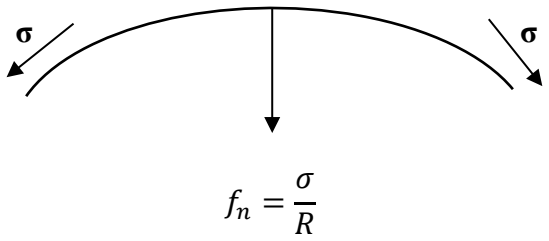

Figure A.1: The tangential forces applied to free surfaces in the process simulation models were defined by surface tension forces, $\boldsymbol{\sigma}$. The net influence of the tangential surface tension forces acted in the normal direction and tended to reduce the surface curvature.

The surface tension force was a force of amplitude σ acting tangent to the surface whose net influence was in the normal direction. This normal force per unit length, f_n, tended to reduce the surface curvature. The parameter σ was the surface tension coefficient, and satisfied the Equation A.22,

$$f_n \boldsymbol{n} = \frac{\sigma}{R} \boldsymbol{n} \tag{A.22}$$

where R is the Gaussian curvature of the surface given in Equation A.23,

$$\frac{1}{R} = \frac{1}{R_1} + \frac{1}{R_2} \tag{A.23}$$

where R_1 and R_2 are the two principal radii of curvature measured in orthogonal directions.

For boundaries with a free surface flow boundary conditions, surface tension forces were introduced on the right-hand side of the momentum equation in Equation A.1.

Introduction of Equation A.22 requires integration by parts in order to use only first order derivatives of the shape functions that characterize the geometry of the surface. Integrating the product of Equation A.22 and the velocity shape function introduces tangential forces at both ends of the free surface. These forces described the external forces on the free surface in order to equilibrate the tensile force σ. In order to maintain equilibrium with the tensile force on the free surface, the tangential force f_τ must be defined as Equation A.24,

$$f_\tau \tau = \sigma \tau \tag{A.24}$$

where τ is the unit vector tangent to the free surface directed away from the surface. An angle, θ, was used to describe the direction of τ as shown in Equation A.25.

$$\tau = \begin{pmatrix} cos\theta \\ sin\theta \end{pmatrix} \tag{A.25}$$

Figure A.2 shows the surface tension and traction at the extremities of the free surface imposed on the extrudate at the nozzle at the beginning of road 1 and road 2 deposition.

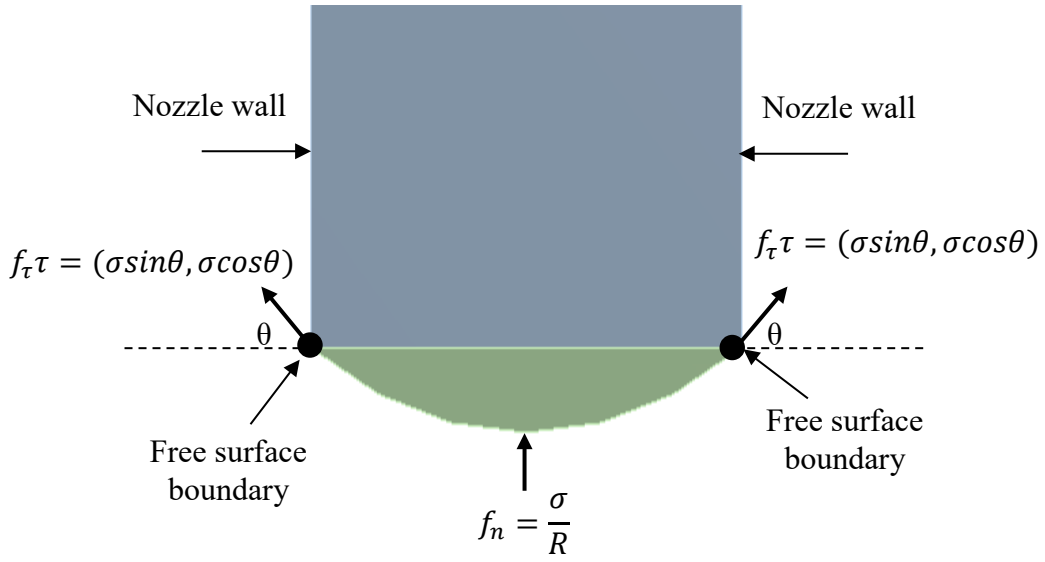

Figure A.2: Surface tension and traction at the extremities of the free surface imposed on the extrudate at the beginning of road 1 and road 2 deposition.

Contact conditions were set for the free surfaces in road 1 and road 2 deposition using the contact detection algorithm in ANSYS® Polyflow. Contact detection is a local procedure that is performed at each location along a free surface. The contact condition used on the free surface in road 1 extrusion was the blow molding contact condition. In the road 1 deposition, the extrudate was the free surface and the build platform was defined as the mold. The displacement of the free surface was calculated using a remeshing scheme where the evolving geometry was constantly re-meshed as the volumetric flow was applied. When contact was detected between the extrudate and the build platform in road 1 deposition, the thermal boundary condition of the extrudate was changed from convection to imposed temperature. The imposed temperature was equal to the build platform temperature.

In road 2 deposition, the fluid-to-fluid contact condition was applied to the free surface. The extrudate was the source of the fluid-to-fluid connected condition and the top surface of road 1 was the target. When contact was detected between the extrudate and the top of road 1, the thermal boundary condition of the extrudate was changed from convection to pure conduction between the extrudate and road 1. This contact condition assumed perfect contact between the two roads.

APPENDIX B. INTERLAYER BONDING IMPROVEMENT IN PPS MEX PARTS

B.1 Microscope images of PPS Taguchi experiments

Optical microscope images were taken of the PPS Taguchi samples described in CHAPTER 5. The side images of the experiments are shown in Figure B.1, the failure cross sections are shown in Figure B.2, and the non-failure cross sections are shown in Figure B.3.

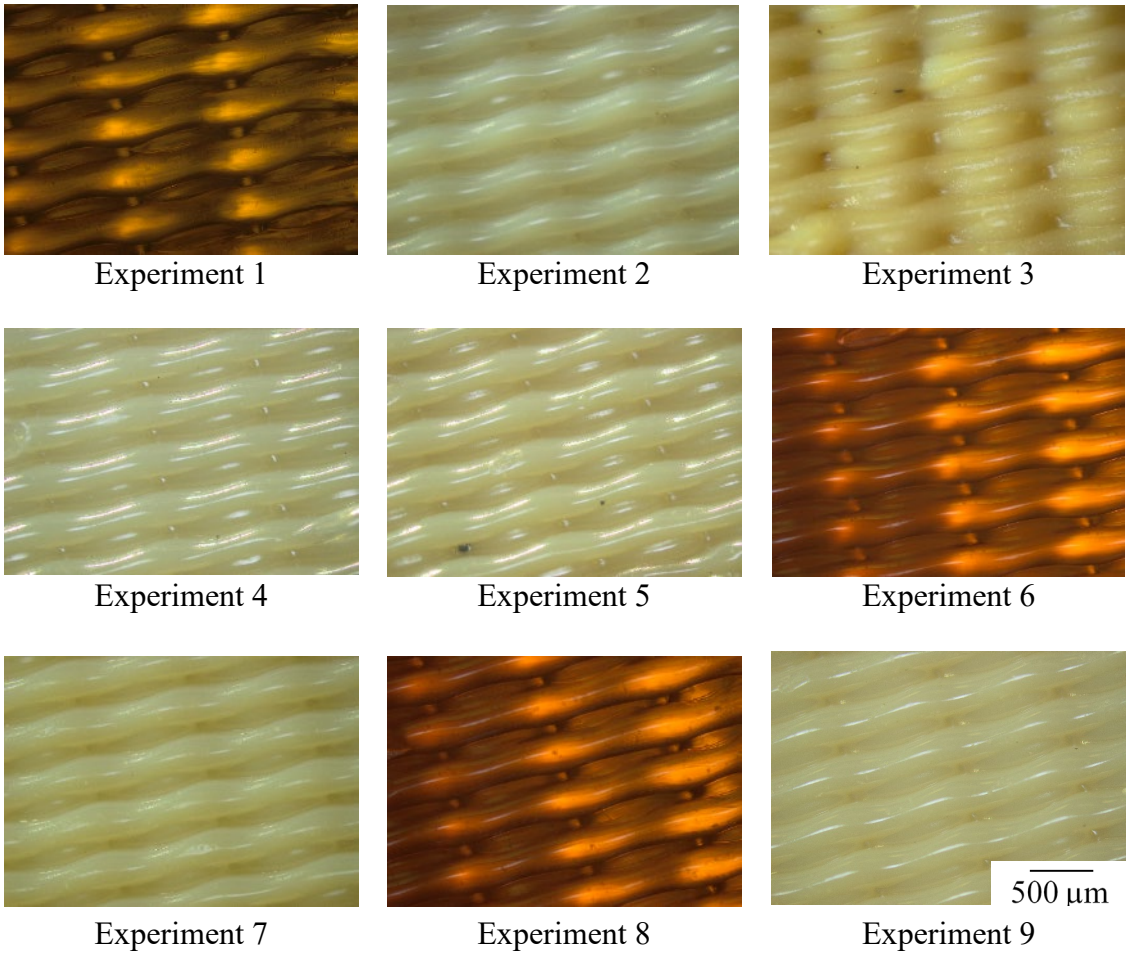

Figure B.1: Side images of each of the Taguchi experiments performed for PPS MEX dogbones. The images are similar for all experiments and the individual roads with a 90 ° raster angle can be observed. Heat-treated samples (experiments 2, 3, 4, 5, 7, and 9) were opaque due to the crystallinity that developed during heat-treating at all heat-treatment times. Non heat-treated samples (experiments 1, 6, and 8) were translucent indicating low levels of crystallinity.

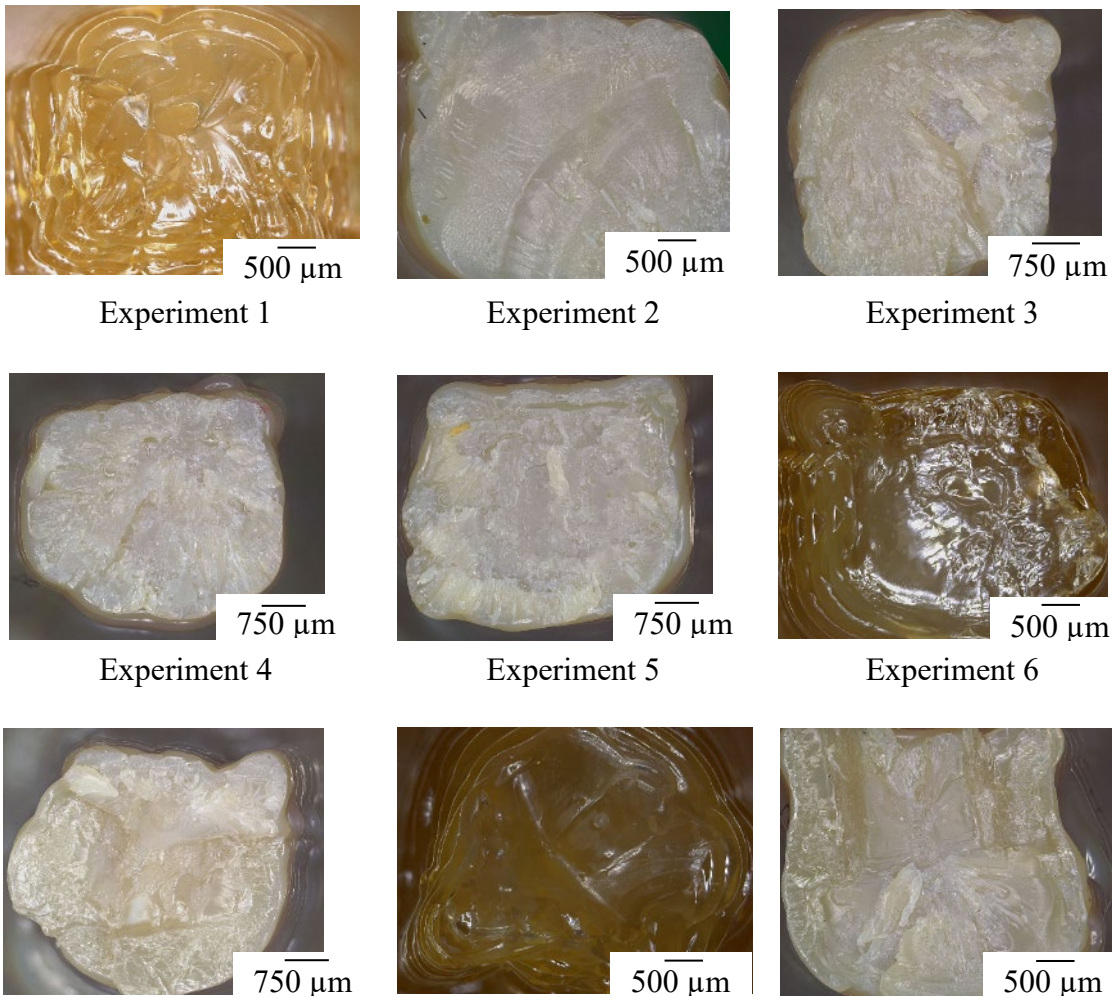

Figure B.2: Failure cross sections of each of the Taguchi experiments performed for PPS MEX dogbones. The custom z-stacking feature was used to obtain in focus images of the irregular fracture surfaces. No individual roads were observed in any of the samples.

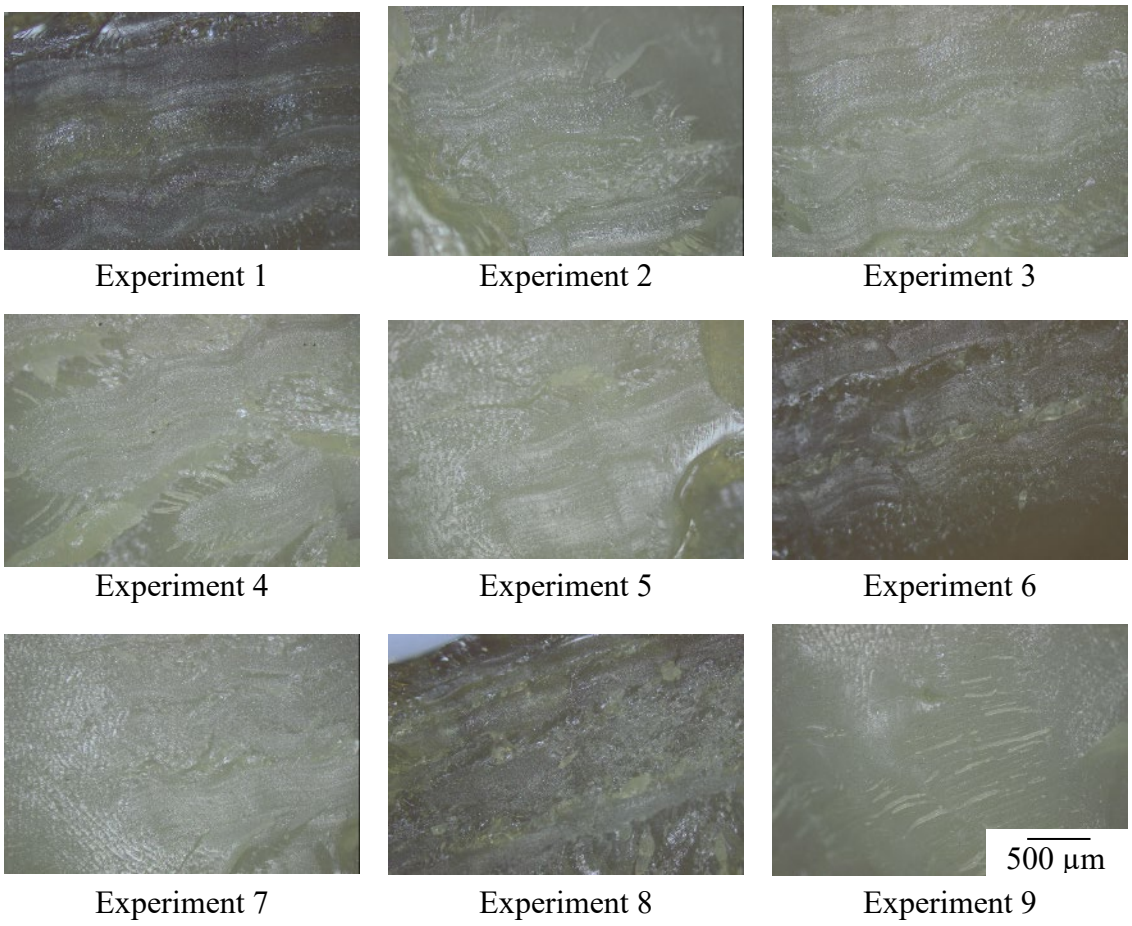

Figure B.3: Non-failure cross sections of each of the Taguchi experiments performed for PPS MEX dogbones. Individual roads can be observed in some of the non-failure cross sections, but the interfaces between roads were shown to decrease with increasing print and heat-treatment temperature.

B.2 FFE examining the interaction between heat-treatment time and temperature

An FFE set was performed at the print temperature optimized for PPS in CHAPTER 5 to determine if the interaction between heat-treatment time and temperature was significant. ANOVA performed with the original Taguchi experiments and the additional FFE experiments showed that the interaction between heat-treatment time and temperature had a 1%, 3%, and 0.1% contribution to UTS, Young's modulus, and percent crystallinity, respectively. The ANOVA tables for UTS, Young's modulus, and percent crystallinity are given Table B.1, Table B.2, and Table B.3, respectively. The percent contribution of each of the control parameters and the interaction between heat-treatment time and temperature to each design output is shown visually in Pareto plots in Figure B.4. The significance of the control parameters was evaluated with 99% confidence.

Table B.1: ANOVA table for UTS including the interaction between heat-treatment time and temperature (B x C) for PPS MEX dogbones.

Parameter	SS	DOF	Var	F-ratio	% contribution	Significant
A	319.74	2	159.869	10.89	13%	Yes
B	108.18	2	54.092	3.68	4%	No
C	1571.29	2	785.646	53.5	62%	Yes
B x C	20.13	4	5.032	0.34	1%	No
Error	499.26	34	14.684		20%	
Total	2518.6	44				

Table B.2: ANOVA table for Young's modulus including the interaction between heat-treatment time and temperature (B x C) for PPS MEX dogbones.

Parameter	SS	DOF	Var	F-ratio	% contribution	Significant
A	73812.5	2	36906.2	2.91	6%	No
B	68278	2	34139	2.69	6%	No
C	1010433	2	505216.5	39.81	84%	Yes
B x C	33801.9	4	8450.5	0.67	3%	No
Error	12691.9	34	12691.9		1%	
Total	1199017.3	44				

Table B.3: ANOVA table for percent crystallinity including the interaction between heat-treatment time and temperature (B x C) for PPS MEX dogbones.

Parameter	SS	DOF	Var	F-ratio	% contribution	Significant
A	1.38	2	0.69	0.12	0%	No
B	26.17	2	13.09	2.3	1%	No
C	4793.99	2	2396.99	420.49	95%	Yes
B x C	5.46	4	1.37	0.24	0.1%	No
Error	193.82	34	5.7		4%	
Total	5020.82	44				

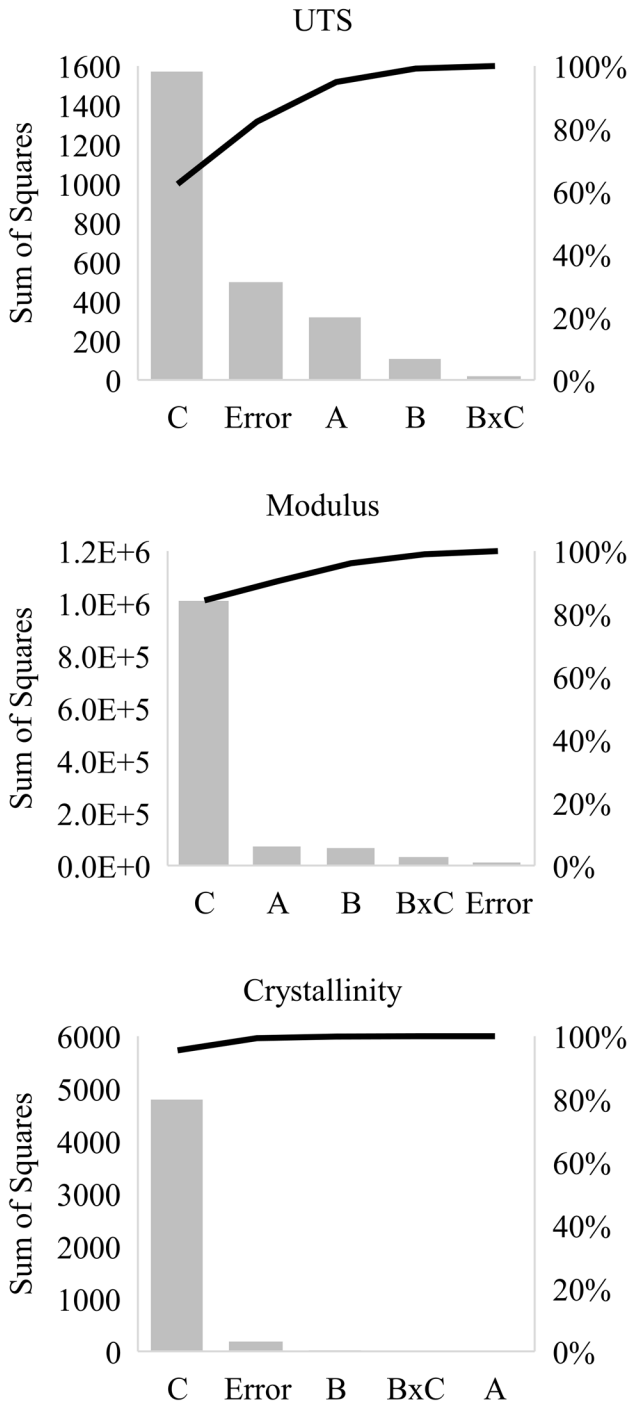

Figure B.4: Pareto plots for UTS, Young's modulus, and crystallinity showed the percent contributions of each control parameter and the interaction between heat-treatment time and temperature based on the SS analysis.

APPENDIX C. INTERLAYER BONDING IMPROVEMENT IN NORYL MEX PARTS USING THE TAGUCHI METHOD

C.1 NORYL as a new MEX material

An interesting engineering thermoplastic that has not been developed for the MEX process is a fully miscible blend of polystyrene (PS) and polyphenylene oxide (PPO) known as NORYL [1], [2]. The addition of PS to PPO both increased the processibility of PPO and decreased its overall cost while maintaining high heat resistance and excellent dimensional stability [3]-[5]. Previous studies have shown that amorphous polymers, including NORYL, have the ability to crack heal and strengthen interface adhesion at temperatures below their glass transition temperatures [6]-[8]. This ability of amorphous materials could be advantageous for post-processing heat-treatments of MEX parts. Heat-treating MEX parts below their glass transition point could allow the bonding between roads and layers to improve without sacrificing the dimensional accuracy of the part.

The objective of this study was to investigate NORYL as a new material for MEX using the Taguchi method for process optimization described in CHAPTER 5. A print temperature range was determined for NORYL following the hypothesis that rheological behavior of ABS at MEX conditions can be used as a benchmark for setting MEX process variables for other polymers. This was the same procedure used to determine a print temperature range for PPS in section 5.2.2. MEX filament was also produced using NORYL pellets. Appropriate times and temperatures for heat-treatments of MEX parts were established based on bonding studies between NORYL sheets. With appropriate heat-

treatment settings established, a process optimization was performed on NORYL MEX parts using the Taguchi method for dogbones fabricated in the horizontal and vertical build orientation. The Young's modulus and UTS of the MEX parts were optimized for horizontal dogbones considering the process parameters: layer thickness, deposition temperature, heat-treatment time, and heat-treatment temperature. For vertical dogbones, layer thickness was not examined and only print temperature, heat-treatment time and heat-treatment temperature were examined similarly to the studies performed with PPS in CHAPTER 5.

C.2 Materials and methods

Pellets of NORYL blend 731-701 (black) and 731-780 (grey) were obtained from SABIC. These pellets were the same blend of NORYL, but used different coloring agents. Sheets of black NORYL with a thickness of 1/16" (1.59 mm) were obtained from McMaster Carr.

C.2.1 Differential scanning calorimetry

DSC was performed on both the NORYL pellets and sheets following ASTM E1356 to confirm that they had the same glass transition temperature. Three tests were performed on each material using a TA instruments Q200 DSC. Samples were heated from 40 °C to 200 °C at a heating rate of 10 °C/min. Then, the sample equilibrated for 5 min and was cooled at a rate of 20 °C/min to 100 °C where it again equilibrated for an additional 5

min. It was then heated at 10 °C/min to 200 °C. This final heating run was used to measure the glass transition temperature.

C.2.2 Filament extrusion

MEX filament of approximately 1.75 mm diameter was fabricated using the NORYL pellets obtained from SABIC. A Brabender Intelli-Torque system was used with a ¾" single screw extruder with an L/D ratio of 25:1. The barrel had three heating zones in addition to a heating zone located in the vertical rod die, which had a diameter of 3/16" (4.76 mm) and an L/D ratio of 3:1. In order to cool the filament and minimize filament diameter variations during fabrication, a water bath was used between the extruder die and the take-up system. Before extrusion, the NORYL pellets were dried in a vacuum oven at 110 °C for 3 hrs. The temperature profile of the extruder, starting with zone 1 in the barrel and ending with the die temperature, was 250 °C, 260 °C, 270 °C, and 280 °C. A screw speed of 28 RPM was used.

C.2.3 Capillary rheology

Capillary rheology was performed on both blends of NORYL pellets using the Dynisco LCR7001 capillary rheometer. The capillary die used in this study had an L/D ratio of 40 with a length of 20 mm and a diameter of 0.5 mm. Experimental runs were performed at 300 °C, 310 °C, 320 °C and 330 °C for NORYL grey over a range of shear rates representative of the MEX process: 100 to 10,000 s^{-1}. For NORYL black,

experimental runs were performed at 270 °C, 290 °C and 310 °C over the same range of shear rates. The viscosity data obtained from these runs was converted from apparent viscosity to true viscosity. No Bagley correction was performed due to the limited capillary dies available for the rheometer.

C.2.4 Heat-treatment determination

NORYL sheets obtained from McMaster Carr were cut into 1” x 4” x 1/16” bars. These bars were bonded in a lap-shear joint geometry and submitted to tension loading as described in ASTM D3163. The experimental setup for bonding the bars is shown in Figure C.1.

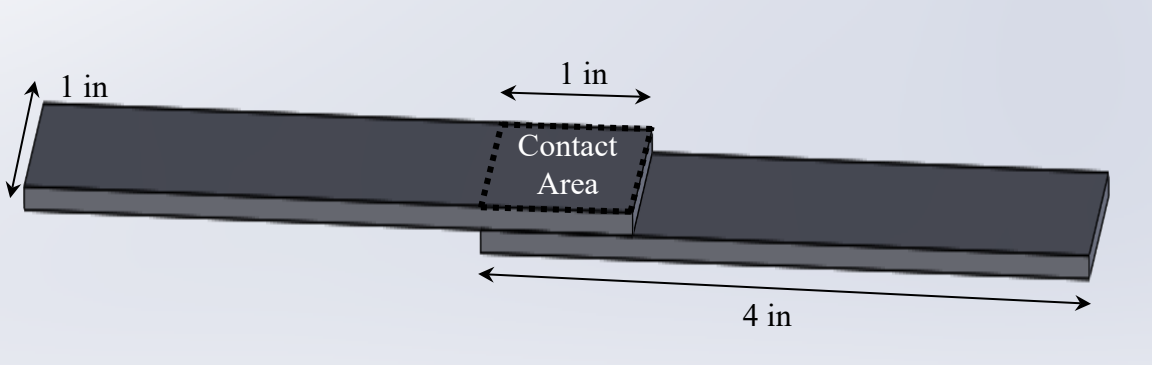

Figure C.1: The lap-shear joint experiment set up showing the contact area

In order to bond the bars together, a Carver® auto series (model no. 4389) bench top press with heated platens was preheated to the desired temperature. Five joints were

placed side by side on a 6” x 6” stainless steel plate that had also been preheated. Steel plates of 1/16” were placed under the elevated bar on the joints to ensure none of the bars were deformed during bonding. The entire setup was the placed in the hot press and allowed to preheat for 5 min. After this time, 2 tons of force was applied on the 6” x 6” platens, resulting in a pressure of 0.77 MPa, which has been shown in previous work to be sufficient pressure to provide adequate contact between the joints [6]. The set up was left for the desired contact time, which ranged from 10 min to 24 hrs. The assembly was then quickly cooled to room temperature using the water cooling capability of the Carver bench top press. The samples were then removed from the press and left at room temperature for 24 hrs. before mechanical testing.

The lap-shear joints were tested on the Instron® 5566 static tensile testing frame using a 1 kN and 10 kN load cell with a rate of elongation of 0.05 in/min (1.27 mm/min) according to ASTM D3163. Shear stress was calculated as the measured force divided by the contact area. Five joints were measured for each experimental data point.

C.2.5 Taguchi method orthogonal array

For the horizontal MEX dogbones, four process parameters, layer thickness (A), print temperature (B), heat-treatment time (C), and heat-treatment temperature (D), were examined with three levels each. Based on this selection, an L_9 orthogonal array was used for the Taguchi experimental plan as shown in Table C.1. For the vertical dogbones, print temperature, heat-treatment time, and heat-treatment temperature were examined with

three levels each similarly to the process optimization performed with PPS in CHAPTER 5 section 5.2.2. The experimental plan is given in Table 5.4.

Table C.1: Experimental plan for horizontal NORYL MEX dogbones using an L_9 orthogonal array

Experiment number	**Parameter/level**			
	A	B	C	D
1	1	1	1	1
2	1	2	2	2
3	1	3	3	3
4	2	1	2	3
5	2	2	3	1
6	2	3	1	2
7	3	1	3	2
8	3	2	1	3
9	3	3	2	1

C.2.6 MEX dogbone fabrication

The MEX additive manufacturing machine used to fabricate D638 Type V dogbones was the HYREL System 30 from HYREL International described in section 3.2.4. Horizontal dogbones were fabricated using the NORYL black filament. The dogbones were fabricated at a print speed of 15 mm/s with a 0.5 mm diameter nozzle. They were constructed using a 45° raster angle with an infill density of 100%. The dogbones had a rectilinear infill with three contours. Three contours were used so that the deposition path through the gauge length would have unidirectional rasters in the loading direction. The deposition path for a layer in the horizontal dogbones is shown in Figure C.2. The print temperature and layer thickness for the dogbones were chosen based on the orthogonal

array given in Table C.1. Three dogbones were fabricated for each experiment number given in the orthogonal array.

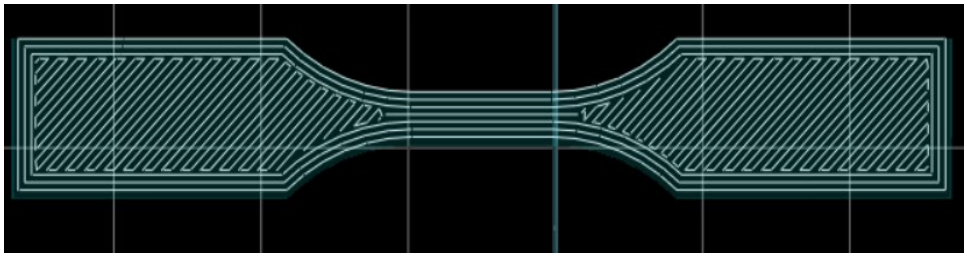

Figure C.2: Deposition path for the horizontal MEX dogbones fabricated using the NORYL black MEX filament. A raster angle of 45° raster angle with an infill density of 100% was used in the grip areas. The gauge area had unidirectional rasters in the direction of loading.

Vertical dogbones were fabricated using the NORYL grey filament according to the same procedure used to fabricate vertical PPS dogbones described in section 5.2.3. Three dogbones were fabricated for each experiment number given in the orthogonal array in Table 5.4.

The heat-treatment protocol was started 24 hrs. after the dogbones were fabricated. For the elevated temperature heat-treatments, the dogbones were placed inside a preheated furnace at the specified heat-treatment temperature for the given heat-treatment time according to the Taguchi experimental plan. Upon completion, the samples were removed from the furnace and allowed to cool to room temperature for 30 minutes before mechanical testing. Room temperature heat-treated samples were left at room temperature for their

heat-treatment time plus an additional 30 min before testing to provide consistency between the elevated temperature heat-treated samples.

C.2.7 Mechanical testing of MEX dogbones

The horizontal and vertical NORYL dogbones were tested on the Instron® 5566 static tensile testing frame following the same procedure outlined for the PPS dogbones described in section 5.2.4. ASTM D638 Type V dogbones were also cut from the NORYL sheets and tested using the same mechanical testing procedure in order to compare the MEX dogbone values to bulk mechanical property values.

C.2.8 Imaging MEX dogbones

The fracture cross sections of the NORYL black horizontal dogbones were imaged using the Leica DVM6 A microscope. The custom z-stack feature was used to obtain in focus images of the irregular fracture surfaces. Three surfaces of the NORYL grey vertical dogbones were characterized including the fracture surface, a non-failure cross section, and a side image in the grip area of the dogbone similar to the study performed on vertical PPS dogbones in CHAPTER 5.

C.3 Results and discussion

C.3.1 Glass transition temperatures from DSC

The glass transition temperature of NORYL black and grey pellets and the black NORYL sheets was determined using DSC. The onset, midpoint and endset of glass transition for the three materials are given in Table C.2. Based on the midpoint of glass transition, the composition of PPO in the NORYL blends was estimated to be 60% [3].

Table C.2: Glass transition temperature for NORYL pellets and sheets determined using DSC

Material	T_g [°C]		
	Onset	Midpoint	Endset
NORYL black pellets	135 ± 2.0	142 ± 0.6	148 ± 0.4
NORYL grey pellets	137 ± 0.8	141 ± 0.8	146 ± 0.9
NORYL black sheets	134 ± 2.0	138 ± 0.04	140 ± 0.2

C.3.2 Print temperature determination using capillary rheology

The results of the capillary rheology experiments performed on NORYL black and NORYL grey were used to determine print temperature ranges for the two materials. The viscosity equation given in Equation 3.4 was fit to the experimental data for each material and the resulting equation for NORYL black is given in Equation C.1 and the resulting equation for NORYL grey is given in Equation C.2.

$$\eta = e^{\left[8919.8\left(\frac{1}{T}-\frac{1}{583.15}\right)\right]}13213(\dot{\gamma})^{-0.58} \quad \text{(C.1)}$$

$$\eta = e^{\left[9244.2\left(\frac{1}{T}-\frac{1}{583.15}\right)\right]}9779(\dot{\gamma})^{-0.56} \quad \text{(C.2)}$$

Using Equation C.1 and C.2, viscosity surface plots were constructed to show the viscosity as a function of shear rate and temperature over a larger temperature range for NORYL black and grey. These surface plots are given in Figure C.3.

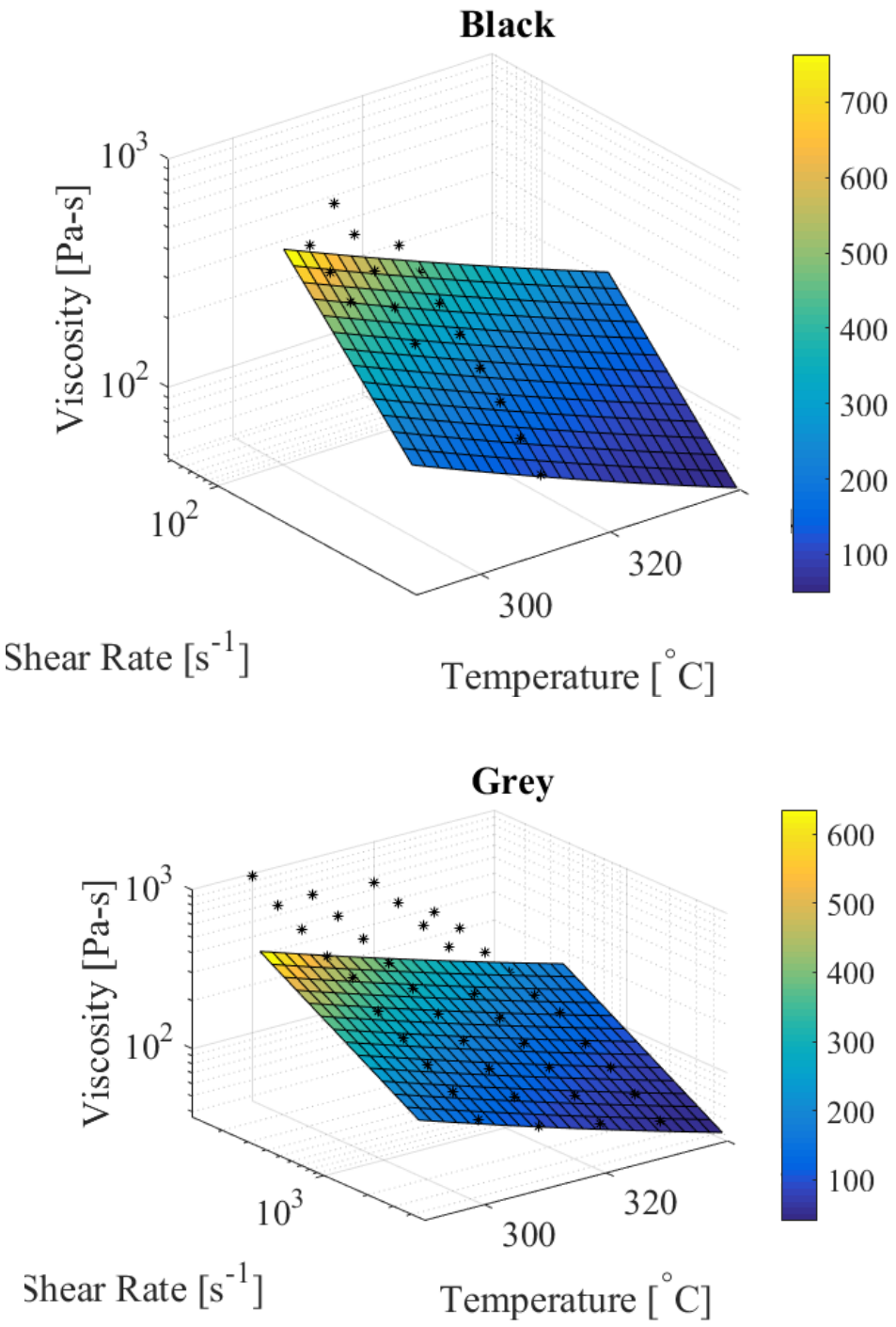

Figure C.3: Viscosity surface plots for NORYL black and grey were constructed by fitting Equation 3.4 to the experimental data. The symbols (*) represent experimental data while the surface plots were obtained for NORYL black and grey using Equation C.1 and Equation C.2, respectively. The equations were used to plot viscosity as a function of shear rate and temperature from 290 °C to 340 °C and from 100 s^{-1} to 10,000 s^{-1}

The shear rate of the HYREL System 30 MEX machine was determined to be 400 s^{-1}. At this shear rate, the viscosity of ABS at its deposition temperature was 500 Pa-s. Using Equation C.1 and C.2, the theoretical print temperature of NORYL black and grey were determined to be 296 °C and 304 °C, respectively. Based on these theoretical printing temperatures, the print temperature control levels selected for examination with the Taguchi method were 295, 305, and 315 °C for both NORYL black and grey.

C.3.3 Heat-treatment determination

Based on the glass transition temperature of NORYL determined using DSC, three temperatures were examined as possible heat treatment temperatures. Temperatures of 120, 130 and 140 °C were examined at five different contact times: 10 min, 25 min, 100 min, 400 min, and 1440 min (24 hrs.). The shear strength of the bonded joints was plotted against $t^{1/4}$ and is shown in Figure C.4. No results are plotted for 120 °C because no bonding was formed in the lap shear joints at that temperature for any amount of contact time. These data showed that NORYL interfaces could crack heal at temperatures below and at the midpoint of glass transition. Based on these studies, the heat-treatment times selected for both the NORYL black horizontal dogbones and the NORYL grey vertical dogbones were 10 min, 100 min and 24 hrs. The heat-treatment temperature control levels selected for the NORYL black horizontal dogbones were room temperature, 130 °C, and 140 °C. The heat-treatment temperature control levels selected for the NORYL grey vertical dogbones were 120 °C, 130 °C, and 140 °C. Even though the performed lap shear joint experiments were

not able to develop interfacial bonding at 120 °C, previous work with NORYL has shown crack healing at 120 °C [6].

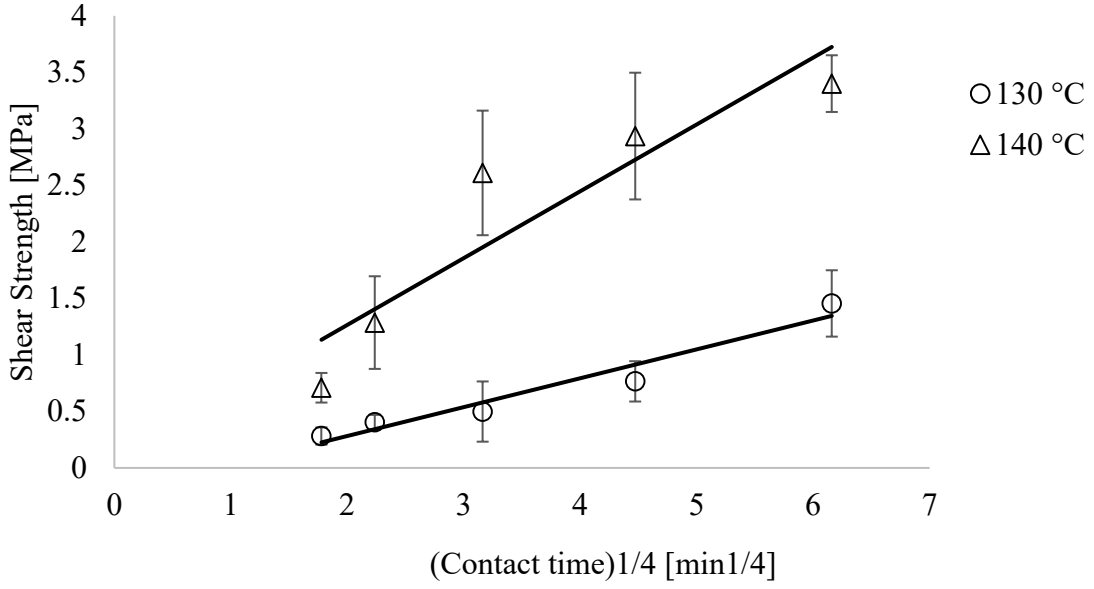

Figure C.4: Shear strength of NORYL interfaces as a function of contact time for heat-treatment times.

C.3.4 Taguchi method analysis for NORYL black horizontal MEX dogbones

The control parameter levels for layer thickness, print temperature, heat-treatment time, and heat-treatment temperature investigated for the NORYL black horizontal dogbones are given in Table C.3. The layer thickness control levels were based on standard layer thicknesses used in the MEX process. Three horizontal dogbones were fabricated with control parameter levels according to the orthogonal array in Table C.1. The UTS, Young's modulus, and strain to failure values for the Taguchi experiments are given in

Table C.4. Figure C.5 shows the stress vs. strain curves for experiments representative of the overall stress vs. strain behavior of the experiments.

Table C.3: Process parameter levels for the Taguchi analysis of NORYL black horizontal MEX dogbones.

Parameter	**Level**		
	1	**2**	**3**
A. Layer thickness	0.1 mm	0.2 mm	0.3 mm
B. Print temperature	295 °C	305 °C	315 °C
C. Heat-treatment time	10 min	100 min	1440 min
D. Heat-treatment temperature	Room temp	130°C	140°C

Table C.4: Average UTS, Young's modulus, and strain to failure for NORYL black horizontal MEX dogbones.

Experiment	**UTS [MPa]**	**Young's modulus [MPa]**	**Strain to failure [%]**
1	58.0 ± 2.0	1700 ± 78	24.1 ± 4.4
2	53.0 ± 2.9	1780 ± 43	8.8 ± 2.6
3	53.6 ± 3.4	1590 ± 87	7.5 ± 1.3
4	52.1 ± 3.0	1500 ± 63	18.1 ± 2.9
5	48.4 ± 0.7	1480 ± 6	22.4 ± 5.7
6	51.0 ± 1.4	1450 ± 85	15.3 ± 0.5
7	46.2 ± 0.9	1360 ± 17	15.1 ± 1.3
8	46.3 ± 1.7	1350 ± 68	18.0 ± 1.9
9	42.5 ± 2.3	1360 ± 91	11.5 ± 0.2

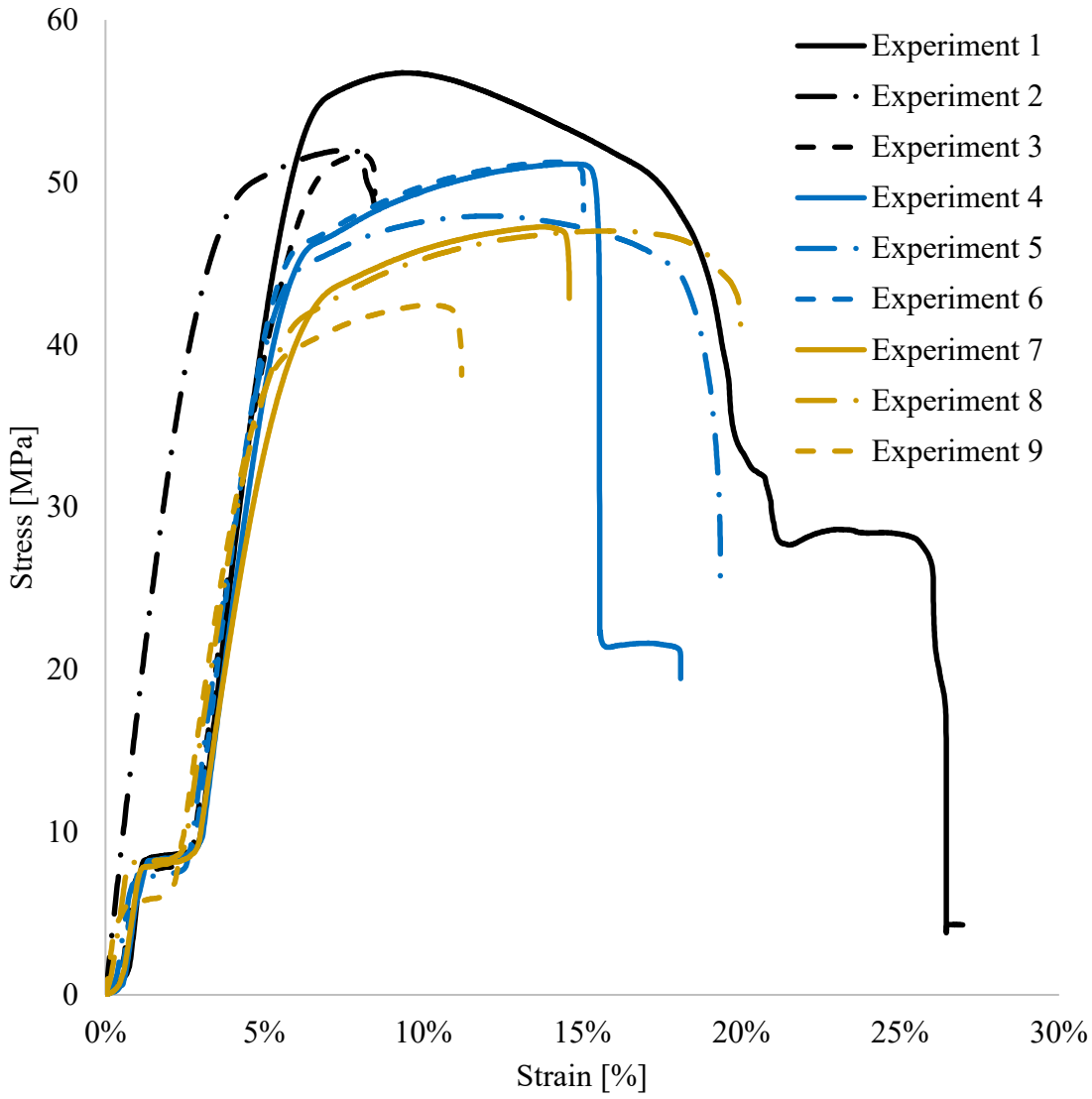

Figure C.5: Stress vs. strain curves for NORYL black horizontal MEX dogbones.

Figure C.5 shows that during testing, the horizontal MEX dogbones yielded and had strain to failure values ranging from 7.5 ± 1.3% to 24.1 ± 4.4%. Dogbones cut from the NORYL black sheets were mechanically tested and had a UTS of 65.9 ± 1.0 MPa and a Young's modulus of 2530 ± 32 MPa. The UTS values of the horizontal printed dogbones ranged from 64-88% of bulk NORYL and the Young's modulus values ranged from 53-70%.

The S/N ratios for UTS and Young's modulus were calculated using the "larger is better" S/N ratio equation in Equation 5.3. The average S/N ratio for each control parameter level was also calculated. These results are shown graphically in Figure C.6. ANOVA was also performed for both UTS and Young's modulus to determine which control parameters were significant to each design output. The ANOVA tables for UTS and Young's modulus are shown in Table C.5 and Table C.6, respectively. The percent contribution of each control parameter to each design output are shown visually in the Pareto plots in Figure C.7. The significance of the control parameters was evaluated with 99% confidence.

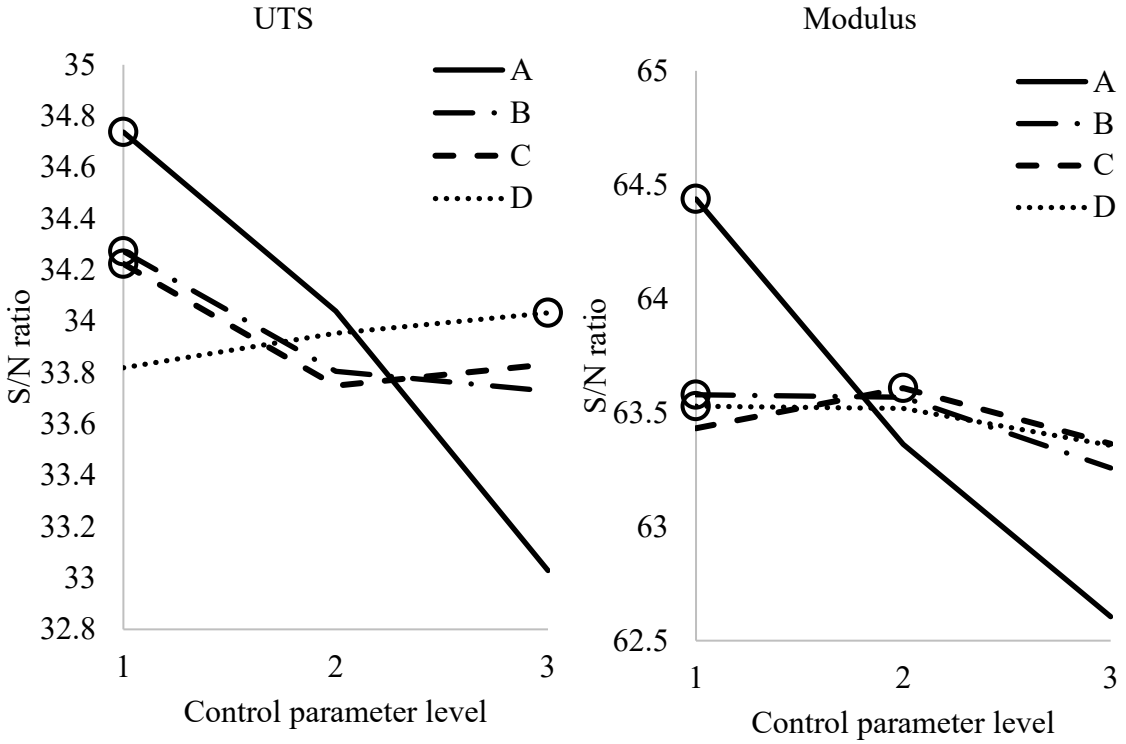

Figure C.6: Parameter level effect plots for UTS and Young's modulus for NORYL black horizontal MEX dogbones. The optimum parameter condition for UTS and Young's modulus were determined by maximizing the S/N ratio for each control parameter, indicated by the ○ on the plot. The optimum layer thickness (A) and print temperature (B) for both UTS and Young's modulus were 0.1 mm and 295 °C, respectively. The optimum heat-treatment time (C) for UTS was 10 min while the optimum level for Young's modulus was 100 min. The optimum heat-treatment temperature (D) for UTS was 140 °C while the optimum level for Young's modulus was room temperature.

Table C.5: ANOVA table for the UTS of NORYL black horizontal MEX dogbones.

Parameter	SS	DOF	Var	F-ratio	% contribution	Significant
A	439.578	2	219.789	30.06827	66%	Yes
B	52.977	2	26.4885	3.623763	8%	No
C	36.821	2	18.4105	2.518651	5%	No
D	4.712	2	2.356	0.322313	1%	No
Error	131.574	18	7.309667		20%	
Total	665.662	26				

Table C.6: ANOVA table for the Young's modulus of NORYL black horizontal MEX dogbones.

Parameter	SS	DOF	Var	F-ratio	% contribution	Significant
A	462768.7	2	231384.4	34.72192	75%	Yes
B	16519.4	2	8259.7	1.239464	3%	No
C	11010.1	2	5505.05	0.826097	2%	No
D	5716.1	2	2858.05	0.428884	1%	No
Error	119950.7	18	6663.928		19%	
Total	615965	26				

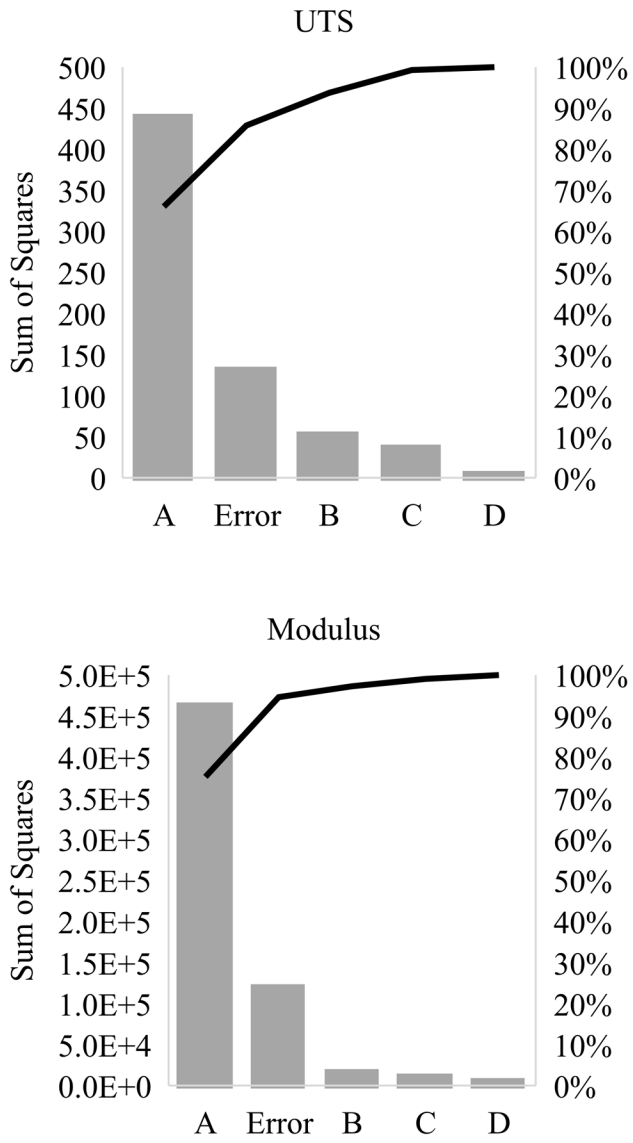

Figure C.7: Pareto plots for UTS and Young's of NORYL black horizontal MEX dogbones showed the percent contributions of each of the control parameters based on the SS analysis. Layer thickness (A) had the largest contribution to both UTS and Young's modulus. None of the other control parameters were significant to UTS or Young's modulus.

The optimum parameter condition for each design output was determined by maximizing the average S/N ratio for each control parameter. The optimum parameter condition for UTS was a layer thickness (A) of 0.1 mm, a print temperature (B) of 295 °C, a heat-treatment time (C) of 10 min, and a heat-treatment temperature (D) of 140 °C. The optimum parameter condition for Young's modulus had the same levels for layer thickness and print temperature. The optimum levels for heat-treatment time and temperature for Young's modulus were 100 min and room temperature, respectively. However, according to ANOVA, the only control parameter significant to UTS and Young's modulus was the layer thickness. Therefore, the only level effectively optimized from the S/N ratio analysis was the layer thickness. For the other control parameters, the average S/N ratios at all levels were not statistically different. Because only layer thickness was shown to be significant to UTS and Young's modulus, no confirmation experiments were performed. The contribution of error to UTS and Young's modulus in ANOVA was 20% and 19%, respectively. The error contribution was low enough in both ANOVA studies to conclude that the control parameters significant to the design outputs were adequately controlled.

The effect of layer thickness on the horizontal MEX dogbones was examined by taking optical microscopy images of the fracture surfaces of the samples. Many of the roads in the cross sections yielded during testing resulting in highly deformed fracture surfaces. The custom z-stacking feature of the microscope was used to obtain in focus images of the uneven surfaces. These images are shown in Figure C.8.

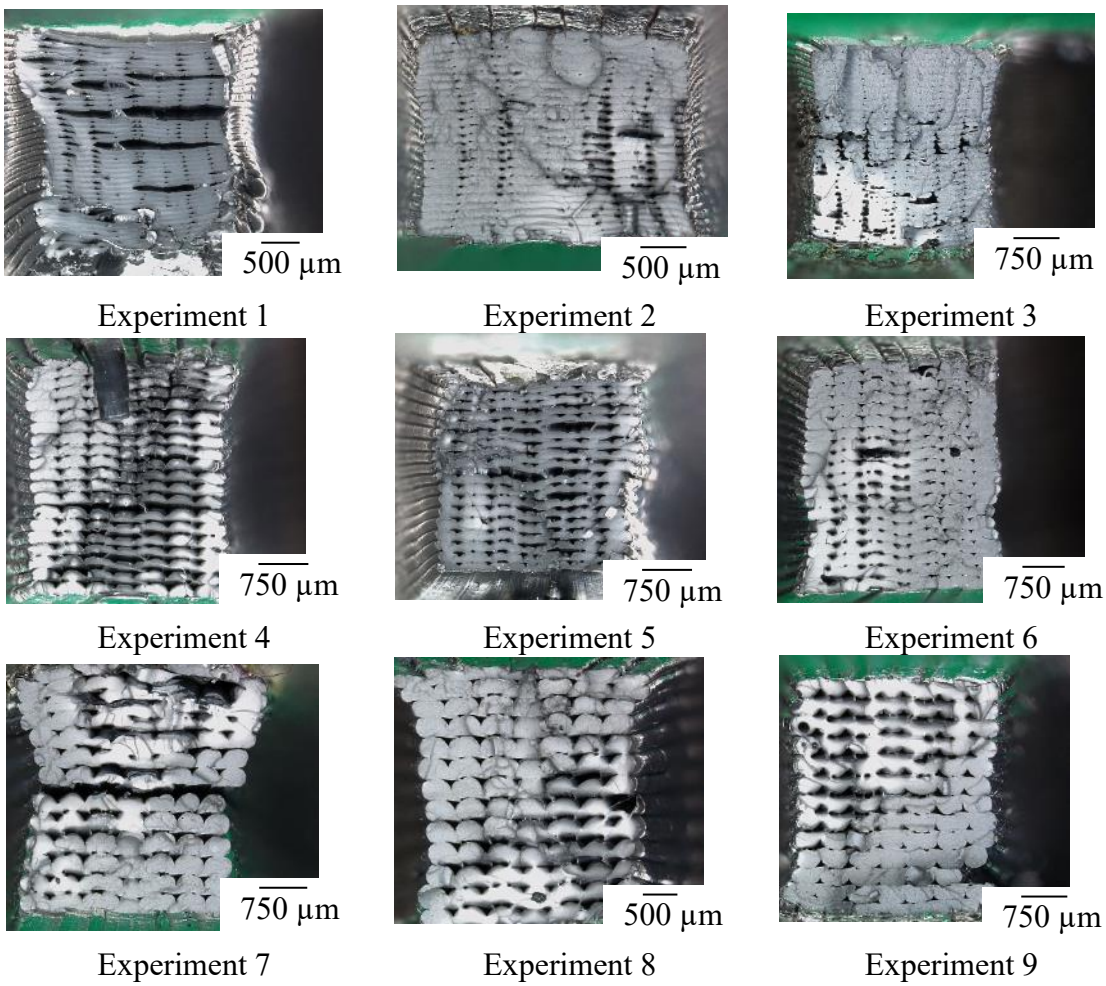

Figure C.8: Fracture surfaces of horizontal NORYL MEX dogbones. The size of the voids present between roads increased with increasing layer thickness, resulting in reductions in mechanical properties.

The microscope images of the fracture surfaces shown in Figure C.8 showed that increasing layer thickness increased the size of the voids present between roads. Samples fabricated with the largest layer height of 0.3 mm had the lowest mechanical properties due to the loss of load carrying capacity from the increased presence of voids. Dogbones fabricated with the smallest layer thickness, 0.1 mm, had the fewest, smallest voids and therefore exhibited the highest mechanical properties. The reduction in void size with decreasing layer thickness was the result of the increased compression of the NORYL road as it was deposited at lower thicknesses.

C.3.5 Taguchi method analysis for NORYL grey vertical MEX dogbones

Following the Taguchi method analysis performed using NORYL black to fabricate horizontal MEX dogbones, an additional process optimization was performed to understand the effect of heat-treatments on mechanical properties of MEX parts. Because layer thickness had a large effect on the mechanical properties of the fabricated dogbones, it was not studied in the subsequent process optimization in order to more closely examine the other parameters. In addition, the build orientation of the dogbones was changed from horizontal to vertical. By fabricating the dogbones in the vertical build orientation, the interlayer bonding strength of the dogbones was characterized. This interface has been shown to exhibit the weakest bonding in MEX parts [9]-[14]. Based on the increases in interfacial bonding shown in the NORYL sheets in section C.3.3, it was hypothesized that heat-treatments could improve the interlayer bonding in NORYL MEX dogbones. Due to

limited material, NORYL grey was used to fabricate the vertical dogbones instead of NORYL black used for the horizontal dogbones.

The control parameter levels for print temperature, heat-treatment time, and heat-treatment temperature used during the process optimization with NORYL grey vertical dogbones are given in Table C.7. Three horizontal dogbones were fabricated with the print temperatures and heat-treatment conditions specified in the orthogonal array in Table 5.4. In addition, three dogbones were fabricated using a print temperature of 295 °C and were not heat-treated. These dogbones are referred to as room temperature samples throughout this section. The UTS, Young's modulus, and strain to failure values for the Taguchi experiments and the room temperature samples are given in Table C.8. Figure C.9 shows the stress vs. strain curves for experiments representative of the overall stress vs. strain behavior of the experiments.

Table C.7: Process parameter levels for the Taguchi analysis of NORYL grey vertical MEX dogbones.

Parameter	**Level**		
	1	**2**	**3**
A. Print temperature	295 °C	305 °C	315 °C
B. Heat-treatment time	10 min	100 min	1440 min
C. Heat-treatment temperature	120°C	130°C	140°C

Table C.8: Average UTS, Young's modulus, and strain to failure for NORYL grey vertical MEX dogbones.

Experiment	UTS [MPa]	Young's modulus [MPa]	Strain to failure [%]
1	18.0 ± 1.0	1250 ± 10	2.0 ± 0.3
2	18.8 ± 0.3	1270 ± 78	2.0 ± 0.1
3	17.3 ± 0.2	1270 ± 37	1.7 ± 0.1
4	24.2 ± 0.2	1390 ± 91	2.7 ± 0.2
5	26.6 ± 1.9	1430 ± 91	2.9 ± 0.3
6	24.8 ± 2.2	1400 ± 46	2.7 ± 0.4
7	26.8 ± 2.2	1420 ± 92	3.0 ± 0.4
8	24.9 ± 1.4	1450 ± 61	2.6 ± 0.1
9	24.2 ± 1.4	1350 ± 26	2.7 ± 0.2
RT	20.6 ±1.9	1260 ± 41	2.4 ± 0.5

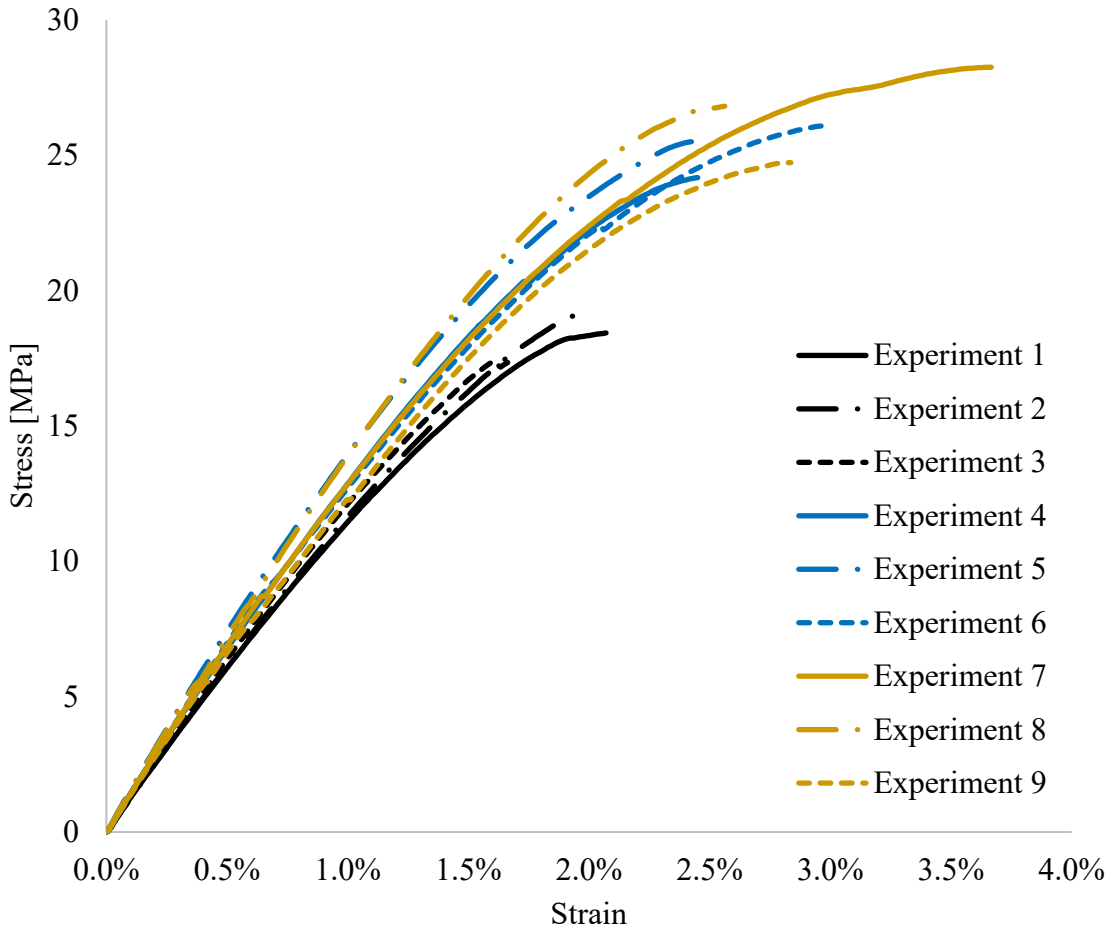

Figure C.9: Stress vs. strain curves for NORYL grey vertical MEX dogbones.

Figure C.9 shows that NORYL grey dogbones printed at the lowest print temperature of 295 °C (experiments 1, 2 and 3) had the lowest mechanical properties and the lowest strain to failure values. The lowest UTS (experiment 3) and Young's modulus (experiment 1) from the vertical dogbones were 26% and 45% of the bulk UTS and Young's modulus, respectively. Compared to the room temperature sample fabricated at the same temperature as experiments 1, 2, and 3, heat-treatments did not appear to significantly increase the UTS or Young's modulus of those samples. Overall, the vertical dogbones exhibited lower mechanical properties and lower strain to failure values than the horizontal dogbones. The maximum UTS of the vertical dogbones (experiment 7) was 46% of the maximum horizontal dogbone UTS and only 41% of the bulk NORYL UTS. The maximum Young's modulus of the vertical dogbones (experiment 8) was 81% of the maximum horizontal dogbone Young's modulus and only 57% of the bulk NORYL UTS. This anisotropy and reduction of mechanical properties compared to bulk values was consistent with previous work with ABS [11].

The S/N ratio for UTS and Young's modulus were calculated using Equation 5.3 and the average S/N ratio for each control parameter level was also calculated. These results are shown in the parameter level effect plots in Figure C.10. ANOVA was also performed to determine which control parameter(s) were significant to UTS and Young's modulus. The ANOVA tables for UTS and Young's modulus are given in Table C.9 and Table C.10, respectively. The percent contribution of each of the control parameters to the design outputs is shown in the Pareto plots in Figure C.11. The significance of the control parameters was evaluated with 99% confidence.

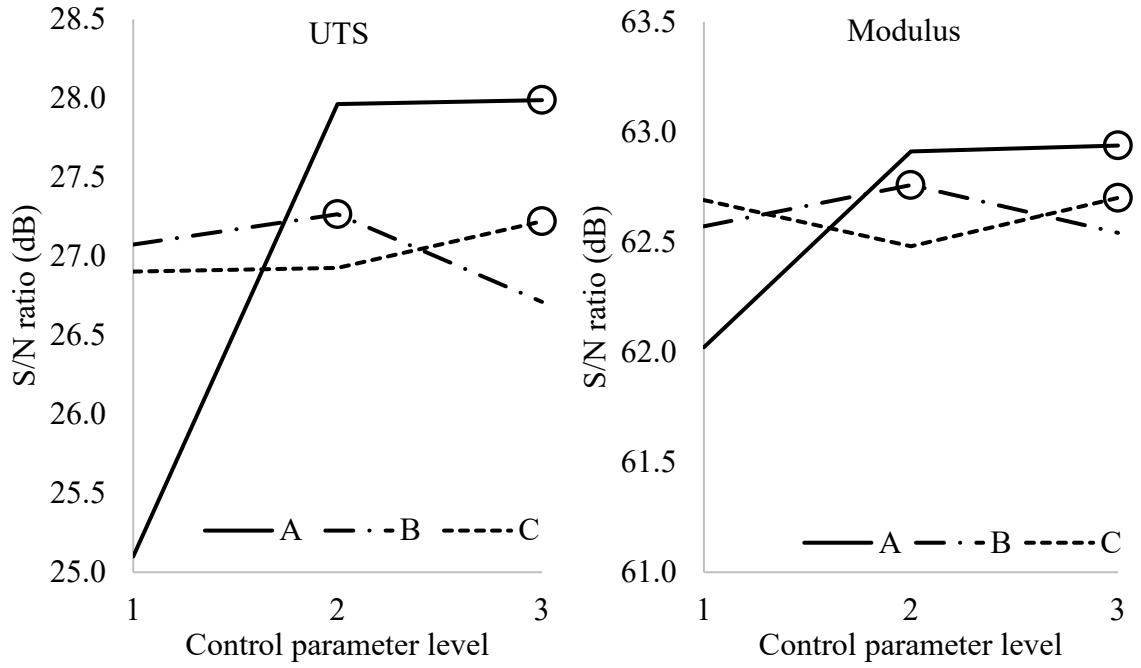

Figure C.10: Parameter level effect plots for UTS and Young's modulus for NORYL grey vertical MEX dogbones. The optimum parameter condition for UTS and Young's modulus was determined by maximizing the S/N ratio for each control parameter, indicated by the ○ on the plot. The optimum parameter condition for UTS and Young's modulus was a print temperature (A) of 315 °C, a heat-treatment time (B) of 100 min, and a heat-treatment temperature (C) of 140 °C.

Table C.9: ANOVA table for the UTS of NORYL grey vertical MEX dogbones.

Parameter	SS	DOF	Var	F-ratio	% contribution	Significant
A	311.792	2	155.896	48.43973	79.5%	Yes
B	8.775	2	4.3875	1.363276	2.2%	No
C	7.463	2	3.7315	1.159445	1.9%	No
Error	64.367	20	3.21835		16.4%	
Total	392.397	26				

Table C.10: ANOVA table for the Young's modulus of NORYL grey vertical MEX dogbones.

Parameter	SS	DOF	Var	F-ratio	% contribution	Significant
A	119724.1	2	59862.05	9.939049	47.0%	Yes
B	8019.9	2	4009.95	0.665782	3.1%	No
C	6728.7	2	3364.35	0.558592	2.6%	No
Error	120458.3	20	6022.915		47.3%	
Total	254931	26				

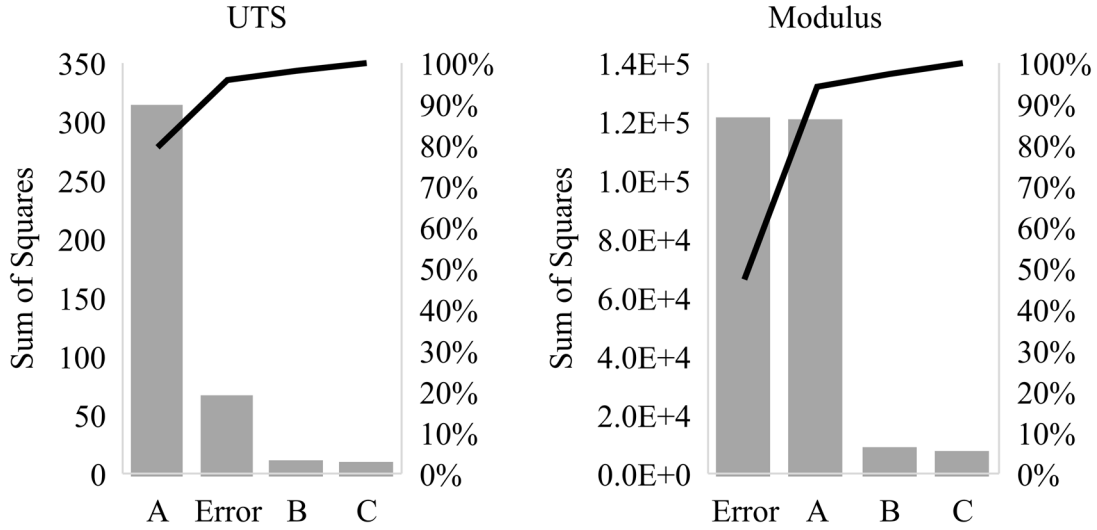

Figure C.11: Pareto plots for UTS and Young's showed the percent contributions of each of the control parameters based on the SS analysis. Print temperature (A) was the only significant control parameter to both UTS and Young's modulus. The percent contribution of error to the Young's modulus analysis was large because of the low impact of all of the control parameters.

The optimum control parameter combination for UTS and Young's modulus determined by maximizing the average S/N ratio for each parameter was a 315 °C print temperature, a heat-treatment time of 100 min, and a heat-treatment temperature of 140 °C (A3 B2 C3). ANOVA showed that the only control parameter significant to UTS and Young's modulus was print temperature. The average S/N ratios for print temperature level 2 and 3 were similar in both UTS and Young's modulus. The higher print temperatures could improve road-to-road and layer-to-layer bonding by allowing additional neck growth to form between the newly deposited road and previously deposited material [15]. This result was consistent with what was shown for vertical PPS MEX dogbones in CHAPTER 5. Because only print temperature was shown to be significant to improving the mechanical properties of the vertical MEX dogbones, no confirmation experiments were performed.

The contribution of error to UTS in ANOVA was 16.4%, indicating that optimization was successful and the control parameters significant to UTS were well controlled. However, the contribution of error to Young's modulus was 47.3%. This was due to the low impact that the control parameters had on the Young's modulus. The NORYL grey vertical MEX dogbones had Young's moduli that ranged from 1250 to 1450 MPa and experiments had an average standard deviation of 60 MPa. Because of the relatively low impact of print temperature on increasing the Young's modulus of the vertical dogbones, the variation due to error in the MEX dogbones made a significant contribution to the overall change seen in the Young's modulus. The large contribution of error indicated that the process optimization for Young's modulus did not examine control parameters that significantly influenced the modulus values.

MEX parts have been shown to have larger levels of variation than standard bulk parts due to inter-laminar defects from underflow, overflow, or the presence of excess material that sticks to the MEX nozzle [16]. These error contributions may have been significant in both the vertical and horizontal NORYL MEX dogbones because the filament used for fabrication had variations in its diameter, which could lead to inconsistencies in the MEX deposition. In order to investigate any inter-laminar defects present in the vertical MEX dogbones, optical microscope images were taken of the side, failure cross section, and non-failure cross section. The side images are shown in Figure C.12, the failure cross sections are shown in Figure C.13, and the non-failure cross sections are shown in Figure C.14. Figure C.15 shows the same images taken of the room temperature experiment.

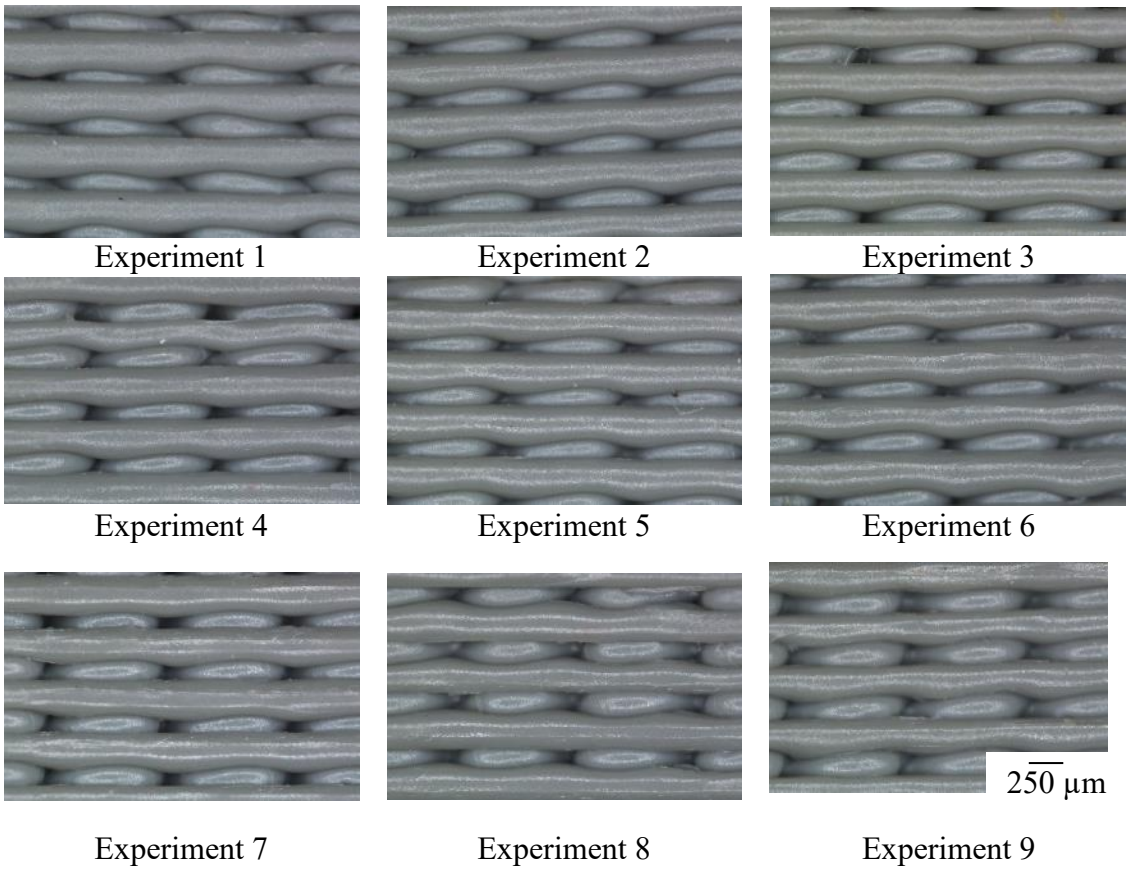

Figure C.12: Side images of each of the Taguchi experiments performed for NORYL grey vertical MEX dogbones. The images are similar for all experiments and the individual roads with a 90 ° raster angle can be observed.

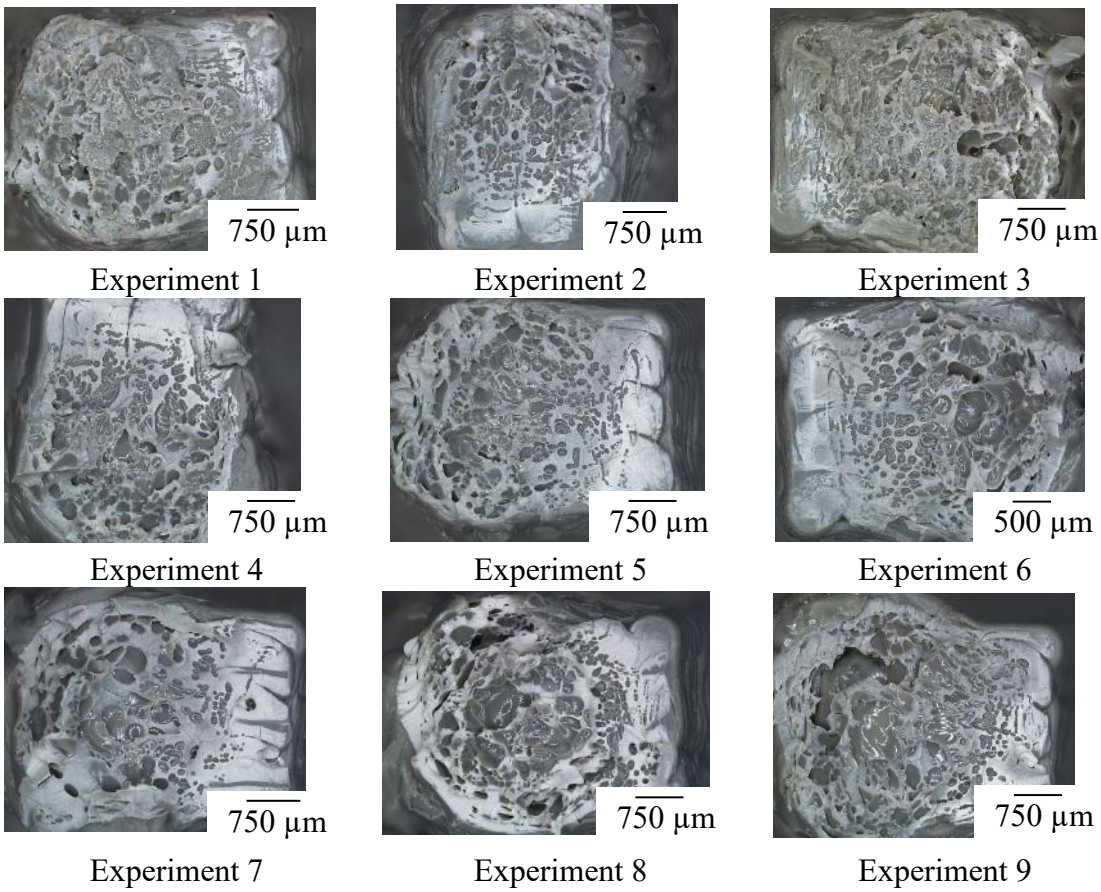

Figure C.13: Failure cross sections of each of the Taguchi experiments performed for NORYL grey vertical MEX dogbones. The samples did not fail cleanly at an interface and instead failed within the layer due to the large voids within the deposited roads.

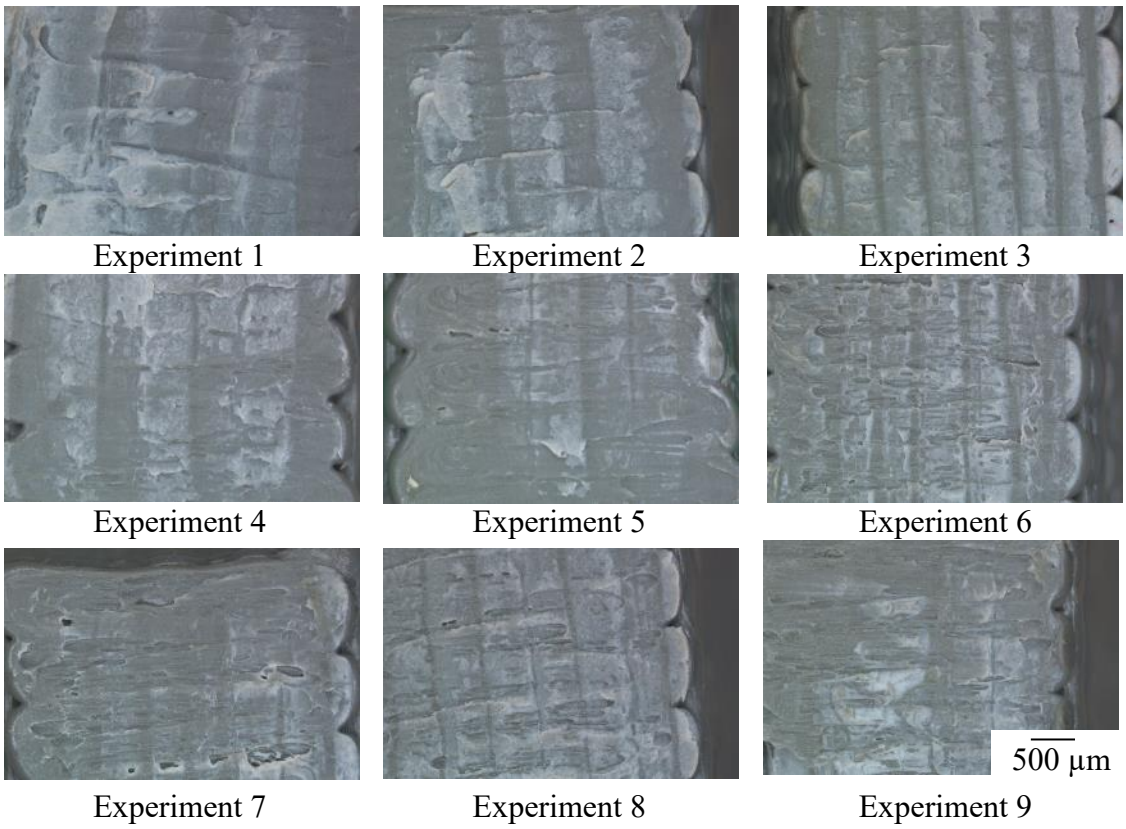

Figure C.14: Non-failure cross sections for each of the Taguchi experiments performed for NORYL grey vertical dogbones. The images are similar for all experiments and show rough interfaces due to void present between layers.

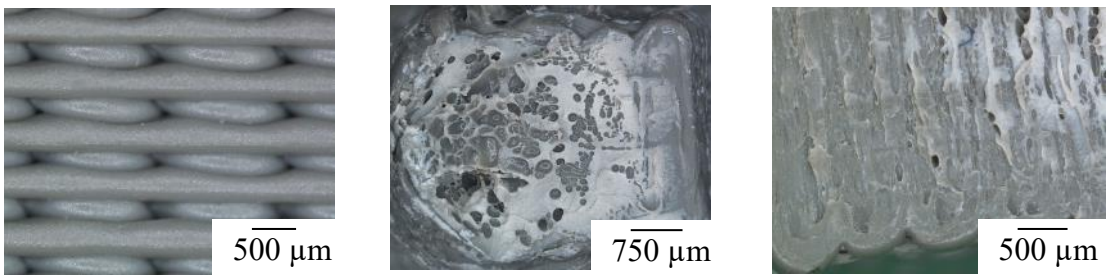

Figure C.15: Side, failure cross section, and non-failure cross section for NORYL grey vertical MEX dogbones that were not heat-treated. The images are similar to the results seen in the NORYL grey vertical MEX dogbones exposed to elevated heat-treatment temperatures in the Taguchi process optimization.

While the side images shown in Figure C.12 do not show obvious inter-laminar defects in the NORYL grey vertical dogbones, the failure cross sections and non-failure cross sections shown in Figure C.13 and Figure C.14 show the presence of large voids within roads and between layers. The failure cross sections showed that the dogbones did not fail cleanly at a layer interface and instead failed within a layer due to the large voids present in the roads. The layer interfaces shown in the non-failure cross sections showed rough interfaces that resulted from voids between the individual layers. The images shown in Figure C.15 for the room temperature samples were similar to the images of the Taguchi experiments.

The presence of voids within the roads and between layers could also have prevented the heat-treatments from significantly improving the mechanical properties of the vertical dogbones. The results of the lap-shear bonding experiments in section showed that NORYL could develop interfacial bonding at the times and temperatures used for the heat-treatments in the Taguchi studies. However, since the voids within the roads resulted

in failure within the roads instead of at the layer interface, the interlayer bonding strength was not effectively measured.

A microscope image of the NORYL grey MEX filament used to fabricate the vertical dogbones is shown in Figure C.16**.** Air gaps present in the filament cross section could have led to the presence of voids within the individual roads. In addition, underflow resulting from voids in the filament could also have resulted in the voids in between layers.

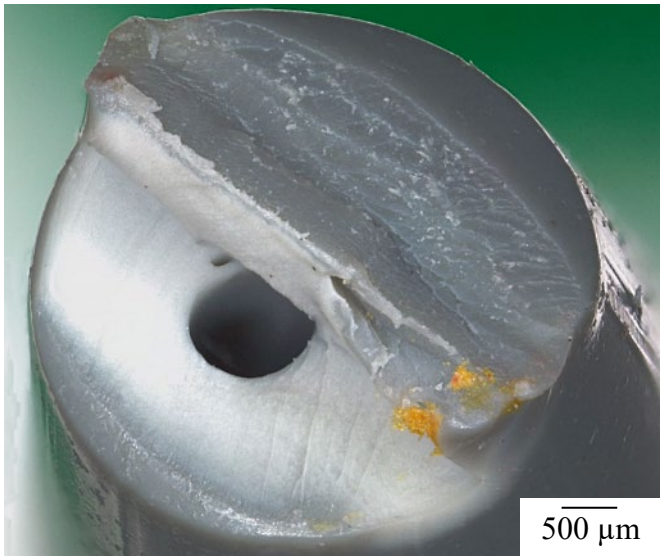

Figure C.16: A cross section of the NORYL grey MEX filament showed voids in the filament. These pockets could result in underflow in the fabricated MEX parts and could have been the cause of the large voids seen within roads and between layers in the vertical MEX dogbones.

C.4 Conclusions and suggested future work

NORYL was investigated as a new material for MEX. Print temperature ranges for fabricated NORYL MEX filaments were determined based on the hypothesis that MEX process variable settings for new materials could be determined by using the rheological behavior of ABS at MEX conditions as a benchmark. Lap-shear joints fabricated from NORYL sheets showed that NORYL interfaces could bond at temperatures below and around the glass transition temperature. These studies were used to set post-processing heat-treatment settings for optimization with the Taguchi method. NORYL black horizontal MEX dogbones were fabricated to examine the effect of layer thickness, print temperature, and post-processing heat-treatments on mechanical properties. The Taguchi method process optimization showed that decreasing the layer thickness significantly increased both UTS and Young's modulus.

An additional process optimization was performed using NORYL grey without varying the layer thickness to examine if post-processing heat-treatments could improve the interlayer bonding in MEX parts. MEX dogbones were fabricated in the vertical build orientation and the effect of print temperature and post-processing heat-treatments on interlayer bonding was examined. The only control parameter determined to be significant to interlayer bonding was print temperature. Optical microscopy showed that the vertical dogbones failed within a layer due to the presence of large voids inside the roads. These voids were likely the result of flow variations during MEX deposition using the fabricated MEX filament that contained air pockets within the filament cross section. Because failure occurred within a layer, the interlayer bonding of the vertical dogbones was not effectively

characterized and the impact of post-processing heat-treatments on the interfaces could not be determined.

In order to more effectively measure the interlayer bonding and the effect of post-processing heat-treatments on improving the mechanical properties of NORYL MEX dogbones, the voids present in the deposited MEX roads need to be reduced. In future work, the extrusion method used to fabricate the NORYL MEX filament could be improved to extrude higher quality MEX filament without air pockets. Future work could also examine the use of post-processing heat-treatments below and around glass transition using commercially available amorphous MEX materials. A possible candidate material for study is HIPS, which has been shown to crack heal below glass transition temperature in the same studies that examined NORYL [6].

C.5 References

[1] D.-T. Hseih and D. G. Peiffer, "Miscibility and immiscibility in functionalized associating polymer systems: polystyrene-poly (phenylene oxide) blends," *Polymer,* vol. 33, no. 6, pp. 1210-1217, 1992.

[2] A. M. Donald and E. J. Kramer, "Craze microstructure and molecular entanglements in polystyrene-poly(phenylene oxide) blends," *Polymer,* vol. 23, no. 3, pp. 461-465, 1982/03/01/ 1982.

[3] A. S. Hay, "Polymerization by oxidative coupling: Discovery and commercialization of PPO® and Noryl® resins," *Journal of Polymer Science Part A: Polymer Chemistry,* vol. 36, no. 4, pp. 505-517, 1998.

[4] S. Stack, O. O'Donoghue, and C. Birkinshaw, "The thermal stability and thermal degradation of blends of syndiotactic polystyrene and polyphenylene ether," Polymer Degradation and Stability, vol. 79, no. 1, pp. 29-36, 2003/01/01/ 2003

[5] SABIC. (2017, 17 July). *NORYL Resin 731*. Available: https://www.sabic-ip.com/gep/Plastics/en/ProductsAndServices/ProductLine/noryl.html

[6] Y. M. Boiko and R. E. Prud'Homme, "Strength development at the interface of amorphous polymers and their miscible blends, below the glass transition temperature," *Macromolecules,* vol. 31, no. 19, pp. 6620-6626, Sep 22 1998.

[7] K. Jud, H. H. Kausch, and J. G. Williams, "Fracture-Mechanics Studies of Crack Healing and Welding of Polymers," *Journal of Materials Science,* vol. 16, no. 1, pp. 204-210, 1981.

[8] S. Wu, H. K. Chuang, and D. H. Chang, "Diffuse Interface between Polymers - Structure and Kinetics," *Journal of Polymer Science Part B-Polymer Physics,* vol. 24, no. 1, pp. 143-159, Jan 1986.

[9] I. Gibson, D. W. Rosen, and B. Stucker, *Additive Manufacturing Technologies: 3D Printing, Rapid Prototyping, and Direct Digital Manufacturing*, Second ed. Springer, 2015.

[10] W. Gao *et al.*, "The status, challenges, and future of additive manufacturing in engineering," *Computer-Aided Design,* vol. 69, pp. 65-89, Dec 2015.

[11] S.-H. Ahn, M. Montero, D. Odell, S. Roundy, and P. K. Wright, "Anisotropic material properties of fused deposition modeling ABS," *Rapid prototyping journal,* vol. 8, no. 4, pp. 248-257, 2002.

[12] C. Ziemian, M. Sharma, and S. Ziemian, M. Gokcek, Ed. *Anisotropic mechanical properties of ABS parts fabricated by fused deposition modelling*. INTECH Open Access Publisher, 2012.

[13] X. H. Liu, M. S. Zhang, S. P. Li, L. Si, J. Q. Peng, and Y. Hu, "Mechanical property parametric appraisal of fused deposition modeling parts based on the gray Taguchi method," *International Journal of Advanced Manufacturing Technology,* vol. 89, no. 5-8, pp. 2387-2397, Mar 2017.

[14] C. C. Wang, T. W. Lin, and S. S. Hu, "Optimizing the rapid prototyping process by integrating the Taguchi method with the Gray relational analysis," *Rapid Prototyping Journal,* vol. 13, no. 5, pp. 304-315, 2007.

[15] C. Bellehumeur, L. Li, Q. Sun, and P. Gu, "Modeling of bond formation between polymer filaments in the fused deposition modeling process," *Journal of Manufacturing Processes,* vol. 6, no. 2, pp. 170-178, 2004.

[16] A. Bellini and S. Guceri, "Mechanical characterization of parts fabricated using fused deposition modeling," *Rapid Prototyping Journal,* vol. 9, no. 4, pp. 252-264, 2003.

REFERENCES

[1] I. Gibson, D. W. Rosen, and B. Stucker, *Additive Manufacturing Technologies: 3D Printing, Rapid Prototyping, and Direct Digital Manufacturing*, Second ed. Springer, 2015.

[2] T. T. Wohlers, *Wohlers Report 2010: Additive Manufacturing state of the industry annual worldwide progress report*. Wohlers Associates Fort Collins, CO, 2010.

[3] I. Campbell, D. Bourell, and I. Gibson, "Additive manufacturing: rapid prototyping comes of age," *Rapid prototyping journal,* vol. 18, no. 4, pp. 255-258, 2012.

[4] J. Scott, N. Gupta, C. Weber, S. Newsome, T. Wohlers, and T. Caffrey, "Additive manufacturing: status and opportunities," *Science and Technology Policy Institute, Washington, DC,* pp. 1-29, 2012.

[5] AmericaMakes. (6 September 2018). *About America Makes*. Available: https://www.americamakes.us/

[6] W. Gao *et al.*, "The status, challenges, and future of additive manufacturing in engineering," *Computer-Aided Design,* vol. 69, pp. 65-89, Dec 2015.

[7] B. N. Turner, R. Strong, and S. A. Gold, "A review of melt extrusion additive manufacturing processes: I. Process design and modeling," *Rapid Prototyping Journal,* Review vol. 20, no. 3, pp. 192-204, 2014.

[8] R. A. Malloy, *Plastic part design for injection molding*. Hanser Publishers New York, 1994.

[9] B. N. Turner and S. A. Gold, "A review of melt extrusion additive manufacturing processes: II. Materials, dimensional accuracy, and surface roughness," *Rapid Prototyping Journal,* Article vol. 21, no. 3, pp. 250-261, 2015.

[10] S.-H. Ahn, M. Montero, D. Odell, S. Roundy, and P. K. Wright, "Anisotropic material properties of fused deposition modeling ABS," *Rapid prototyping journal,* vol. 8, no. 4, pp. 248-257, 2002.

[11] D. L. Bourell, M. C. Leu, and D. W. Rosen, "Roadmap for additive manufacturing: identifying the future of freeform processing," *The University of Texas at Austin, Austin, TX,* pp. 11-15, 2009.

[12] C. Ziemian, M. Sharma, and S. Ziemian, M. Gokcek, Ed. *Anisotropic mechanical properties of ABS parts fabricated by fused deposition modelling*. INTECH Open Access Publisher, 2012.

[13] X. H. Liu, M. S. Zhang, S. P. Li, L. Si, J. Q. Peng, and Y. Hu, "Mechanical property parametric appraisal of fused deposition modeling parts based on the gray Taguchi method," *International Journal of Advanced Manufacturing Technology,* vol. 89, no. 5-8, pp. 2387-2397, Mar 2017.

[14] C. C. Wang, T. W. Lin, and S. S. Hu, "Optimizing the rapid prototyping process by integrating the Taguchi method with the Gray relational analysis," *Rapid Prototyping Journal,* vol. 13, no. 5, pp. 304-315, 2007.

[15] Q. Sun, G. Rizvi, C. Bellehumeur, and P. Gu, "Effect of processing conditions on the bonding quality of FDM polymer filaments," *Rapid Prototyping Journal,* vol. 14, no. 2, pp. 72-80, 2008.

[16] Q. Sun, G. Rizvi, C. Bellehumeur, and P. Gu, "Experimental study of the cooling characteristics of polymer filaments in FDM and impact on the mesostructures and properties of prototypes," in *Proceedings of the 14th Solid Freeform Fabrication Symposium*, 2003, pp. 170-178.

[17] C. Bellehumeur, L. Li, Q. Sun, and P. Gu, "Modeling of bond formation between polymer filaments in the fused deposition modeling process," *Journal of Manufacturing Processes,* vol. 6, no. 2, pp. 170-178, 2004.

[18] P. G. de Gennes, "Conformations of polymers attached to an interface," *Macromolecules,* vol. 13, no. 5, pp. 1069-1075, 1980.

[19] Y. H. Kim and R. P. Wool, "A theory of healing at a polymer-polymer interface," *Macromolecules,* vol. 16, no. 7, pp. 1115-1120, 1983.

[20] O. A. Mohamed, S. H. Masood, and J. L. Bhowmik, "Optimization of fused deposition modeling process parameters: a review of current research and future prospects," *Advances in Manufacturing,* vol. 3, no. 1, pp. 42-53, Mar 2015.

[21] E. R. Fitzharris, I. Watt, D. W. Rosen, and M. L. Shofner, "Interlayer bonding improvement of material extrusion parts with polyphenylene sulfide using the Taguchi method," *Additive Manufacturing,* vol. 24, pp. 287-297, 12/01/2018.

[22] D. Drummer, S. Cifuentes-Cuéllar, and D. Rietzel, "Suitability of PLA/TCP for fused deposition modeling," *Rapid Prototyping Journal,* vol. 18, no. 6, pp. 500-507, 2012.

[23] M. Dawoud, I. Taha, and S. J. Ebeid, "Mechanical behaviour of ABS: An experimental study using FDM and injection moulding techniques," *Journal of Manufacturing Processes,* vol. 21, pp. 39-45, Jan 2016.

[24] J. Lee and A. Huang, "Fatigue analysis of FDM materials," *Rapid Prototyping Journal,* vol. 19, no. 4, pp. 291-299, 2013.

[25] M. F. Ashby and K. Johnson, *Materials and design: the art and science of material selection in product design*. Butterworth-Heinemann, 2013.

[26] J. Torres, J. Cotelo, J. Karl, and A. P. Gordon, "Mechanical Property Optimization of FDM PLA in Shear with Multiple Objectives," *Jom,* vol. 67, no. 5, pp. 1183-1193, May 2015.

[27] 3DxTech. (27 September 2018). *General-purpose filaments*. Available: https://www.3dxtech.com/general-purpose-filaments/

[28] MatterHackers. (27 September 2018). *3D printer filament comparison guide*. Available: https://www.matterhackers.com/3d-printer-filament-compare

[29] S. Rohringer. (27 September 2018). *2018 3D printer filament guide - all you need to know*. Available: https://all3dp.com/1/3d-printer-filament-types-3d-printing-3d-filament/

[30] Stratasys. (27 September 2018). *Our materials*. Available: http://www.stratasys.com/materials/search

[31] A. Bellini and S. Guceri, "Mechanical characterization of parts fabricated using fused deposition modeling," *Rapid Prototyping Journal,* vol. 9, no. 4, pp. 252-264, 2003.

[32] 3DxTech. (27 September 2018). *Engineering-grade filaments*. Available: https://www.3dxtech.com/engineering-polymers/

[33] 3DxTech. (27 September 2018). *Ultra-performance filaments*. Available: https://www.3dxtech.com/ultra-performance-filaments/

[34] 3DxTech. (27 September 2018). *Flexible filaments*. Available: https://www.3dxtech.com/3dxflex-flexible-filament/

[35] M. Fischer and V. Schöppner, "Fatigue Behavior of FDM Parts Manufactured with Ultem 9085," *JOM,* journal article vol. 69, no. 3, pp. 563-568, March 01 2017.

[36] A. Bagsik, S. Josupeit, V. Schoeppner, and E. Klemp, "Mechanical Analysis of Lightweight Constructions Manufactured with Fused Deposition Modeling," in *Proceedings of Pps-29: The 29th International Conference of the Polymer - Conference Papers*, vol. 1593, V. Alstadt, Ed. (AIP Conference Proceedings, Melville: Amer Inst Physics, 2014, pp. 696-701.

[37] T. Osborn *et al.*, "Experimental and Theoretical Evaluation of Stiffness Properties of Fused Deposition Modeling Parts," *Proceedings of the American Society for Composites: Thirtieth Technical Conference,* Proceedings Paper pp. 2589-2598, 2015.

[38] M. Rubinstein and R. H. Colby, *Polymer physics*. Oxford university press New York, 2003.

[39] P. C. Painter and M. M. Coleman, *Essentials of polymer science and engineering*. DEStech Publications Inc, 2008.

[40] N. Watanabe, M. Shofner, N. Treat, and D. Rosen, "A model for residual stress and part warpage prediction in material extrusion with application to polypropylene," in *2016 Annual International Solid Freeform Fabrication Sympossium*, Austin, TX, 2016.

[41] J. P. Jog and V. M. Nadkarni, "Crystallization Kinetics of Polyphenylene Sulfide," *Journal of Applied Polymer Science,* vol. 30, no. 3, pp. 997-1009, 1985.

[42] A. J. Lovinger, F. J. Padden, and D. D. Davis, "Structure of Poly(P-Phenylene Sulfide)," *Polymer,* vol. 29, no. 2, pp. 229-232, Feb 1988.

[43] R. W. Lenz, H. A. Smith, and C. E. Handlovits, "Phenylene sulfide polymers. III. The synthesis of linear polyphenylene sulfide," *Journal of Polymer Science,* vol. 58, no. 166, pp. 351-367, 1962.

[44] Z. Y. Jiang, L. A. Gyurova, A. K. Schlarb, K. Friedrich, and Z. Zhang, "Study on friction and wear behavior of polyphenylene sulfide composites reinforced by short carbon fibers and sub-micro TiO2 particles," *Composites Science and Technology,* vol. 68, no. 3-4, pp. 734-742, Mar 2008.

[45] C. J. Schwartz and S. Bahadur, "Studies on the tribological behavior and transfer film-counterface bond strength for polyphenylene sulfide filled with nanoscale alumina particles," *Wear,* vol. 237, no. 2, pp. 261-273, Feb 2000.

[46] 3DxTech. (11 July 2018). *PPS Filaments*. Available: https://www.3dxtech.com/pps-filament/

[47] N. M. DeNardo, "Additive manufacturing of carbon fiber-reinforced thermoplastic composites," Purdue University, 2016.

[48] K. S. Boparai, R. Singh, F. Fabbrocino, and F. Fraternali, "Thermal characterization of recycled polymer for additive manufacturing applications," *Composites Part B-Engineering,* vol. 106, pp. 42-47, Dec 1 2016.

[49] E. R. Fitzharris, N. Watanabe, D. W. Rosen, and M. L. Shofner, "Effects of material properties on warpage in fused deposition modeling parts," *The International Journal of Advanced Manufacturing Technology,* vol. 95, no. 5, pp. 2059-2070, Mar 1 2018.

[50] M. Rubinstein and R. H. Colby, *Polymer physics*. New York: Oxford, 2003.

[51] F. De Santis, R. Pantani, V. Speranza, and G. Titomanlio, "Analysis of Shrinkage Development of a Semicrystalline Polymer during Injection Molding," *Industrial & Engineering Chemistry Research,* vol. 49, no. 5, pp. 2469-2476, Mar 3 2010.

[52] M. L. Shofner, K. Lozano, F. J. Rodriguez-Macias, and E. V. Barrera, "Nanofiber-reinforced polymers prepared by fused deposition modeling," *Journal of Applied Polymer Science,* vol. 89, no. 11, pp. 3081-3090, Sep 2003.

[53] W. H. Zhong, F. Li, Z. G. Zhang, L. L. Song, and Z. M. Li, "Short fiber reinforced composites for fused deposition modeling," *Materials Science and Engineering a-Structural Materials Properties Microstructure and Processing,* vol. 301, no. 2, pp. 125-130, Mar 31 2001.

[54] H. L. Tekinalp *et al.*, "Highly oriented carbon fiber-polymer composites via additive manufacturing," *Composites Science and Technology,* vol. 105, pp. 144-150, Dec 10 2014.

[55] F. D. Ning, W. L. Cong, J. J. Qiu, J. H. Wei, and S. R. Wang, "Additive manufacturing of carbon fiber reinforced thermoplastic composites using fused deposition modeling," *Composites Part B-Engineering,* vol. 80, pp. 369-378, Oct 2015.

[56] Z. Z. Quan *et al.*, "Additive manufacturing of multidirectional preforms for composites: opportunities and challenges," *Materials Today,* vol. 18, no. 9, pp. 503-512, Nov 2015.

[57] S. Kumar and J. P. Kruth, "Composites by rapid prototyping technology," *Materials & Design,* vol. 31, no. 2, pp. 850-856, Feb 2010.

[58] R. W. Gray, D. G. Baird, and J. H. Bohn, "Effects of processing conditions on short TLCP fiber reinforced FDM parts," *Rapid Prototyping Journal,* vol. 4, no. 1, pp. 14-25, 1998.

[59] J. Korpela, A. Kokkari, H. Korhonen, M. Malin, T. Narhi, and J. Seppala, "Biodegradable and bioactive porous scaffold structures prepared using fused deposition modeling," *Journal of Biomedical Materials Research Part B-Applied Biomaterials,* vol. 101b, no. 4, pp. 610-619, May 2013.

[60] R. W. Gray, D. G. Baird, and J. H. Bohn, "Thermoplastic composites reinforced with long fiber thermotropic liquid crystalline polymers for fused deposition modeling," *Polymer Composites,* vol. 19, no. 4, pp. 383-394, Aug 1998.

[61] O. S. Carneiro, A. F. Silva, and R. Gomes, "Fused deposition modeling with polypropylene," *Materials & Design,* vol. 83, pp. 768-776, Oct 15 2015.

[62] 3DxTech. (27 September 2018). *Specialty filaments*. Available: https://www.3dxtech.com/specialty-filaments/

[63] L. J. Love *et al.*, "The importance of carbon fiber to polymer additive manufacturing," *Journal of Materials Research,* vol. 29, no. 17, pp. 1893-1898, Sep 14 2014.

[64] AutoDesk. (2018, September 23, 2018). *Netfabb: Additive manufacturing design software*. Available: https://www.autodesk.com/products/netfabb/overview

[65] A. Bellini, S. Guceri, and M. Bertoldi, "Liquefier dynamics in fused deposition," *Journal of Manufacturing Science and Engineering-Transactions of the Asme,* vol. 126, no. 2, pp. 237-246, May 2004.

[66] M. K. Agarwala, V. R. Jamalabad, N. A. Langrana, A. Safari, P. J. Whalen, and S. C. Danforth, "Structural quality of parts processed by fused deposition," *Rapid Prototyping Journal,* vol. 2, no. 4, pp. 4-19, 1996.

[67] N. Venkataraman, S. Rangarajan, B. Harper, M. Matthewson, A. Safari, and S. Danforth, "Process-property-performance relationship for fused deposition of ceramics (FDC) feedstock materials," *MRS Online Proceedings Library Archive,* vol. 625, 2000.

[68] N. Venkataraman *et al.*, "Mechanical and rheological properties of feedstock material for fused deposition of ceramics and metals (FDC and FDMet) and their relationship to process performance," *Solid Freeform Fabrication Proceedings, University of Texas at Austin, Austin,* pp. 351-360, 1999.

[69] N. Venkataramana *et al.*, "Feedstock material property - process relationships in fused deposition of ceramics (FDC)," *Rapid Prototyping Journal,* Article vol. 6, no. 4, pp. 244-252, 2000.

[70] M. A. Yardimci, T. Hattori, S. I. Guceri, and S. Danforth, "Thermal analysis of fused deposition," in *Proceedings of solid freeform fabrication conference*, 1997, pp. 689-698: August, University of Texas, Texas.

[71] A. Bellini, "Fused deposition of ceramics: a comprehensive experimental, analytical and computational study of material behavior, fabrication process and equipment design," 2002.

[72] N. Mostafa, H. M. Syed, S. Igor, and G. Andrew, "A study of melt flow analysis of an ABS-Iron composite in fused deposition modelling process," *Tsinghua Science & Technology,* vol. 14, pp. 29-37, 2009.

[73] H. Ramanath, C. Chua, K. Leong, and K. Shah, "Melt flow behaviour of poly-ε-caprolactone in fused deposition modelling," *Journal of Materials Science: Materials in Medicine,* vol. 19, no. 7, pp. 2541-2550, 2008.

[74] T. Karis *et al.*, "Rapid prototyping materials rheology," *Journal of Imaging Science and Technology,* vol. 40, no. 2, pp. 147-155, 1996.

[75] L. B. Ji and T. R. Zhou, "Finite element simulation of temperature field in fused deposition modeling," in *Advanced Materials Research*, 2010, vol. 97, pp. 2585-2588: Trans Tech Publ.

[76] R. S. Crockett, "The liquid-to-solid transition in stereodeposition techniques," Doctor of Philosophy, Materials Science and Engineering, University of Arizona, 1997.

[77] L. Li, Q. Sun, C. Bellehumeur, and P. Gu, "Investigation of bond formation in FDM process," *Solid Freeform Fabrication Proceedings,(403),* vol. 400407, 2002.

[78] L. Li, *Analysis and fabrication of FDM prototypes with locally controlled properties*. University of Calgary, 2002.

[79] S. Costa, F. Duarte, and J. Covas, "Estimation of filament temperature and adhesion development in fused deposition techniques," *Journal of Materials Processing Technology,* vol. 245, pp. 167-179, 2017.

[80] L. Li, Q. Sun, C. Bellehumeur, and P. Gu, "Composite modeling and analysis for fabrication of FDM prototypes with locally controlled properties," *Journal of manufacturing processes,* vol. 4, no. 2, pp. 129-141, 2002.

[81] J. Thomas and J. Rodríguez, "Modeling the fracture strength between fused deposition extruded roads," in *Proceedings of the 11th Solid Freeform Fabrication Symposium*, 2000, pp. 16-23.

[82] S. Costa, F. Duarte, and J. Covas, "Towards modelling of Free Form Extrusion: analytical solution of transient heat transfer," *International Journal of Material Forming,* vol. 1, no. 1, pp. 703-706, 2008.

[83] S. Costa, F. Duarte, and J. Covas, "Thermal conditions affecting heat transfer in FDM/FFE: a contribution towards the numerical modelling of the process: This paper investigates convection, conduction and radiation phenomena in the filament deposition process," *Virtual and Physical Prototyping,* vol. 10, no. 1, pp. 35-46, 2015.

[84] J. Zhang, X. Z. Wang, W. W. Yu, and Y. H. Deng, "Numerical investigation of the influence of process conditions on the temperature variation in fused deposition modeling," *Materials & Design,* vol. 130, pp. 59-68, 2017.

[85] Y. Zhang and Y. Chou, "Three-dimensional finite element analysis simulations of the fused deposition modelling process," *Proceedings of the Institution of Mechanical Engineers, Part B: Journal of Engineering Manufacture,* vol. 220, no. 10, pp. 1663-1671, 2006.

[86] Y. Zhou, T. Nyberg, G. Xiong, and D. Liu, "Temperature analysis in the fused deposition modeling process," in *Information Science and Control Engineering (ICISCE), 2016 3rd International Conference on*, 2016, pp. 678-682: IEEE.

[87] M. Atif Yardimci and S. Güçeri, "Conceptual framework for the thermal process modelling of fused deposition," *Rapid Prototyping Journal,* vol. 2, no. 2, pp. 26-31, 1996.

[88] Dynisco. (2016, 8 May 2017). *Capillary rheometer (LCR7000 Series)* [Online]. Available: http://www.dynisco.com/capillary-rheometer--lcr-7000-series-.

[89] Quadrantplasics.com. (8 May 2017). *Techtron PPS - Quadrant* [Online]. Available: http://www.quadrantplastics.com/na-en/products/engineering-plastics/advanced-325-425-f/techtron-R-pps.html

[90] (October 14, 2017). *Critical surface tension and contact angle with water for various polymers*. Available: https://www.accudynetest.com/polytable_03.html

[91] (2016, 8 May). *HYREL System 30* [Online]. Available: http://www.hyrel3d.com/

[92] (8 May). *Repetier homepage* [Online]. Available: http://www.repetier.com/

[93] G. Hodgson. (8 May). *Slic3r Manual* [Online]. Available: http//www.manual.slic3r.org/intro/overview

[94] A. Tsou and W. Waddell, "Fillers. Encyclopedia of Polymer Science and Technology," ed: Wiley, New York, 2002.

[95] G. W. Lee, M. Park, J. Kim, J. I. Lee, and H. G. Yoon, "Enhanced thermal conductivity of polymer composites filled with hybrid filler," *Composites Part a-Applied Science and Manufacturing,* vol. 37, no. 5, pp. 727-734, 2006.

[96] M. Moniruzzaman and K. I. Winey, "Polymer nanocomposites containing carbon nanotubes," *Macromolecules,* vol. 39, no. 16, pp. 5194-5205, Aug 8 2006.

[97] Z. D. Han and A. Fina, "Thermal conductivity of carbon nanotubes and their polymer nanocomposites: A review," *Progress in Polymer Science,* vol. 36, no. 7, pp. 914-944, Jul 2011.

[98] E. Guth, "Theory of Filler Reinforcement," *Journal of Applied Physics,* vol. 16, no. 1, pp. 20-25, 1945.

[99] Y. S. Xu, D. D. L. Chung, and C. Mroz, "Thermally conducting aluminum nitride polymer-matrix composites," *Composites Part a-Applied Science and Manufacturing,* vol. 32, no. 12, pp. 1749-1757, 2001.

[100] TORAY. (2018, 14 September 2018). *TORELINA PPS Resin*. Available: https://www.toray.jp/plastics/en/torelina/technical/tec_015.html

[101] J. Rodriguez, "Maximizing the strength of fused-deposition ABS plastic parts."

[102] C. Kousiatza, N. Chatzidai, and D. Karalekas, "Temperature mapping of 3D printed polymer plates: experimental and numerical study," *Sensors,* vol. 17, no. 3, p. 456, 2017.

[103] C. Kousiatza and D. Karalekas, "In-situ monitoring of strain and temperature distributions during fused deposition modeling process," *Materials & Design,* vol. 97, pp. 400-406, 2016.

[104] J. F. Rodriguez, J. P. Thomas, and J. E. Renaud, "Characterization of the mesostructure of fused-deposition acrylonitrile-butadiene-styrene materials," *Rapid Prototyping Journal,* vol. 6, no. 3, pp. 175-186, 2000.

[105] V. Mathot *et al.*, "The Flash DSC 1, a power compensation twin-type, chip-based fast scanning calorimeter (FSC): first findings on polymers," *Thermochimica Acta,* vol. 522, no. 1-2, pp. 36-45, 2011.

[106] C. Schick, "Differential scanning calorimetry (DSC) of semicrystalline polymers," *Analytical and bioanalytical chemistry,* vol. 395, no. 6, p. 1589, 2009.

[107] L. Jin, J. Ball, T. Bremner, and H.-J. Sue, "Crystallization behavior and morphological characterization of poly (ether ether ketone)," *Polymer,* vol. 55, no. 20, pp. 5255-5265, 2014.

[108] J. E. Schawe, "Analysis of non-isothermal crystallization during cooling and reorganization during heating of isotactic polypropylene by fast scanning DSC," *Thermochimica Acta,* vol. 603, pp. 85-93, 2015.

[109] F. De Santis, S. Adamovsky, G. Titomanlio, and C. Schick, "Scanning nanocalorimetry at high cooling rate of isotactic polypropylene," *Macromolecules,* vol. 39, no. 7, pp. 2562-2567, 2006.

[110] S. Adamovsky, A. Minakov, and C. Schick, "Scanning microcalorimetry at high cooling rate," *Thermochimica Acta,* vol. 403, no. 1, pp. 55-63, 2003.

[111] A. A. Minakov, D. A. Mordvintsev, and C. Schick, "Isothermal reorganization of poly (ethylene terephthalate) revealed by fast calorimetry (1000 K s− 1; 5 ms)," *Faraday discussions,* vol. 128, pp. 261-270, 2005.

[112] S. Z. Cheng, "Materials science: Polymer crystals downsized," *Nature,* vol. 448, no. 7157, p. 1006, 2007.

[113] M. Al-Hussein and G. Strobl, "The mechanisms of recrystallization after melting in syndiotactic polypropylene and isotactic polystyrene," *The European Physical Journal E,* journal article vol. 6, no. 4, pp. 305-314, December 01 2001.

[114] P. Holdsworth and A. Turner-Jones, "The melting behaviour of heat crystallized poly (ethylene terephthalate)," *Polymer,* vol. 12, no. 3, pp. 195-208, 1971.

[115] B. Wunderlich, *Macromolecular physics*. Elsevier, 2012.

[116] E. Zhuravlev and C. Schick, "Fast scanning power compensated differential scanning nano-calorimeter: 1. The device," *Thermochimica Acta,* vol. 505, no. 1-2, pp. 1-13, 2010.

[117] A. A. Minakov and C. Schick, "Ultrafast thermal processing and nanocalorimetry at heating and cooling rates up to 1 MK⁄ s," *Review of Scientific Instruments,* vol. 78, no. 7, p. 073902, 2007.

[118] Y. Furushima, A. Toda, V. Rousseaux, C. Bailly, E. Zhuravlev, and C. Schick, "Quantitative understanding of two distinct melting kinetics of an isothermally crystallized poly (ether ether ketone)," *Polymer,* vol. 99, pp. 97-104, 2016.

[119] A. Toda, K. Taguchi, K. Nozaki, and M. Konishi, "Melting behaviors of polyethylene crystals: an application of fast-scan DSC," *Polymer,* vol. 55, no. 14, pp. 3186-3194, 2014.

[120] A. A. Minakov, D. A. Mordvintsev, and C. Schick, "Melting and reorganization of poly (ethylene terephthalate) on fast heating (1000 K/s)," *Polymer,* vol. 45, no. 11, pp. 3755-3763, 2004.

[121] A. A. Minakov, D. A. Mordvintsev, R. Tol, and C. Schick, "Melting and reorganization of the crystalline fraction and relaxation of the rigid amorphous fraction of isotactic polystyrene on fast heating (30,000 K/min)," *Thermochimica acta,* vol. 442, no. 1-2, pp. 25-30, 2006.

[122] X. Tardif *et al.*, "Experimental study of crystallization of PolyEtherEtherKetone (PEEK) over a large temperature range using a nano-calorimeter," *Polymer Testing,* vol. 36, pp. 10-19, 2014.

[123] P. Lemstra, T. Kooistra, and G. Challa, "Melting behavior of isotactic polystyrene," *Journal of Polymer Science Part A-2: Polymer Physics,* vol. 10, no. 5, pp. 823-833, 1972.

[124] D. Blundell and B. Osborn, "The morphology of poly (aryl-ether-ether-ketone)," *Polymer,* vol. 24, no. 8, pp. 953-958, 1983.

[125] C. Fougnies, P. Damman, M. Dosiere, and M. Koch, "Time-resolved SAXS, WAXS, and DSC study of melting of poly (aryl ether ether ketone)(PEEK) annealed from the amorphous state," *Macromolecules,* vol. 30, no. 5, pp. 1392-1399, 1997.

[126] A. Toda, R. Androsch, and C. Schick, "Insights into polymer crystallization and melting from fast scanning chip calorimetry," *Polymer,* vol. 91, pp. 239-263, 2016.

[127] D. Ivanov, R. Legras, and A. M. Jonas, "The crystallization of poly (aryl-ether-ether-ketone)(PEEK): reorganization processes during gradual reheating of cold-crystallized samples," *Polymer,* vol. 41, no. 10, pp. 3719-3727, 2000.

[128] T. Liu and J. Petermann, "Multiple melting behavior in isothermally cold-crystallized isotactic polystyrene," *Polymer,* vol. 42, no. 15, pp. 6453-6461, Jul 2001.

[129] D. Ivanov and A. M. Jonas, "Isothermal growth and reorganization upon heating of a single poly (aryl− ether− ether− ketone)(peek) spherulite, as imaged by atomic force microscopy," *Macromolecules,* vol. 31, no. 14, pp. 4546-4550, 1998.

[130] M. Yasuniwa, S. Tsubakihara, Y. Sugimoto, and C. Nakafuku, "Thermal analysis of the double-melting behavior of poly (L-lactic acid)," *Journal of Polymer Science Part B: Polymer Physics,* vol. 42, no. 1, pp. 25-32, 2004.

[131] R. Androsch, H. M. N. Iqbal, and C. Schick, "Non-isothermal crystal nucleation of poly (l-lactic acid)," *Polymer,* vol. 81, pp. 151-158, 2015/12/16/ 2015.

[132] R. Androsch, A. M. Rhoades, I. Stolte, and C. Schick, "Density of heterogeneous and homogeneous crystal nuclei in poly (butylene terephthalate)," *European Polymer Journal,* vol. 66, pp. 180-189, 2015.

[133] R. Androsch, C. Schick, and A. M. Rhoades, "Application of Tammann's two-stage crystal nuclei development method for analysis of the thermal stability of homogeneous crystal nuclei of poly (ethylene terephthalate)," *Macromolecules,* vol. 48, no. 22, pp. 8082-8089, 2015.

[134] A. M. Rhoades, J. L. Williams, and R. Androsch, "Crystallization kinetics of polyamide 66 at processing-relevant cooling conditions and high supercooling," *Thermochimica Acta,* vol. 603, pp. 103-109, 2015.

[135] A. Mollova, R. Androsch, D. Mileva, C. Schick, and A. Benhamida, "Effect of supercooling on crystallization of polyamide 11," *Macromolecules,* vol. 46, no. 3, pp. 828-835, 2013.

[136] N. Bosq, N. l. Guigo, E. Zhuravlev, and N. Sbirrazzuoli, "Nonisothermal crystallization of polytetrafluoroethylene in a wide range of cooling rates," *The Journal of Physical Chemistry B,* vol. 117, no. 12, pp. 3407-3415, 2013.

[137] A. Gradys, P. Sajkiewicz, E. Zhuravlev, and C. Schick, "Kinetics of isothermal and non-isothermal crystallization of poly(vinylidene fluoride) by fast scanning calorimetry," *Polymer,* vol. 82, pp. 40-48, 2016/01/15/ 2016.

[138] D. Mileva, R. Androsch, E. Zhuravlev, and C. Schick, "Morphology of mesophase and crystals of polyamide 6 prepared in a fast scanning chip calorimeter," *Polymer,* vol. 53, no. 18, pp. 3994-4001, 2012.

[139] D. G. Papageorgiou, E. Zhuravlev, G. Z. Papageorgiou, D. Bikiaris, K. Chrissafis, and C. Schick, "Kinetics of nucleation and crystallization in poly(butylene succinate) nanocomposites," *Polymer,* vol. 55, no. 26, pp. 6725-6734, 2014/12/15/ 2014.

[140] E. Zhuravlev, V. Madhavi, A. Lustiger, R. Androsch, and C. Schick, "Crystallization of polyethylene at large undercooling," *ACS Macro Letters,* vol. 5, no. 3, pp. 365-370, 2016.

[141] E. Zhuravlev, J. W. Schmelzer, B. Wunderlich, and C. Schick, "Kinetics of nucleation and crystallization in poly (ε-caprolactone)(PCL)," *Polymer,* vol. 52, no. 9, pp. 1983-1997, 2011.

[142] M. Pyda *et al.*, "Melting and crystallization of poly (butylene terephthalate) by temperature-modulated and superfast calorimetry," *Journal of Polymer Science Part B: Polymer Physics,* vol. 44, no. 9, pp. 1364-1377, 2006.

[143] J. E. Schawe, "Influence of processing conditions on polymer crystallization measured by fast scanning DSC," *Journal of Thermal Analysis and Calorimetry,* vol. 116, no. 3, pp. 1165-1173, 2014.

[144] J. E. Schawe, P. A. Vermeulen, and M. van Drongelen, "Two processes of α-phase formation in polypropylene at high supercooling," *Thermochimica acta,* vol. 616, pp. 87-91, 2015.

[145] D. Cavallo *et al.*, "Mesophase-mediated crystallization of poly (butylene-2, 6-naphthalate): an example of Ostwald's rule of stages," *ACS Macro Letters,* vol. 1, no. 8, pp. 1051-1055, 2012.

[146] I. Kolesov, D. Mileva, R. Androsch, and C. Schick, "Structure formation of polyamide 6 from the glassy state by fast scanning chip calorimetry," *Polymer,* vol. 52, no. 22, pp. 5156-5165, 2011/10/13/ 2011.

[147] I. Stolte and R. Androsch, "Kinetics of the melt – Form II phase transition in isotactic random butene-1/ethylene copolymers," *Polymer,* vol. 54, no. 26, pp. 7033-7040, 2013/12/13/ 2013.

[148] A. Gradys, P. Sajkiewicz, S. Adamovsky, A. Minakov, and C. Schick, "Crystallization of poly(vinylidene fluoride) during ultra-fast cooling," *Thermochimica Acta,* vol. 461, no. 1, pp. 153-157, 2007/09/15/ 2007.

[149] M. Salmerón Sánchez, V. B. Mathot, G. Vanden Poel, and J. L. Gómez Ribelles, "Effect of the cooling rate on the nucleation kinetics of poly (L-lactic acid) and its influence on morphology," *Macromolecules,* vol. 40, no. 22, pp. 7989-7997, 2007.

[150] F. De Santis, S. Adamovsky, G. Titomanlio, and C. Schick, "Isothermal nanocalorimetry of isotactic polypropylene," *Macromolecules,* vol. 40, no. 25, pp. 9026-9031, 2007.

[151] R. Androsch, M. L. Di Lorenzo, C. Schick, and B. Wunderlich, "Mesophases in polyethylene, polypropylene, and poly (1-butene)," *Polymer,* vol. 51, no. 21, pp. 4639-4662, 2010.

[152] S. Adamovsky and C. Schick, "Ultra-fast isothermal calorimetry using thin film sensors," *Thermochimica acta,* vol. 415, no. 1-2, pp. 1-7, 2004.

[153] C. Silvestre, S. Cimmino, D. Duraccio, and C. Schick, "Isothermal crystallization of isotactic poly (propylene) studied by superfast calorimetry," *Macromolecular rapid communications,* vol. 28, no. 7, pp. 875-881, 2007.

[154] D. Mileva and R. Androsch, "Effect of co-unit type in random propylene copolymers on the kinetics of mesophase formation and crystallization," *Colloid and Polymer Science,* vol. 290, no. 5, pp. 465-471, 2012.

[155] D. Mileva, R. Androsch, E. Zhuravlev, C. Schick, and B. Wunderlich, "Homogeneous nucleation and mesophase formation in glassy isotactic polypropylene," *Polymer,* vol. 53, no. 2, pp. 277-282, 2012.

[156] M. van Drongelen, T. Meijer-Vissers, D. Cavallo, G. Portale, G. V. Poel, and R. Androsch, "Microfocus wide-angle X-ray scattering of polymers crystallized in a fast scanning chip calorimeter," *Thermochimica acta,* vol. 563, pp. 33-37, 2013.

[157] D. Mileva, R. Androsch, D. Cavallo, and G. C. Alfonso, "Structure formation of random isotactic copolymers of propylene and 1-hexene or 1-octene at rapid cooling," *European Polymer Journal,* vol. 48, no. 6, pp. 1082-1092, 2012/06/01/ 2012.

[158] R. Androsch and C. Schick, "Crystal nucleation of polymers at high supercooling of the melt," in *Polymer Crystallization I*: Springer, 2015, pp. 257-288.

[159] A. Wurm *et al.*, "Crystallization and homogeneous nucleation kinetics of poly (ε-caprolactone)(PCL) with different molar masses," *Macromolecules,* vol. 45, no. 9, pp. 3816-3828, 2012.

[160] I. Stolte, R. Androsch, M. L. Di Lorenzo, and C. Schick, "Effect of aging the glass of isotactic polybutene-1 on form II nucleation and cold crystallization," *The Journal of Physical Chemistry B,* vol. 117, no. 48, pp. 15196-15203, 2013.

[161] R. Androsch, C. Schick, and J. W. Schmelzer, "Sequence of enthalpy relaxation, homogeneous crystal nucleation and crystal growth in glassy polyamide 6," *European Polymer Journal,* vol. 53, pp. 100-108, 2014.

[162] E. Zhuravlev, A. Wurm, P. Pötschke, R. Androsch, J. W. P. Schmelzer, and C. Schick, "Kinetics of nucleation and crystallization of poly(ε-caprolactone) – Multiwalled carbon nanotube composites," *European Polymer Journal,* vol. 52, pp. 1-11, 2014/03/01/ 2014.

[163] E. Zhuravlev, J. r. W. Schmelzer, A. S. Abyzov, V. M. Fokin, R. Androsch, and C. Schick, "Experimental test of Tammann's nuclei development approach in crystallization of macromolecules," *Crystal Growth & Design,* vol. 15, no. 2, pp. 786-798, 2015.

[164] J. Ibarretxe, G. Groeninckx, L. Bremer, and V. B. F. Mathot, "Quantitative evaluation of fractionated and homogeneous nucleation of polydisperse distributions of water-dispersed maleic anhydride-grafted-polypropylene micro- and nano-sized droplets," *Polymer,* vol. 50, no. 19, pp. 4584-4595, 2009/09/10/ 2009.

[165] D. Turnbull, "Correlation of Liquid-Solid Interfacial Energies Calculated from Supercooling of Small Droplets," *The Journal of Chemical Physics,* vol. 18, no. 5, pp. 769-769, 1950.

[166] L. Kailas, C. Vasilev, J.-N. Audinot, H.-N. Migeon, and J. K. Hobbs, "A real-time study of homogeneous nucleation, growth, and phase transformations in nanodroplets of low molecular weight isotactic polypropylene using AFM," *Macromolecules,* vol. 40, no. 20, pp. 7223-7230, 2007.

[167] J. Carvalho and K. Dalnoki-Veress, "Surface nucleation in the crystallisation of polyethylene droplets," *The European Physical Journal E,* vol. 34, no. 1, p. 6, 2011.

[168] R. Tol, A. Minakov, S. Adamovsky, V. Mathot, and C. Schick, "Metastability of polymer crystallites formed at low temperature studied by ultra fast calorimetry: polyamide 6 confined in sub-micrometer droplets vs. bulk PA6," *Polymer,* vol. 47, no. 6, pp. 2172-2178, 2006.

[169] V. Brucato, S. Piccarolo, and V. La Carrubba, "An experimental methodology to study polymer crystallization under processing conditions. The influence of high cooling rates," *Chemical Engineering Science,* vol. 57, no. 19, pp. 4129-4143, 2002/10/01/ 2002.

[170] J. E. Mark, *Polymer data handbook*, 2nd ed. Oxford ; New York: Oxford University Press, 2009.

[171] J. E. K. Schawe, *Practical aspects of the Flash DSC 1: Sample prepataion for measurements of polymers*. 2012, pp. 17-24.

[172] S. Z. Cheng, Z. Q. Wu, and B. Wunderlich, "Glass transition and melting behavior of poly (thio-1, 4-phenylene)," *Macromolecules,* vol. 20, no. 11, pp. 2802-2810, 1987.

[173] P. Huo and P. Cebe, "Temperature-dependent relaxation of the crystal-amorphous interphase in poly (ether ether ketone)," *Macromolecules,* vol. 25, no. 2, pp. 902-909, 1992.

[174] P. Huo and P. Cebe, "Effects of thermal history on the rigid amorphous phase in poly (phenylene sulfide)," *Colloid and Polymer Science,* vol. 270, no. 9, pp. 840-852, 1992.

[175] P. Huo and P. Cebe, "Dielectric relaxation of poly (phenylene sulfide) containing a fraction of rigid amorphous phase," *Journal of Polymer Science Part B: Polymer Physics,* vol. 30, no. 3, pp. 239-250, 1992.

[176] M. L. Di Lorenzo, M. Gazzano, and M. C. Righetti, "The role of the rigid amorphous fraction on cold crystallization of poly (3-hydroxybutyrate)," *Macromolecules,* vol. 45, no. 14, pp. 5684-5691, 2012.

[177] M. L. Di Lorenzo and M. C. Righetti, "The three-phase structure of isotactic poly (1-butene)," *Polymer,* vol. 49, no. 5, pp. 1323-1331, 2008.

[178] M. L. Di Lorenzo, M. C. Righetti, and B. Wunderlich, "Influence of crystal polymorphism on the three-phase structure and on the thermal properties of isotactic poly (1-butene)," *Macromolecules,* vol. 42, no. 23, pp. 9312-9320, 2009.

[179] J. Pak, M. Pyda, and B. Wunderlich, "Rigid amorphous fractions and glass transitions in poly (oxy-2, 6-dimethyl-1, 4-phenylene)," *Macromolecules,* vol. 36, no. 2, pp. 495-499, 2003.

[180] M. C. Righetti, E. Tombari, and M. L. Di Lorenzo, "Crystalline, mobile amorphous and rigid amorphous fractions in isotactic polystyrene," *European Polymer Journal,* vol. 44, no. 8, pp. 2659-2667, 2008.

[181] C. Y. Li and S. Z. D. Cheng, "Semicrystalline Polymers," in *Encyclopedia of Polymer Science and Technology*: John Wiley & Sons, Inc., 2002.

[182] A. Gradys *et al.*, "Crystallization of polypropylene at various cooling rates," *Materials Science and Engineering: A,* vol. 413-414, pp. 442-446, 2005/12/15/ 2005.

[183] G. J. Park, T. H. Lee, K. H. Lee, and K. H. Hwang, "Robust design: An overview," *AIAA Journal,* vol. 44, no. 1, pp. 181-191, Jan 2006.

[184] T. W. Simpson, J. D. Peplinski, P. N. Koch, and J. K. Allen, "Metamodels for computer-based engineering design: survey and recommendations," *Engineering with Computers,* vol. 17, no. 2, pp. 129-150, 2001.

[185] R. Anitha, S. Arunachalam, and P. Radhakrishnan, "Critical parameters influencing the quality of prototypes in fused deposition modelling," *Journal of Materials Processing Technology,* vol. 118, no. 1-3, pp. 385-388, Dec 3 2001.

[186] B. H. Lee, J. Abdullah, and Z. A. Khan, "Optimization of rapid prototyping parameters for production of flexible ABS object," *Journal of Materials Processing Technology,* vol. 169, no. 1, pp. 54-61, Oct 2005.

[187] J. A. Ghani, I. A. Choudhury, and H. H. Hassan, "Application of Taguchi method in the optimization of end milling parameters," *Journal of Materials Processing Technology,* vol. 145, no. 1, pp. 84-92, Jan 1 2004.

[188] J. Z. Zhang, J. C. Chen, and E. D. Kirby, "Surface roughness optimization in an end-milling operation using the Taguchi design method," *Journal of Materials Processing Technology,* vol. 184, no. 1-3, pp. 233-239, Apr 12 2007.

[189] D. M. Byrne, "The Taguchi approach to parameter design," *Quality Progress,* vol. 20, no. 12, pp. 19-26, 1987.

[190] G. Taguchi, *Introduction to quality engineering: designing quality into products and processes*. 1986.

[191] G. Taguchi, M. El Sayed, and C. Hsaing, "Quality engineering and quality systems," ed: McGraw-Hill, NY, 1989.

[192] C. Zang, M. I. Friswell, and J. E. Mottershead, "A review of robust optimal design and its application in dynamics," *Computers & Structures,* vol. 83, no. 4-5, pp. 315-326, Jan 2005.

[193] H. G. Beyer and B. Sendhoff, "Robust optimization - A comprehensive survey," *Computer Methods in Applied Mechanics and Engineering,* vol. 196, no. 33-34, pp. 3190-3218, 2007.

[194] J. Torres, M. Cole, A. Owji, Z. DeMastry, and A. P. Gordon, "An approach for mechanical property optimization of fused deposition modeling with polylactic acid via design of experiments," *Rapid Prototyping Journal,* vol. 22, no. 2, pp. 387-404, 2016.

[195] T. Nancharaiah, D. R. Raju, and V. R. Raju, "An experimental investigation on surface quality and dimensional accuracy of FDM components," *International Journal on Emerging Technologies,* vol. 1, no. 2, pp. 106-111, 2010.

[196] R. K. Sahu, S. Mahapatra, and A. K. Sood, "A study on dimensional accuracy of fused deposition modeling (FDM) processed parts using fuzzy logic," *Journal for Manufacturing Science & Production,* vol. 13, no. 3, pp. 183-197, 2013.

[197] A. K. Sood, R. K. Ohdar, and S. S. Mahapatra, "Improving dimensional accuracy of Fused Deposition Modelling processed part using grey Taguchi method," *Materials & Design,* vol. 30, no. 10, pp. 4243-4252, Dec 2009.

[198] D. Y. Chang and B. H. Huang, "Studies on profile error and extruding aperture for the RP parts using the fused deposition modeling process," *International Journal of Advanced Manufacturing Technology,* vol. 53, no. 9-12, pp. 1027-1037, Apr 2011.

[199] J. W. Zhang and A. H. Peng, "Process-Parameter Optimization for Fused Deposition Modeling Based on Taguchi Method," in *Advanced Materials Research*, vol. 538-541, L. C. Zhao, H. Wang, and C. F. Xiao, Eds. Stafa-Zurich: Trans Tech Publications, 2012, pp. 444-447.

[200] D. G. LeGrand, "Annealing," in *Encyclopedia of Polymer Science and Technology*: John Wiley & Sons, Inc., 2002.

[201] Y. M. Boiko and R. E. Prud'Homme, "Strength development at the interface of amorphous polymers and their miscible blends, below the glass transition temperature," *Macromolecules,* vol. 31, no. 19, pp. 6620-6626, Sep 22 1998.

[202] K. Jud, H. H. Kausch, and J. G. Williams, "Fracture-Mechanics Studies of Crack Healing and Welding of Polymers," *Journal of Materials Science,* vol. 16, no. 1, pp. 204-210, 1981.

[203] S. Wu, H. K. Chuang, and D. H. Chang, "Diffuse Interface between Polymers - Structure and Kinetics," *Journal of Polymer Science Part B-Polymer Physics,* vol. 24, no. 1, pp. 143-159, Jan 1986.

[204] H. W. Wyckoff, "X-ray and related studies of quenched, drawn, and annealed polypropylene," *Journal of Polymer Science,* vol. 62, no. 173, pp. 83-114, 1962.

[205] M. R. Kantz, H. D. Newman, and F. H. Stigale, "The skin-core morphology and structure–property relationships in injection-molded polypropylene," *Journal of Applied Polymer Science,* vol. 16, no. 5, pp. 1249-1260, 1972.

[206] J.-M. Guenet, "Neutron scattering investigations on the effect of crystallization temperature and thermal treatment on the chain trajectory in bulk-crystallized isotactic polystyrene," *Polymer,* vol. 22, no. 3, pp. 313-320, 1981/03/01/ 1981.

[207] I. G. Zewi, W. J. Rudik, R. D. Corneliussen, and E. V. Lind, "The ductile-brittle transition of low-density polyethylene," *Polymer Engineering & Science,* vol. 20, no. 9, pp. 622-629, 1980.

[208] G. C. Alfonso, E. Pedemonte, and L. Ponzetti, "Mechanism of densification and crystal perfection of poly(ethylene terephthalate)," *Polymer,* vol. 20, no. 1, pp. 104-112, 1979.

[209] G. Jarrousse, C. Creton, L. Léger, A. Magalhães, M. Bulters, and C. Plummer, "Self adhesion of semi-crystalline polymers below their melting point," in *Proceedings of the IUPAC world polymer congress, Paris*, 2004.

[210] J. L. Wang, H. M. Xie, Z. X. Weng, T. Senthil, and L. X. Wu, "A novel approach to improve mechanical properties of parts fabricated by fused deposition modeling," *Materials & Design,* vol. 105, pp. 152-159, Sep 2016.

[211] C. C. Yang, X. Y. Tian, D. C. Li, Y. Cao, F. Zhao, and C. Q. Shi, "Influence of thermal processing conditions in 3D printing on the crystallinity and mechanical properties of PEEK material," *Journal of Materials Processing Technology,* vol. 248, pp. 1-7, Oct 2017.

[212] P. J. Ross, *Taguchi techniques for quality engineering: loss function, orthogonal experiments, parameter and tolerance design*. 1996.